Chem Soc Rev

REVIEW ARTICLE

View Article Online
View Journal

Cite this: DOI: 10.1039/d3cs00244f

The effects of external electric fields on proteins

Michal Cifra, *[a] Saurabh Kumar Pandey, [a] Tomás Zakar, [a] Michaela Poplová, [a] Daniela G. Blanco Campoy, †[a] Jiří Průša, [a] Daniel Havelka, [a] Paolo Marracino, [b] Micaela Liberti, [c] Francesca Apollonio, *[c] Niall J. English, *[d] Carl Caleman [ef] and Erik G. Marklund *[g]

Proteins are highly abundant and, as a biomolecular class, have very versatile functions in living systems. Protein structures contain electrically charged residues and proteins' electrostatics are crucial for their function. Although protein activity is commonly modulated through a variety of ligands and post-translational modifications, an external electric field (EF) represents an alternative, physical approach. By exerting forces on charged and dipolar regions, EFs can reshape the energetic landscape and dynamic behavior of proteins. This approach offers a mass-free, rapidly switchable, spatially precise, non-contact, and reagent-free way to control protein conformation and function – features increasingly appealing for applications in green bioprocessing, neuromodulation, ultrafast structural biology, and in studying proteins without clearly ligandable sites. Despite the growing evidence for diverse and reversible control of proteins by EF, the mechanisms are still underexplored and applications have not yet grown to their full potential. This review focuses on molecular mechanisms and integrates the findings of the effects of external EFs on proteins from both computational simulations and experimental studies. The literature shows that the EF acts on protein charged and dipolar groups, and when the EF parameters are well tailored, the EF consequently triggers effects on protein rigid body motion, secondary structure, tertiary structure, quaternary structure and molecular conformation, ultimately leading to changes in protein interactions and function (enzymatic, ion channelling, switching, . . .). These effects are being utilized not only on proteins as food components but also for bionanotechnological applications, *e.g.* in membrane proteins for controlling their transport properties, and in structural and force-generating proteins to steer self-assembly pathways and dynamic behavior. The compiled evidence clarifies key mechanisms by which EFs influence proteins and identifies promising directions for biomedical, food-processing, and biotechnological applications.

Received 24th November 2025

DOI: 10.1039/d3cs00244f

rsc.li/chem-soc-rev

1 Introduction

Accounting for roughly half of the dry mass of most metabolically active cells,[1,2] proteins form the single largest class of macromolecules, and play a key roles in biological systems, for example, in catalysis, regulation, and spatiotemporal organisation. At a cellular level, the vast majority of structural aspects and main functions of the human body and all kingdoms of life are carried out by proteins.[3]

The function of a protein is determined by its primary sequence and the explicit conformation of the polypeptide chain.[4] Accordingly, the structure, conformational dynamics, and function of proteins and their assemblies,[5] as well as strategies to modulate them,[6,7] have been the focus of considerable research attention. Anomalies in these protein systems result in serious disruptions of cellular function and give rise to a variety of diseases.[8–10] For example, Alzheimer's and Parkinson's diseases are proteinopathies associated with protein misfolding and subsequent amyloid formation.[11] Although protein malfunction underlies many pathological conditions, properly functioning proteins act as highly efficient molecular machines – both *in vivo* (for example, flagellar motors, myosin,

[a] *Institute of Photonics and Electronics of the Czech Academy of Sciences, Prague 18200, Czechia. E-mail: cifra@ufe.cz*
[b] *Rise Technology srl, Lungomare Paolo Toscanelli, 170, 00121 Rome, Italy*
[c] *Department of Information Engineering, Electronics, and Telecommunications, Sapienza University of Rome, 00184 Rome, Italy. E-mail: francesca.apollonio@uniroma1.it*
[d] *University College Dublin, Ireland. E-mail: niall.english@ucd.ie*
[e] *Department of Physics & Astronomy, Uppsala University, Box 516, SE-75120, Uppsala, Sweden*
[f] *Center for Free-Electron Laser Science, DESY, Notkestrasse 85, DE-22607 Hamburg, Germany*
[g] *Department of Chemistry for Life Sciences, Uppsala University, Box 576, SE-75123 Uppsala, Sweden. E-mail: erik.marklund@kemi.uu.se*
† Present address: J. Heyrovský Institute of Physical Chemistry of the Czech Academy of Sciences, Prague, 18200, Czechia.

DNA and RNA polymerases) and in bionanotechnological applications: serving as nanomotors,[12] nanoscissors (lytic and cleavage enzymes),[13] nanoassembly lines (synthase enzymes),[14] and photoelectric transducers (light-harvesting protein complexes).[15]

Therefore, having the ability to control the protein structure and conformation, hence protein function, using an electric field (EF), as is possible in other molecules,[16–19] is a formidable opportunity for the development of methods in biotechnology, structural biology, physical chemistry, nanotechnology, biosensing, analytics, the food industry and medicine, which have features unattainable by and complementary to chemical control only.[7,20] External EFs offer a fundamentally mass-free, energy-only, parallel handle on proteins: the EF delivers force to every copy of the macromolecule without adding reagents, avoiding the stoichiometric constraints, toxicity, and downstream purification inherent to ligand or covalent chemistries: an advantage already exploited in pulsed EF (PEF) bioprocessing, where sub-millisecond bursts reshape proteins in aqueous media with no added solvent.[21] Voltage control also translates into electronic speed: nanosecond EFs of ~100 MV m^{-1} have driven Å-scale conformational transitions that can be imaged in real time by electric-field-stimulated X-ray crystallography, a timescale orders of magnitude faster than ligand binding or covalent chemistry.[22] Crucially, the stimulus can be delivered entirely without contact: picosecond PEFs radiated from dielectric-rod or wide-band antennas have been shown to trigger cellular responses without electrodes[23] and microwave and THz EF bursts drive conformational changes in enzymes or disassemble non-covalent protein polymers[24,25] and even modulate cellular activity.[26] Because EFs couple to charge and permanent or induced dipoles rather than to a defined binding pocket, they can bias catalytic and allosteric energy landscapes even in "undruggable" proteins. This review surveys recent studies on how external EFs (pulsed, static, and oscillating up to the low-THz range) influence protein structure, conformation, and function, both in isolated molecules and in assemblies.

Why can EFs influence and potentially control protein function? Typically, proteins are charged dielectric nano-objects with a complex multipolar charge distribution.[27–31] Consequently, the protein electrostatics (the distribution and interaction of electric charges within a protein) is a critical feature influencing its structure, stability, and function.[32–34] Strong molecular EFs are known to play an essential role in protein folding,[33] protein–ligand,[35] protein–solvent,[32,36] and protein–protein[37] interactions, molecular recognition,[38] as well as enzyme catalysis.[39–42] Some proteins' conformation is naturally regulated by EFs *in vivo*: voltage-gated ion channels switch between open and closed states depending on the voltage across the membranes in which they are incorporated.[43–45] For these reasons, it is reasonable to assume that external EFs with appropriately chosen parameters of EF strength, waveform and spatial structure could modulate protein function or be used to probe the biophysical properties of proteins.

Our major focus is on works that provide a mechanistic (protein structure and dynamics-based) understanding of the observed effects so that the electromagnetic-field-based control of protein function and geometry can be rationally developed for the benefit of biomedicine and bionanotechnology, exemplified by our recent works.[21,46,47] While there are reviews which cover some selected form of EF on proteins or application focus, they lack the comprehensive focus on mechanisms and often include complex samples (emphasizing food products or protein extraction from tissues,[48–63] or focusing on protein structures in cells[64,65]) which prevents drawing mechanistic conclusions about the EF effects on proteins.

The structure of our paper is as follows: after an introduction, we move step-wise from fundamental mechanisms of EF action on proteins (Fig. 1), covering effects on protein motion, structure, energetics, electrostatics, interactions, and function. We provide detailed comprehensive tables of experimental (Table 2) and computational works (Table 3), with necessary methodical parameters, focusing on pure or well-defined protein samples. We include sections on indirect electrophysical and electrochemical influences, and conclude by addressing outstanding challenges, and outlining future research directions.

2 Mechanisms of EF action and effects on proteins

At the length and energy scales of chemistry and biology, every force (direct or emergent from many body interactions) that holds atoms together inside a molecule (covalent, ionic) or brings separate molecules together (hydrogen bonds, electrostatic, van der Waals, ...) in solution is ultimately a manifestation of electromagnetic interactions.[66] Many non-covalent molecular interactions are a direct consequence of electrostatic and (quantum) electrodynamic interactions.[67] Therefore, the EF naturally has a supreme position in the understanding of and action on the behavior of atoms and molecules. The interaction of an EF with matter fundamentally arises from its coupling to electric charges (ionic or electronic). In proteins, the direct interaction with an external field occurs due to the presence of electric charges on specific ionizable groups (fixed charges) of the constituent amino acids. Examples include glutamate and aspartate, which carry negative charges, and lysine, arginine, and histidine, which carry positive charges. The ionization state and the actual electric charge of these groups depend on the pH of the environment. A mechanistic molecular dynamics (MD) simulation study demonstrated on model peptides[68] that the effect of the EF on a peptide (namely on root-mean-square deviation of the peptide) is proportional not to the net charge of a protein, but to the number of charged residues, directly confirming the role of charged residues presences in EF effects on proteins.

Furthermore, an EF can interact with mobile electrons, such as the delocalized π-electrons found in amino acids such as tryptophan, tyrosine, and phenylalanine. The EF $\vec{E}$ exerts a force $\vec{F} = q \cdot \vec{E}$ on electric charge q. As a result, the atomic groups with zero net charge or dipole are unaffected directly by the EF. It can be helpful to visualize the charged groups in a protein as the points where the EF exerts its influence. However, even

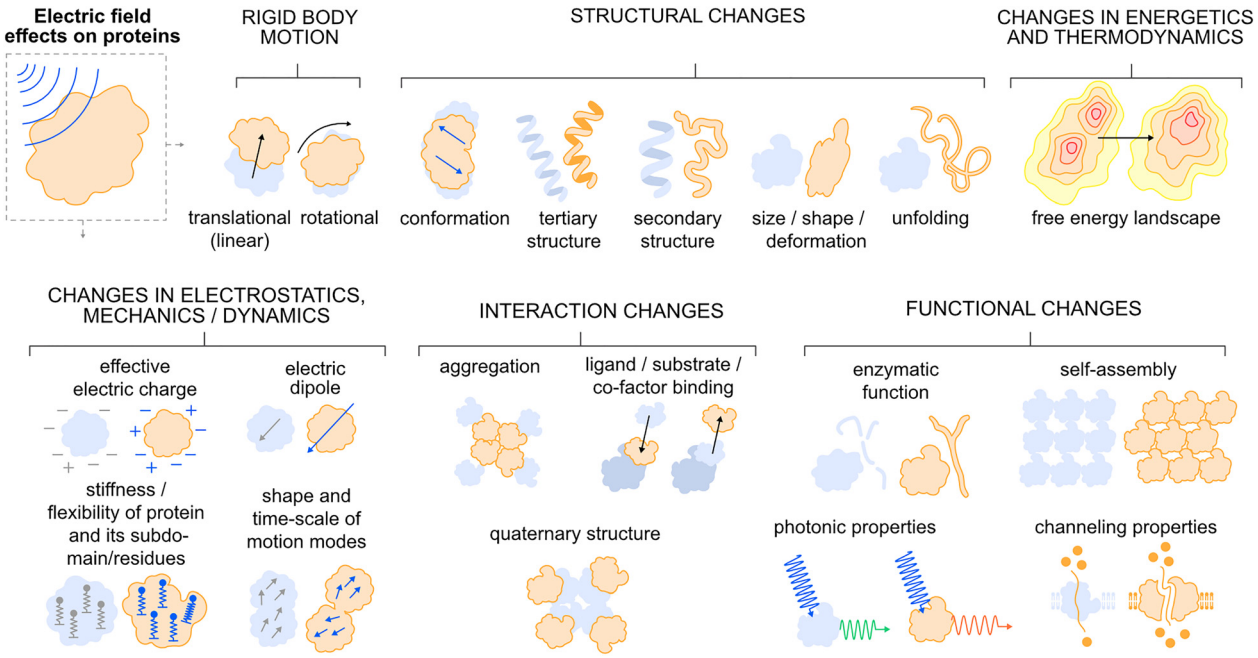

Fig. 1 An overview scheme of the physical effects of an EF on proteins as observed in molecular dynamics simulations (Table 3) and/or in experiments (Table 2). The blue shade denotes the protein status before and the orange color is the status of the protein during or shortly after EF action. The EF acts by force on the protein as an electrically charged particle by causing translational motion and *via* the protein electric dipole causing rotational motion of the protein. A sufficiently strong EF causes (in a field strength increasing manner) changes in protein structure ranging from slight conformational changes to alteration and disruptions in tertiary and even secondary structure leading to protein size and shape changes and ultimately can lead to unfolding. In another, complementary perspective the EF modulates the free energy landscape of the protein. The structural changes then lead to the modulation of the protein's electrostatic, nanomechanical, dynamic and vibrational properties across all levels of protein organization. The EF can also act (often in parallel with effects on single protein chain structure) on the interactions between proteins either causing aggregation (*via* partial unfolding), or disassembly of homotypic or heterotypic protein poly/multi/oligomers, eventually perturbing or enhancing interaction of proteins with non-peptide interaction partners. Ultimately, the EF can disrupt, modulate or even enhance the function of proteins in their enzymatic, self-assembling roles or affect photonic (such as fluorescence) or channeling properties.

non-charged groups may be affected indirectly. This occurs through interactions mediated by the surrounding solvent, nearby charged groups, or even distant charged groups within the protein structure.

The characteristics of an EF can vary based on its temporal and spatial parameters, which significantly influence its effects on proteins. Key parameters include the EF's vector (magnitude and direction), spectral (temporal) content and spatial distribution. The EF can be modulated in time in various ways, delivered as a complex waveform, or applied as a train of pulses, among other variations. For example, when the EF is delivered in pulses,[69] the number of pulses and the intervals between them (determined by an inverse parameter known as the firing frequency) are crucial factors. Each of these parameters can influence how the EF interacts with individual protein molecules or protein assemblies. Beyond temporal structuring, the electromagnetic field can also be spatially shaped.[70–72] However, creating complex EF spatial patterns, particularly at molecular scales and in three dimensions, presents significant technical challenges. Such efforts approach the physical limits of current nanotechnology[73–75] and photonics, and have therefore not been extensively explored for protein control. Here a great portion of inspiration can be absorbed from nature, as biomolecular interactions are largely enabled by the fact that the biomolecules including proteins themselves are nanoscale devices generating spatially complex EFs[34,76] with a dynamic range across 12 orders of magnitude in time[77] and Ångström-level spatial precision.

2.1 Effects on protein rigid body motions

2.1.1 Translational (linear) motion. The simplest effect of an EF on a protein structure with non-zero electric charge is the linear (translation) motion caused by electric force. This effect is exploited in a wide family of electrophoresis-based liquid or gel analytical techniques covered in a plethora of review articles and books, *e.g.*, refs. 83 and 84. On the level of larger protein assemblies, both linear and rotational motion induced by EFs (static or oscillating) were observed and exploited for the characterization and micromanipulation of single microtubules (MTs) and their networks. This has been done either by dielectrophoretic effects using an alternating EF (frequencies up to 10 MHz)[85–87] or long electric pulses (tens of seconds to minutes) using a static EF (direct current),[88–90] and often in combination with kinesin-coated surfaces that power the MTs' motion.[85,89,91,92] Similarly, but in fewer works, the EF has been used for the manipulation of actin filaments.[93–96]

These works demonstrate that an EF can act on protein polymer fibers, leading to their linear and turning motions, hence enabling molecular manipulation at the single protein

fiber level. Those results have a potential significance for bio-nanotechnological manipulation techniques and provide inspiration for what effects one could expect on the single protein level.

2.1.2 Rotational motion. Rigid-body rotational degrees of freedom (in which whole domains pivot as nearly rigid units about hinge axes) give proteins a low-energy mechanism to re-orient catalytic or binding surfaces, synchronize multi-step reaction cycles, and transmit long-range allosteric signals, thereby serving as a fundamental determinant of protein function.[97–102] Hence, EFs have the potential to influence and manipulate a variety of these rotation-dependent functions.

The tendency of a protein's dipole moment to rotate and align with an external EF is the fundamental physical mechanism underlying EF-induced protein rotation. The same principle also forms the basis of many dielectric spectroscopy techniques, where the relaxation of the real part of the permittivity of protein solutions reflects the rotational diffusion dynamics of the proteins.[103,104] The rotation of proteins by an EF has also been observed using optical methods, by analyzing the anisotropy of the optical signal, which is caused by EF-induced rotation of proteins, as illustrated in Fig. 2.[81,105–117] However, the EF turning effects on proteins are poorly experimentally investigated at the single protein level. The two major reasons are (i) the difficulty of observing or imaging a single protein orientation on short time scales and (ii) the high EF strength that might be required to overcome the rotational diffusion due to thermal motion. So far, there have only been a few computational works that have demonstrated this effect, see Table 3, which may guide future experiments along these lines. An emerging area where rotational manipulation of proteins with EFs would have a large impact is X-ray imaging of single molecules.[79] In X-ray single particle imaging (SPI), individual proteins are injected with random orientation into vacuum where they are exposed to the extremely intense (up to 10^{12} photons per pulse) femtosecond pulse delivered by the XFEL, each giving rise to a diffraction pattern reflecting its orientation at the time of exposure.[118] From the diffraction data the three-dimensional (3D) structures of the proteins can in principle be determined, alleviating the need for crystallization or other limitations that restrict conventional techniques for structural biology. Powerful algorithms[119] exist to assemble the data and enable structure determination, but they can be stumped by sparse or missing data, or noise from radiation damage,[120] electronics or sample heterogeneity.[121] One way to improve the performance of these algorithms is to control the rotation of the protein as it is exposed to the XFEL pulse. This could make SPI work with smaller sets of useful diffraction data, which would extend the application range of this technique.[122] The protein rotation can be controlled by using static EFs that couple to the intrinsic dipole moment of the protein,[79,123] or using lasers *via* a protein's anisotropic polarizability.[124] However, these techniques have so far been

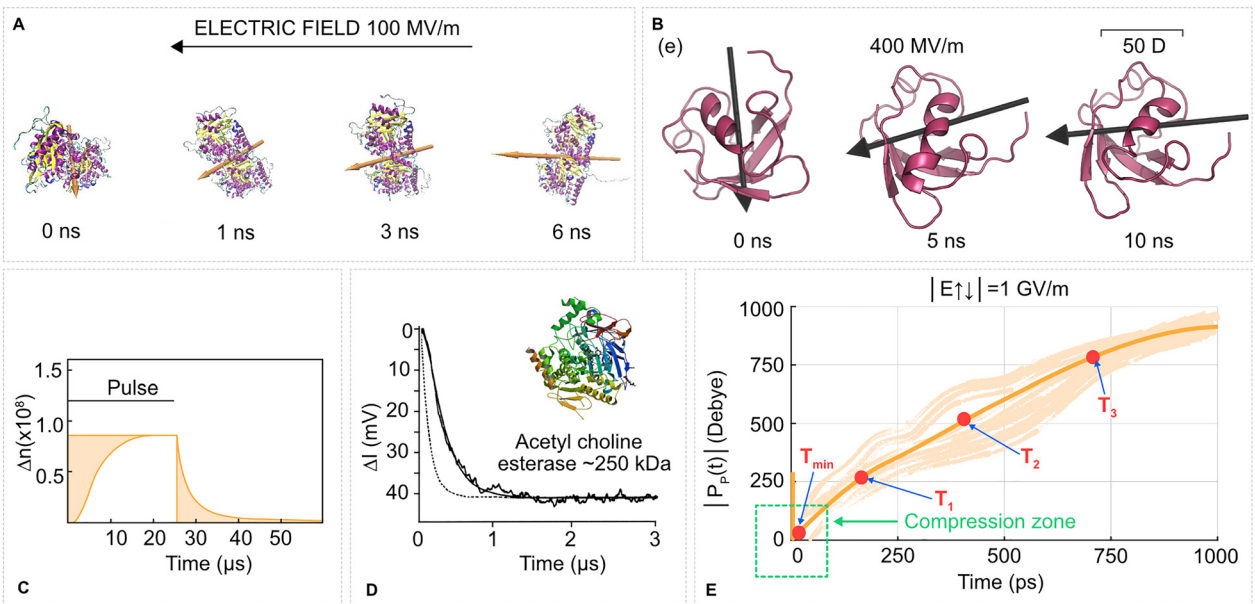

Fig. 2 Protein rotation due to the torque of an EF on a protein permanent dipole is one of the most straightforward yet underutilized effects. (A) Tubulin protein in a molecular dynamics simulation (water and ions not shown) in a 100 MV m^{-1} EF aligns its dipole moment (orange arrow) with the EF vector (black arrow on the top) within a few nanoseconds. Based on our data from ref. 78. (B) Ubiquitin in a gas phase molecular dynamics simulation rotates to align its dipole moment with the EF vector. Adapted with permission from ref. 79. © (2017) American Chemical Society. (C) A pulsed EF (0.4 MV m^{-1}, 25 μs) induces birefringence of a water solution of tubulins due to alignment of tubulin proteins with the EF. Adapted with permission from ref. 80. © (1985) Elsevier. (D) The same experimental method as in C (birefringence signal in mV), relaxation of esterase solutions after a 2.46 MV m^{-1} EF pulse. Adapted with permission from ref. 81. © (1996) Elsevier. (E) Time evolution of the dipole moment magnitude of ubiquitin from molecular dynamics simulations. The protein is initially positioned with its dipole moment vector antiparallel to the EF vector, and hence undergoes fast compression. Then the protein swiftly rotates to parallel with the increase of dipole moment magnitude. T_1, T_2, T_3 corresponds to time points when the dipole magnitude was 1×, 2×, 3× the initial magnitude, respectively. The thick line is the mean of the traces from individual MD simulations. Adapted with permission from ref. 82. © (2022) Wiley.

described only theoretically. Efforts are currently being made to integrate EF-mediated orientation with native mass spectrometry to deliver well-defined and homogeneous mass-selected and oriented protein complexes from heterogeneous mixtures for SPI at the European XFEL.[128,129] Marklund *et al.*[79] simulated a gas-phase Trp-cage, a ribosome protein domain, ubiquitin and lysozyme under the influence of strong EFs and showed that there is an "orientation window" of field strengths where proteins become oriented but with intact structures. At field strengths extending into the GV m^{-1} range the proteins started to unfold on a 10-ns timescale, whereas for longer exposure times (50 ns) the window appeared to shift towards lower fields, Fig. 2. Subsequent simulations using ramped fields that gradually increase from zero field strength, which is more realistic than an instantaneous onset, indicated that ramping is better for preserving the structure, but also that protein orientation happens before unfolding – "orientation before destruction" – meaning that a well-timed pulse could be used to image native-like structures also with destructive field strengths.[123] With the purpose of increasing the dipole of the gas phase samples, to make the orientation easier, simulation studies have explored the effect of adding a layer of water around the protein.[130] This seems to have some positive effects, at least for the protein simulated. The water increases the total dipole slightly, but more importantly it tends to make the dipole more stable and decreases the deviation between the protein structures, which is crucial for reaching high resolution SPI. Another way to increase the dipole of proteins would be to add dipole enriching segments to the molecule itself, like chromophores,[131] but then again, it's important to understand how these affect the structure.

2.2 Effects on protein structure

Beyond translational and rotational rigid body-like motions, intense EFs can significantly influence protein structure at various levels, including overall conformation, tertiary structure, and secondary structure, as well as size, shape, surface area, and unfolding behavior, see Tables 2 and 3.

2.2.1 Effects on conformation and tertiary structure. Tertiary structure is the unique three-dimensional fold adopted by a single

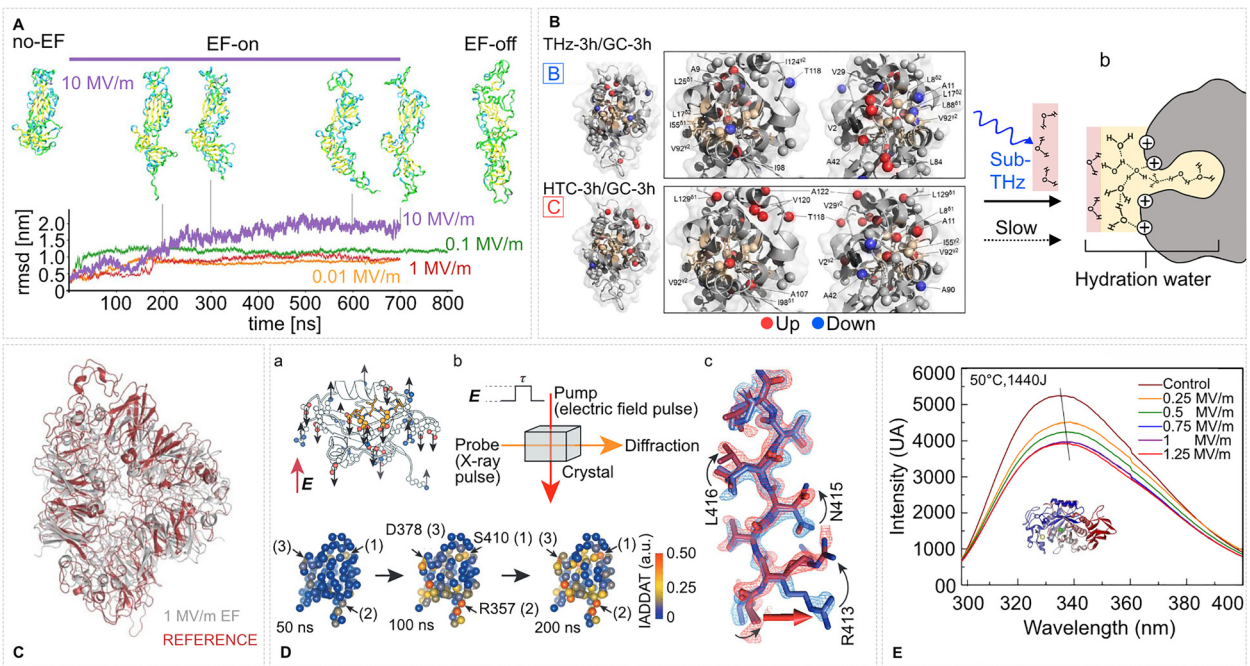

Fig. 3 Conformation and tertiary structure changes in proteins induced by intense EFs. (A) EFs induce global conformational changes in the SARS-CoV-2 spike glycoprotein. Shown are representative RMSD trajectories under various EF strengths and structural snapshots under an EF of 10 MV m^{-1} at selected time points during and after field exposure. Adapted from ref. 125. Springer Nature (2024), CC BY 4.0. (B) Tertiary structure response of lysozyme to subTHz EF perturbation. Pathway B (THz-3 h *vs.* GC-3 h): 0.1 THz irradiation strengthens signals of core methyl groups (red spheres) while peripheral sites weaken (blue), indicating core tightening. Pathway C (HTC-3 h *vs.* GC-3 h): mild heating to 31 °C causes the inverse effect—core weakening and peripheral strengthening—suggesting cavity loosening. (b) Sub-THz radiation modifies lysozyme hydration. Schematic shows altered hydration 24 h post-irradiation. Fast, H-bond-broken water transitions to structured hydration (ochre) at the heterogeneous surface, promoting hydrophobic shielding and altered surface energetics. Adapted from ref. 24. Springer Nature (2024), CC BY 4.0. (C) EF-driven conformational changes in pea protein after 25 ns of 1 MV m^{-1} MD simulated EF exposure. Adapted with permission from ref. 126. © (2023) Elsevier. (D) EF effects on the LNX2PDZ2 protein (PDB ID: 2VWR) revealed by time-resolved X-ray crystallography. (a) Sampling of charged residues (highlighted in red) illustrates potential EF-responsive sites; the ligand is shown in yellow. (b) In EF-X, protein crystals are subjected to an EF pulse of duration τ (pump), followed by X-ray probing (probe) to detect induced structural changes. (c) Example of local rearrangements in hydrogen bonding visualized in the electron density map. Lower: Time evolution of EF-induced structural responses is mapped onto the protein's tertiary structure using Cα atom positions; color intensity reflects IADDAT (integration of absolute difference density above threshold) values. Adapted with permission from ref. 22. © (2016) Springer Nature. (E) Fluorescence spectra of α-amylase after PEF exposure show field-strength-dependent red shifts, indicating tertiary structural rearrangement. Adapted with permission from ref. 127. © (2021) Elsevier.

polypeptide chain, maintained by a network of hydrogen bonds, ionic contacts, hydrophobic packing and (in some proteins) covalent disulfide bridges that lock secondary structure elements into a precise spatial arrangement.[132] A conformation is any one of the inter-convertible spatial arrangements accessible to that folded chain on its rugged energy landscape; proteins continuously fluctuate among such conformers, and populations can shift in response to ligands, mutations or external stimuli.[4] Because active-site geometry, allosteric communication and molecular recognition all depend on both the native tertiary scaffold and its dynamic conformational ensemble, even subtle structural or energetic perturbations, such as those produced by an EF, can switch enzymatic activity, redirect signalling pathways or promote misfolding and disease.[5]

MD simulations have shown extensively that intense EFs can affect protein conformation.[68,78,82,123,126,133–158] In larger proteins, even moderate external fields (10^5–10^7 V m^{-1}) influence the protein conformation. For example, fields two orders of magnitude weaker than typically required for protein damage caused the SARS-CoV-2 spike's receptor-binding β-sheet to unravel into an unstructured coil, abolishing its ability to bind ACE2 (Fig. 3).[125] Similarly, a 30 MV m^{-1} static field applied to a GPCR (5-HT$_{1A}$ receptor) drove an atypical inward shift of its transmembrane helix 6 and disrupted the normal activation by its agonist.[135] Simulations have also shown that oscillating fields can have distinct effects on the protein structure. A study of the effect on the structure of Alzheimer's amyloid-β aggregates revealed that oscillating EFs (Os-EEF) in the low-frequency MHz–GHz range induce an "explosive" dissociation of peptide plaques, accompanied by the loss of their secondary structure, into monomers that do not reform (Fig. 4). In contrast static fields (St-EEF) tend to align peptides into dipole-stabilized parallel bundles that recombine once the field is removed.[133] This superiority of oscillating fields for irreversible disaggregation was observed consistently for both short fragments and full-length Aβ, and higher frequencies (THz) were paradoxically less effective. Notably, some proteins can tolerate very strong fields – enzymatic active sites can generate internal fields on the order of 100 MV m^{-1} – suggesting that external fields in the 0.1–1 MV m^{-1} range can be harnessed without catastrophic damage.

Experimental studies strongly support these predictions.[21,22,24,127,134,163,164] Time-resolved crystallography using MV m^{-1} pulses (EF-X) has directly visualized Å-scale backbone and side-chain movements throughout a protein crystal, mirroring allosteric conformational changes.[22] Terahertz (THz) absorption and NMR experiments have shown that intense sub-THz

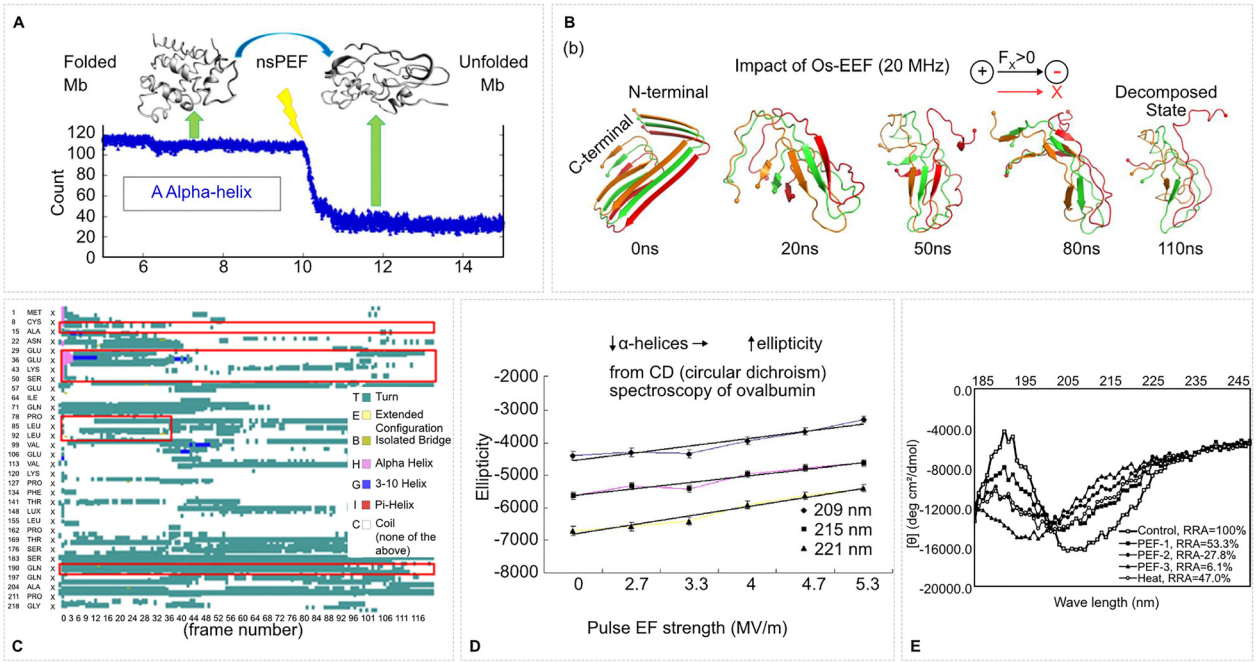

Fig. 4 EF-induced secondary structure transitions in proteins. (A) Nanosecond PEFs (nsPEFs) unfold myoglobin (Mb), as seen by the sharp drop in α-helical content. The structural transition from folded to unfolded Mb correlates with the timing of the nsPEF exposure. Adapted with permission from ref. 159. © (2013) American Chemical Society. (B) Oscillating EFs (20 MHz) progressively disrupt the secondary structure of an Aβ-42 peptide fragment, leading to decomposition over 110 ns. Snapshots show the gradual destabilization from N- to C-terminal under directional field-induced force. Adapted from ref. 133. CC BY 4 (2025) American Chemical Society. (C) Time-resolved secondary structure evolution of β-casein under a pulsed EF from MD simulations. Frame-by-frame analysis reveals EF-induced transitions from α-helix (pink) to coil (cyan) and other motifs. Adapted with permission from ref. 160. © (2023) Elsevier. (D) Circular dichroism spectra of ovalbumin show increased ellipticity and loss of α-helicity with rising PEF strength at characteristic wavelengths (209, 215, and 221 nm), indicating unfolding or loss of ordered structure. Adapted with permission from ref. 161. © (2018) Elsevier. (E) CD spectra of pepsin exposed to varying PEF treatments show field-strength-dependent loss of secondary structure, reflected in reduced relative retention of activity (RRA) and spectral shifts, compared with thermal denaturation. Adapted with permission from ref. 162. © (2004) American Chemical Society.

irradiation perturbs protein–water dynamics nonthermally: in ubiquitin, a 0.1 THz field accelerates hydrogen–deuterium exchange at buried amides while slowing exchange at surface loops, an effect opposite to uniform heating.[163] Dielectric relaxation measurements combined with NMR spectroscopy on lysozyme solutions similarly found that sub-THz fields gradually lower the solvent permittivity by reorienting hydration water into a more "hydrophobic" structuring around the protein, without bulk heating,[24] and affect protein conformation (Fig. 3).

Real-time CD and autofluorescence studies were carried out for bovine serum albumin (BSA) and lysozyme in solution for low-strength EFs. It was conjectured that for the low-intensity fields, unfolding was caused by a frictional force generated by the electrophoretic motion of the proteins. Prolonged exposure to an EF led the proteins to dissipate a large amount of frictional energy – indicating that protein unfolding is a crucial first step for protein aggregation and also possibly for the formation of amyloid fibrils.[165] Complimentarily, dynamic light scattering measurements resolved field-dependent dynamic modes of BSA and interpreted them in terms of field-induced intermolecular interactions in solution.[166]

PEFs in the 0.1 MV m^{-1} range have also been widely applied to proteins in solution, revealing diverse effects on protein conformation. Spectroscopic analyses (intrinsic fluorescence, circular dichroism (CD), Fourier transform infrared (FTIR)) show that PEF treatments often partially unfold proteins, reducing α-helix content and increasing disordered or β-sheet structures. This enhanced flexibility can increase the exposure of functional sites: for instance, 1 MV m^{-1} PEF on pea protein cut its helix fraction by 23% while doubling its binding capacity for the polyphenol EGCG (from 4 to 10 binding sites, confirmed by docking), resulting in higher antioxidant performance,[126] as illustrated in Fig. 3b. In some cases, high-intensity PEFs can even promote refolding; prawn tropomyosin treated at 2 MV m^{-1} underwent "extensive spiralization" into a tightly packed conformation, effectively masking its IgE-binding epitopes and lowering allergenicity.[134] By contrast, milder 0.5–1 MV m^{-1} pulses applied to the same protein increased its flexibility and surface exposure, initially raising antibody reactivity before eventual epitope masking at higher fields.[134]

Functional assays corroborate that conformational changes translate into altered activity. Nonthermal PEF inactivation of enzymes is one compelling example: a 0.25–1.25 MV m^{-1} pulse regime targeting α-amylase caused 70% loss of activity by specifically disrupting a tryptophan-rich active-site region, without the aggregation observed in thermal denaturation.[127] Likewise, a brief 2 MV m^{-1} PEF was found to affect conformation of α-amylase eliminating 80% of its activity when the enzyme was bound in an electrostatic complex with pectin.[167] Despite this extensive conformational damage, the PEF-treated enzyme–pectin complexes did not precipitate; instead, they assembled into larger but soluble branched structures. Classical studies used intense EFs on proteins or proteins-in-membrane fragments in solutions. They used changes in protein sample refractive index anisotropy as a real-time measure for protein conformational changes. For example, an electric pulse can induce bacteriorhodopsin to transiently release and rebind protons at distinct sites, indicating that fields perturb its proton-binding equilibrium.[168] In dried purple membrane films, alternating high-voltage fields cause complex absorbance changes that imply a multi-step cyclic conformational transition in bacteriorhodopsin.[169] Strong static fields drive a reversible spectral shift of purple bacteriorhodopsin to its deprotonated "blue" form, with only a minor retinal rotation observed.[170] In solution, microsecond field pulses reveal two distinct conformational phases in bacteriorhodopsin: an ultrafast retinal reorientation followed by a slower protein charge rearrangement.[171] Early pulsed-field experiments detected intramembrane structural changes with restricted chromophore motion in bacteriorhodopsin, and inferred an unusually high dipole polarizability as well as a five-state conformational cycle.[172] Even relatively weak fields (15 kV m^{-1}) can trigger a cooperative conformational change in bacteriorhodopsin (on a millisecond timescale).[115]

These studies demonstrate that strong EFs – whether static, pulsed, or oscillating – offer a precise means to modulate protein conformation and often also a function. Potential uses range from physically inactivating pathogens and enzymes (*e.g.* "electrodenaturation" to weaken viral spikes or halt spoilage enzymes),[125] to enhancing food proteins' digestibility and binding properties through conformational loosening,[126] to novel therapeutic approaches like disrupting amyloid aggregates with oscillating fields.[133] In parallel, the ability to trigger and probe conformational changes with fields (as in EF-X) is opening new avenues for mapping protein energy landscapes and allosteric pathways.[22]

2.2.2 Effects on secondary structure and unfolding. Proteins rely on well-defined secondary structure elements (α-helices, β-sheets, *etc.*) to maintain their three-dimensional fold and function, so even partial unfolding of these elements can lead to a drastic loss of activity or aggregation. Because complex electrostatic interactions stabilize these structural motifs, external EFs can readily perturb them: proteins' abundant polar and charged groups make their conformations highly sensitive to applied EFs.[78,173] MD simulations have been instrumental in elucidating how intense EFs induce protein secondary structure changes and unfolding. *In silico* studies show that sufficiently strong fields can overcome native stabilizing forces and disrupt secondary structure, resulting in partial or complete unfolding. For example, simulations have demonstrated field-induced unfolding of globular proteins (such as myoglobin) and even induced transitions of secondary structure (*e.g.*, converting β-sheet regions into α-helix or random coil conformations in peptides).[78] Notably, the unfolding process under a high field can follow relatively well-defined pathways, as observed in MD studies of gas-phase proteins subjected to extreme fields[47] (Fig. 5), which could open up for studies folding and unfolding pathways experimentally. Even moderate-strength fields – within experimental reach – may trigger pronounced structural changes: one simulation found that a modest EF could destabilize the SARS-CoV-2 spike glycoprotein's receptor-binding domain, converting a pair of β-strands into an unstructured loop and thereby abrogating its binding affinity.[125] Similarly, recent MD work on Alzheimer's amyloid-β (Aβ) peptides showed that an

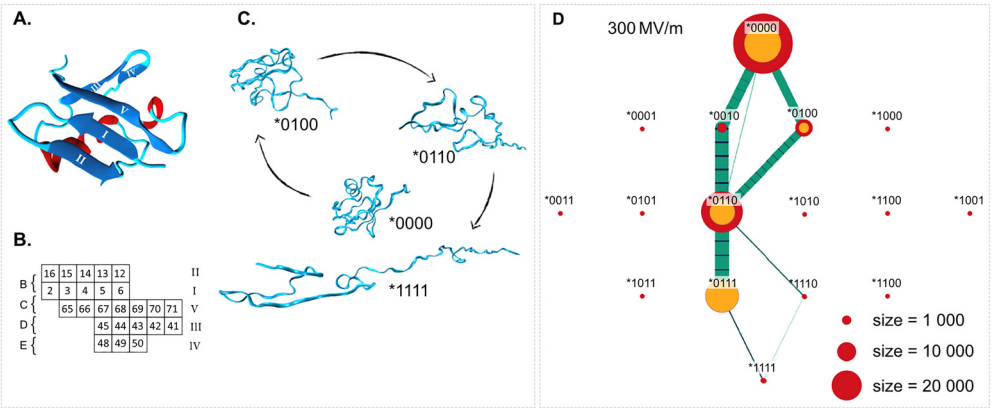

Fig. 5 One of the most common effects seen in MD simulations with EFs is protein unfolding. Here we show an example of extensive analysis from ref. 123, where unfolding pathways of ubiquitin in an EF were obtained. Adapted from ref. 47. CC BY 3 (2021) Royal Society of Chemistry. (A) The native structure of ubiquitin with the α-helix in red and the five β-strands in blue and labelled with roman numerals. (B) Physical connections (labelled B–E) between strands I–V in the native structure and the residues involved. (C) An unfolding pathway at 500 MV m^{-1}. The sate of connections are indicated as a five-bit binary number *BCDE, where 0 and 1 indicate a connection being intact and broken, respectively. D) Transition map between (un)folding states in a 300 MV m^{-1} EF, where node sizes indicate population sizes and edge widths indicate transition frequencies. Green represents transitions towards the unfolded state (downwards) and blue the opposite direction. The underlying data for this map is the aggregated data of 100 short simulations. Here, the unfolding takes place *via* a quite well-defined pathway, except that the C connection is sometimes ruptured before D and sometimes not. At higher field strengths the unfolding clearly prefers breaking the D connection first.[123]

oscillating microwave-frequency field can rapidly diminish β-sheet content in Aβ oligomers,[174] and that applying either static or oscillating oriented fields can prevent aggregation and even irreversibly dissociate preformed amyloid fibrils in long simulations.[175]

On the experimental front, a range of spectroscopic and biophysical techniques have been employed to probe EF-induced secondary structure changes and unfolding. Far-UV CD and FTIR spectroscopy provide direct readouts of secondary structure content (helix, sheet, turn), while intrinsic fluorescence (tryptophan emission) and extrinsic dye fluorescence assays (*e.g.*, ANS or thioflavin T binding) report on tertiary structure exposure and amyloid formation; complementary methods such as light scattering, electron microscopy, and X-ray scattering have also been used to characterize aggregation state and structural dimensions under EFs.[173,176,177] Using such methods, numerous studies have confirmed that EFs can induce significant secondary structure alterations and unfolding in practice. In an *in situ* CD study, Rodrigues *et al.* showed that applying a low-frequency moderate EF during heating lowers the thermal denaturation midpoint of β-lactoglobulin and alters its unfolding pathway, as evidenced by changes in CD spectra and increased hydrophobic surface exposure.[178] Peng *et al.* observed that high-frequency terahertz waves (~35 THz) act as a non-thermal denaturing agent on an Aβ amyloid, breaking apart β-sheet-rich fibrils and slowing fibrillization by ~80%, as indicated by reduced thioflavin T fluorescence and changes in the FTIR spectra.[177] PEFs, which deliver transient high-voltage bursts, have emerged as an effective tool for modifying proteins in solution. PEF treatments generally induce partial unfolding: for instance, mild PEF pretreatment (1.5 MV m^{-1} pulses) of BSA caused the protein to become more disordered and partially unfolded, exposing hydrophobic regions that greatly enhanced its binding affinity and loading capacity for the hydrophobic nutraceutical curcumin.[179] At higher PEF intensities ($\geq$2.5 MV m^{-1}) or longer exposures, however, BSA's structure was overly disrupted, leading to diminished binding—illustrating that there is an optimal degree of unfolding for functional enhancement.[179] Likewise, pulsed fields applied to soybean protein isolates initially induced unfolding of quaternary and tertiary structures, depolymerizing large protein aggregates *via* increased electrostatic repulsion, but above a threshold field strength this unfolding became extensive enough to expose reactive groups that promoted irreversible aggregation (through hydrophobic interactions and disulfide bond formation).[180] The ability to controllably perturb secondary structure with EFs carries broad implications and applications. In biotechnology and food science, electric-field-induced unfolding offers a novel means to tune protein functionality – improving solubility, emulsification, or ingredient binding by exposing buried segments, or guiding protein assembly and gelation *via* controlled denaturation.[178–180] In biomedical contexts, strong EFs or electromagnetic fields provide a noninvasive strategy to modulate proteins: for example, to weaken viral infection by structurally damaging key viral proteins,[125] or to dissolve pathogenic protein aggregates implicated in neurodegenerative diseases.[175] Ongoing research combining external fields with advanced time-resolved structural probes (*e.g.* ultrafast X-ray scattering or single-molecule imaging) promises to further illuminate the mechanisms of EF-induced protein unfolding and to harness these effects for innovative therapeutic and industrial applications.[47]

2.3 Effects on energetic and thermodynamic properties

2.3.1 Free energy landscape. External EFs reshape protein free-energy landscapes by adding a field-dependent potential, $U_{\text{field}} = -\vec{\mu}\cdot\vec{E} = -\mu E\cos\theta$, that stabilises conformers with dipoles $\vec{\mu}$ aligned to the field. Atomistic simulations consistently show

that this energetic bias can split or funnel the landscape, modifying both basin depths and barrier heights. In amyloidogenic apoC-II$_{60–70}$, a static field of 10–100 MV m^{-1} forced ∼94% dipole alignment, converting a single folded minimum into two distinct minima (compact *vs.* extended) on the R_g-end-to-end free energy landscape and lowering the extended basin by ∼5 kJ mol^{-1}.[153] Model β-sheets display a comparable field sensitivity: above ∼5 GV m^{-1} dielectric saturation attenuates water shielding, shifts the balance of hydrophobic and electrostatic terms, and changes the sheet–sheet binding free energy by tens of kJ mol^{-1}.[184] Field-induced thermodynamic shifts are not confined to backbone states. In thioredoxin, static EF as low as 20 MV m^{-1} were shown to lower the pK_a of the buried Cys35 residue by 0.5–1.0 units, corresponding to a stabilization of the thiolate form by 3–6 kJ mol^{-1} in free energy. This field-induced shift reflects enhanced electrostatic polarization of the active site, promoting deprotonation and thus favoring the catalytically competent state,[182] the PCA space was also significantly affected by a 120 MV m^{-1} EF, see Fig. 6D. Nonequilibrium MD of chignolin revealed a striking contrast between static and 2.45 GHz alternating EFs: whereas the static EF deepened the native basin, the oscillating EF flattened it and created a new metastable minimum, effectively redrawing the principal-component energy map (see Fig. 6) and accelerating state-hopping by an order of magnitude.[181] Replica-exchange MD on diphenylalanine showed an even stronger effect: a modest static EF collapsed a three-state landscape into a single dominant basin, reducing conformational entropy and producing a "funneled" surface across 310–373 K.[144] Such entropy–enthalpy trade-offs underline how EFs bias both minima and inter-state barriers. One strategy to quantify how an EF modifies protein stability is to compute field-dependent free-energy landscapes along a selected structural coordinate ξ – such as the root-mean-square deviation (RMSD), radius of gyration R_g, or a backbone principal component. Starting from a distribution $P_0(\xi)$ obtained under zero-field conditions, each protein conformation is assigned an interaction energy $U_{\text{field}}(\xi) = -\vec{\mu}(\xi)\cdot\vec{E}$, where $\vec{\mu}(\xi)$ is the dipole moment at coordinate value ξ and $\vec{E}$ is the applied field vector. This energetic bias is used to re-weight $P_0(\xi)$ using the Boltzmann factor $e^{-\beta U_{\text{field}}(\xi)}$ (with $\beta = 1/k_BT$), yielding a field-biased probability $P_E(\xi)$ and corresponding free energy $\Delta G(\xi,E) = -k_BT\ln P_E(\xi)$. This projection approach reveals how specific conformations are stabilized or destabilized by the EF. In a representative application,[185] Baumketner employed umbrella sampling to map the folding free energy of polyalanine under a static field of 0.1 GV m^{-1}, showing a ∼10 kJ mol^{-1} reduction in the folding barrier. At the same time, this bias destabilized pre-assembled β-sheets, providing a thermodynamic explanation for field-induced disaggregation of amyloid structures. Free-energy perturbation calculations likewise show that GHz–THz fields can shift the minima associated with hydration-layer dipole orientations by several kJ mol^{-1} without measurable bulk heating.[186]

In the case of free-energy profiles of water-transport proteins, MD simulations of both static and alternating EF effects

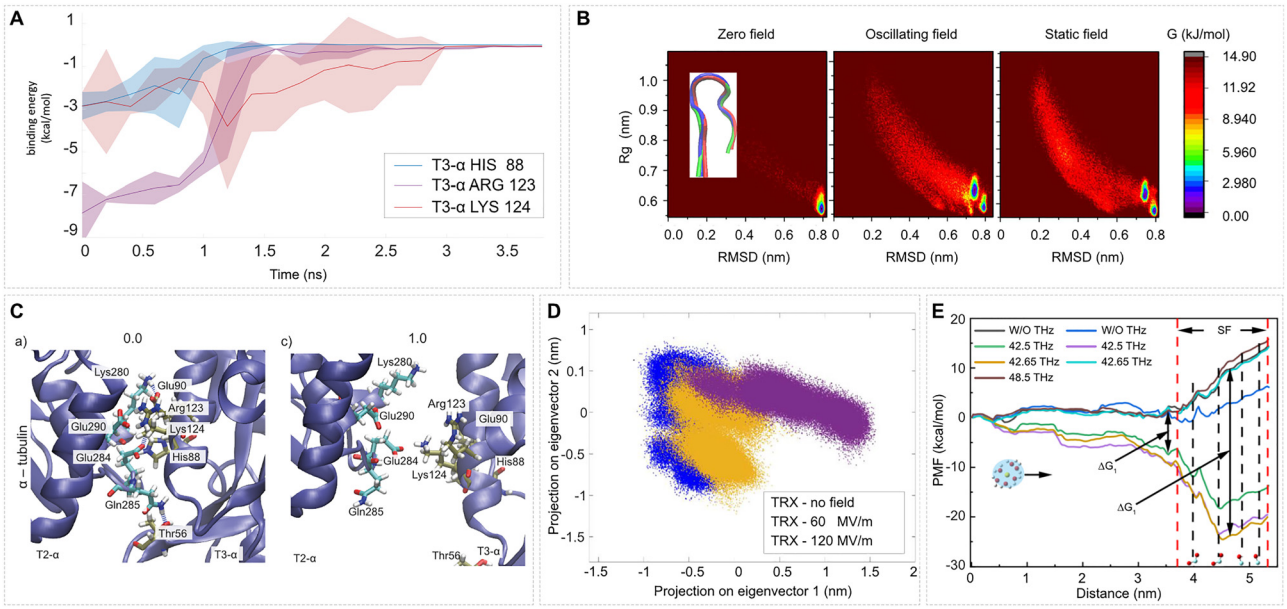

Fig. 6 EF effects on protein energetics and the free-energy landscape. (A) and (C) Snapshots of the opening detail (1st trajectory of −X 100 MV m^{-1} data): between alpha-tubulin 2 and 3 of an MT wall ring, see Fig. 11 and ref. 46. Time evolution of the binding energy contribution of six highly contributing selected amino acids. Mean values (thick line) and the standard deviation (shaded envelope) are from N = 3 trajectories. Adapted with permission from ref. 46 © (2021) Elsevier. (B) Sampled free-energy landscape of the peptide chignolin (see inset for the structure) for zero field, oscillating field, and static field. Adapted from ref. 181 under CC BY 4. (D) Principle component analysis comparison for the C-α of thioredoxin: no field (blue), E = 60 MV m^{-1} (yellow), E = 120 MV m^{-1} (violet). Adapted from ref. 182 under CC BY 4. (E) Potential of mean force (PMF) for the Cav2.1 channel with and without the presence of external THz fields (EF strength 0.6 GV m^{-1}) at different frequencies. The PMF here characterizes the capability of Ca^{2+} ions to pass through the channel. The black dashed lines represent the position of each site. Site 1 (319Gly, 668Glu, 1460Gly, 1756Ala), site 2 (318Glu, 667Glu, 1459Glu, 1755Glu), site 3 (317Met, 666Gly, 1458Gly, 1754Gly), site 4 (316Thr, 665Thr, 1457Thr,1753Thr). Adapted with permission from ref. 183. © (2025) Elsevier.

have been illuminating in the case of studying consequent dipolar orientation and the role this has on regulating water transport through human aquaporin 4.[187,188] The potentials of mean force were evaluated, as well as by using the more efficient metadynamics sampling methods, to manipulate efficiently dipole-orientation in the transport channel, and studying water–flux effects, in a case of "field-enhanced" thermodynamic-state control for water–flux regulation. Direct sampling was required for assessing the shift in the potential of mean force by alternating EFs – *ipso facto*, owing to their time-dependent nature – whilst metadynamics approaches were found in both of these studies to be effective in enhancing statistical sampling and efficiency in the case of static (time-independent) fields. Indeed, the underlying statistical-mechanics framework for direct dipole-coupling to external EFs has been accomplished in non-equilibrium metadynamics, *i.e.*, in using dipolar orientation as a direct collective variable *per se*, and this external-field control was applied to manipulate dipolar orientations of alanine.[189]

Not all field strengths produce sizeable effects: QM/MM simulations of CO binding to solvated myoglobin found that a 1 GHz field below 10 MV m^{-1} altered the binding free energy by <0.2 kJ mol^{-1}, implying a threshold above which thermal noise is overcome.[190] Nevertheless, the 42.8 THz EF has been shown computationally to lower the permeation barrier of Ca^{2+} in $Ca_V2.1$ channels,[183] and weak microwave fields subtly redistribute orientation-dependent collision free energies in carnosine solutions.[191] Collectively, these studies demonstrate that the EF, when suitably tuned, can deepen, flatten or bifurcate protein free-energy surfaces, thereby steering folding, binding, and aggregation pathways in ways that would be inaccessible through temperature or chemical perturbation alone.

2.3.2 Crystallization. Protein crystallization is indispensable for both structural biology and bioseparations, yet obtaining suitably large, well-ordered protein crystals remains notoriously challenging due to uncontrolled nucleation and growth variability.[196,197] A primary goal is often to grow a single large, defect-free crystal for X-ray or neutron diffraction, which requires suppressing spurious nucleation events so that one nucleus can consume the supersaturation.[198] Intense external EFs have emerged as a promising tool to tune protein crystallization outcomes (Fig. 7),[195,199] often involving static EFs (on the order of 0.1 MV m^{-1}) or radio-frequency alternating current (AC) fields.[192] An applied field interacts with charged and polar protein molecules, altering their spatial distribution and the chemical potential of the protein in solution and crystal phases.[195,200] This can create local supersaturation zones and modify the nucleation free-energy barrier, enabling either promotion or inhibition of nucleation depending on the field parameters.[195,201,202] For example, an EF can orient protein dipoles and induce preferred crystal orientation along the field direction,[198] and it may modify intermolecular

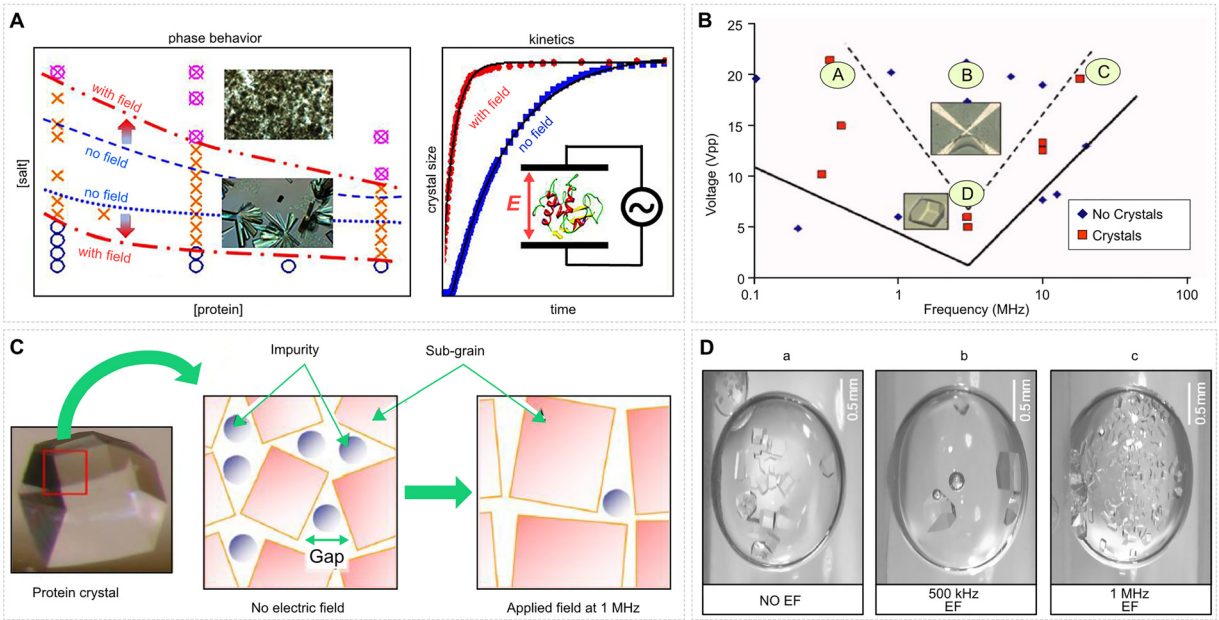

Fig. 7 Electric-field effects on lysozyme phase behaviour, nucleation, and crystal quality. (A) Left: Phase diagram of lysozyme in protein–salt concentration space with or without an EF (1 kHz, 6 kV m^{-1}). Blue circles: homogeneous protein solution; orange crosses: crystals; pink circled crosses: metastable liquid–liquid phase separation (LLPS). Red dash-dotted lines and arrows mark the field-induced downward shift of the crystallization and LLPS boundaries. Right: Growth of a single crystal, plotted as the normalized length *versus* time for field-off and field-on conditions. Adapted from ref. 192 under CC BY 4. (B) Results of 24 h nucleation assays under various AC fields. Red squares indicate conditions where crystals appeared; blue diamonds indicate no observable nuclei. Adapted with permission from ref. 193. © (2008) AIP Publishing. (C) Mechanistic model illustrating how lysozyme dimers (impurities) incorporate at step edges during growth, generating misoriented subgrains; an external field inhibits dimer incorporation, reducing misorientation and enlarging subgrain domains. Adapted with permission from ref. 194. © (2014) American Chemical Society. (D) Optical micrographs of hen-egg-white lysozyme crystals grown with $NiCl_2$ under (a) no field, (b) a 500 kHz AC field, and (c) a 1 MHz AC field. Adapted with permission from ref. 195. © (2009) American Chemical Society.

interactions enough to suppress competing liquid–liquid phase separation in favor of direct crystallization.[192] Two general modes of applying the field exist: an ''internal'' (or conducting) field with electrodes directly in the solution (allowing a DC current through the sample), and an ''external'' (or non-conducting) field where the electrodes are insulated or placed outside such that no electrolysis occurs.[201,203] Indeed, new device designs have been proposed and tested for external-electrode configurations, with some very promising results to control and manipulate field-mediated crystallization precisely, with potential applications for crystallization in, *inter alia*, the lipidic cubic phase.[204]

In typical DC-field crystallization, the protein (often carrying net charge in solution) electro-migrates toward an electrode, quickly establishing a high-concentration (supersaturated) region near that electrode.[200,205] Consequently, nucleation is preferentially localized at the electrode and is largely suppressed in the bulk or at the anode, yielding a reduced number of crystals, usually only one or a few, growing at the cathodic interface.[200,206] This method drastically reduces the overall nucleation rate while accelerating the first nucleation event (shortening induction time) and produces larger crystals than for zero-field controls.[200,206] Indeed, crystals grown under a static EF (DC) are often significantly bigger and exhibit improved diffraction quality (*e.g.*, lower ''mosaicity'' and higher resolution) due to the minimization of simultaneous nucleation events.[200,207] In contrast, an alternating-current EF (especially at high frequency) can be applied without net electro-migration, influencing crystallization through pure electrostatic effects on the free-energy landscape.[195,196] AC fields have been shown to either enhance or inhibit protein nucleation by tuning the field frequency to adjust the electrostatic contribution to the phase free energies.[195,202] Notably, under a 1 MHz AC field, lysozyme crystals grew more slowly (with reduced growth kinetics), despite an increased supersaturation driving force, as the field effectively raised the step-edge free energy and produced flatter, more orderly crystal faces; this led to substantially improved crystal quality (fewer defects and lower mosaic spread) in the tetragonal lysozyme form.[196,208] Many studies report that EFs can expedite the nucleation of proteins that are otherwise difficult to crystallize: for instance, the application of an extremely low-voltage ($\sim$1 V, 20 Hz) internal field was sufficient to induce thaumatin crystallization in a regime where no crystals normally appeared.[209] Likewise, microfluidic experiments with patterned ITO electrodes demonstrated that certain AC field configurations could both reduce nucleation induction time and localize crystal formation to specific sites, even enabling insulin crystals to form in cases where control samples showed none.[197,210]

The presence of an EF offers remarkable control over crystallization kinetics: it can reduce induction times, control the number and location of nuclei, increase crystal size, and enhance crystal quality (yielding larger and more orderly-packed crystals) under a broad range of conditions.[193,199,211] This approach has been successfully leveraged to improve protein crystal homogeneity and diffraction properties for structural analysis,[207,211] to manipulate crystal polymorphs by stabilizing a desired solid phase through field-induced shifts of the nucleation barrier,[202] and even to achieve oriented crystallization for better crystal mounting or data collection.[198,199] Continued advances in electric-field-assisted crystallization techniques – including scaling up to continuous crystallizers and combining fields with other stimuli – highlight the significant implications of this approach for both fundamental protein crystallography and practical protein manufacturing.[199,212]

2.4 Effects on electrostatic, mechanical and dynamic properties

2.4.1 Effective electric charge and dipole: local electrostatic environment. In a protein, charged residues are arranged in a defined 3D pattern. Their algebraic sum determines the protein's overall net charge, while their spatial distribution creates the molecule's permanent dipole moment. The effects of EFs on the protein dipole moment have been extensively studied using MD simulations (Fig. 8).[46,213–215] How the EFs affect protein behavior was shown by Marracino *et al.*, who investigated the polarization of the myoglobin protein in response to a pulsed/static EF of 0.1 GV m^{-1} to 1 GV m^{-1} strength.[159] It was observed that a nsPEF of 1 GV m^{-1} strength induced a fast transition (within few hundreds picoseconds) of the protein dipole moment and the protein remained highly polarized even after switching off the pulse during the simulation. The effects observed in this case of a nsPEF were very similar to those obtained after exposure to a static EF. Another interesting effect was the increase of the dipole moment after exposure to an EF of lower strength (100 MV m^{-1}). At this strength, the EF did not have any major effect on the secondary structure or overall geometry of the protein despite causing significant polarization. This slow kinetics/magnitude of polarization (upon exposure to a lower strength EF) indicated subtle changes in the structure, which might be a very helpful finding for bionanotechnology applications, in which protein structure could be manipulated without causing any denaturation effects.

Tubulin proteins, carrying an unusually high charge and dipole moment,[78] are the building unit of MTs, which makes them a target for the investigation of EF effects. Apart from the effects of the EF on the mechanical properties of the tubulin protein mentioned above,[218,219] Marracino *et al.* studied the temporal evolution of the dipole moment of a tubulin dimer as well as of individual residues that form the binding sites for various drug molecules and cofactors such as GTP/GDP.[78] Applying an EF of strength 10 MV m^{-1} to 300 MV m^{-1} resulted in the polarization of the dimer, which led to a change in the shape and orientation of the tubulin dimer. Data showed that the dipole component along the median axis (containing a highly charged C-terminal tail) is affected most, causing the C-terminal tail to extend beyond the dimer surface. The EF also affected the dipole moment of residues in the binding sites and this polarization effect varied with the strength of the applied EF. The analysis of the dipole moment in this study could be helpful in other cases such as protein–drug interactions, in which the binding of a drug can be controlled by applying an EF, or in ion channels, in which the conductance can be

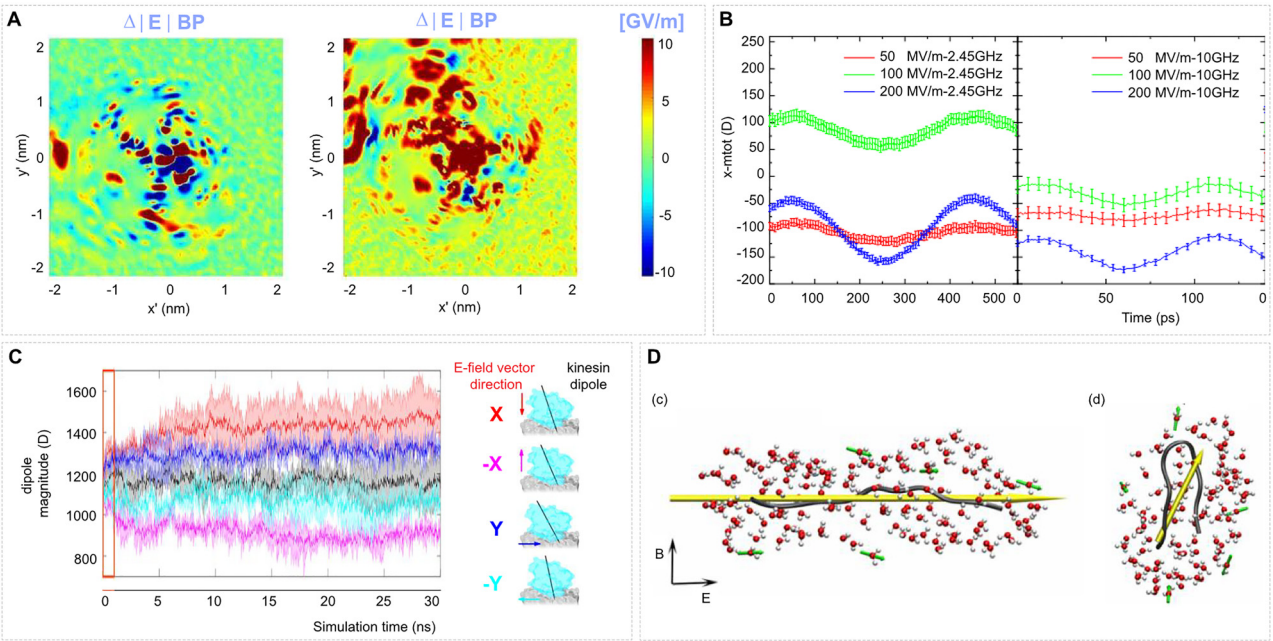

Fig. 8 EF effects on local electrostatic properties of proteins and on the protein dipole moment. (A) 2D maps of the local electrostatic field distribution around the active site of SOD1. The maps show EF shifts on the representative planes π′ (top row) and π″ (bottom row) due to a monopolar nsPEF pulse (left) and bipolar one (right). Both signals alter the electrostatic map around the central copper ion, with the monopolar pulse producing localized changes and the bipolar pulse resulting in a more diffuse and uniform distribution, suggesting the possible rotation of specific protein residues and charge redistribution under the applied field. Adapted from ref. 216 under CC BY 4. (B) Average *x*-component of the dipole moment of hen egg-white lysozyme (HEWL) under different EF conditions, computed across multiple simulation replicates. Adapted from ref. 181 under CC BY 4. (C) Time evolution of the dipole moment magnitude of kinesin under five different EF conditions: no field (black), +100 MV m^{-1} along the *X* axis (red), −100 MV m^{-1} along the *X* axis (magenta), +100 MV m^{-1} along the *Y* axis (blue), and −100 MV m^{-1} along the *Y* axis (cyan). The EF is applied continuously for the entire duration of the molecular dynamics simulations. Solid lines represent the mean dipole magnitude, and the shaded regions indicate the standard deviation computed from *N* = 3 independent replicates. Insets show kinesin bound to a tubulin protofilament at the end of the simulation; black arrows denote the kinesin dipole vector, and colored arrows indicate the direction of the applied EF, using the same color scheme as the main plot. Adapted from ref. 217 under CC BY. (D) Representative structures of the chignolin peptide and surrounding hydration layers under applied EFs of (c) 0.7 GV m^{-1} and (d) 0.7 MV m^{-1}. Dipole moment vectors of the peptide and water molecules are shown as yellow and green arrows, respectively. The directions of the applied electric *E* and magnetic *B* fields are indicated with arrows. Adapted with permission from ref. 153. © (2016) AIP Publishing.

manipulated by the effect of an external EF on the orientation of charged residues in loops.

Marracino *et al.*[220] used MD simulations to test whether classical Onsager–Kirkwood theory – valid under "weak field" linear-response conditions – still holds for nanosecond, high-intensity continuous-wave (CW) EFs. Unlike the static or ideal rectangular fields common in MD studies, real nsPEF waveforms possess finite rise/fall times that broaden their spectra into the 100 MHz–100 GHz range. The authors showed that CW amplitudes above ∼150 MV m^{-1} drive pronounced nonlinear behaviour throughout this band: higher-order polarization harmonics emerge, especially at the lower frequencies, but fade beyond the dipolar relaxation limit. The simulated polarization follows a Langevin-type curve; by adapting the Langevin function and introducing a frequency-dependent correlation $P(\omega)$, they built a predictive dipolar-interaction model ($R^2 \approx 1$) that naturally reproduces the Debye-like water relaxation time. Their results highlight the need to keep field strengths below ∼200 MV m^{-1} in protein MD studies to remain within the weak-field regime and avoid nonlinear or saturation artefacts.[221]

Protein electrostatics plays a fundamental role in shaping the structure, maintaining the stability, and governing the function of proteins through the spatial arrangement and interaction of internal charge distributions. As outlined in the Introduction, protein electrostatics is essential for processes such as molecular recognition and catalytic activity.[40,41] Intense EFs interact with proteins and lead to altered charge distributions, often mediated by water polarization. MD simulations reveal that EFs in the range of 0.1–1 GV m^{-1} can modify electrostatic environments without structural damage at lower intensities, while higher intensities may induce unfolding. For example, in superoxide dismutase (SOD1),[216] fields of 100 MV m^{-1} affect the electrostatic environment of the active site, enhancing substrate interaction. Similarly, in tubulin, fields above 20 MV m^{-1} induce significant changes of dipole components of several functionally important residues.[78] Stark spectroscopy, particularly the vibrational Stark effect,[222] is a key technique for studying protein electrostatics by measuring how local EFs influence vibrational probe frequencies, such as nitrile stretches. This spectroscopy offers insights into electrostatic forces within proteins, revealing their magnitude and direction, and was demonstrated to sense changes in internal protein electrostatics when applying a 100 MV m^{-1} EF (myoglobin in glycerol/water glass at 74 K).[223,224]

2.4.2 Nanomechanics of proteins. Mechanical properties, including stiffness, elasticity, and force resistance, are fundamental determinants of protein function, because the mechanical energy stored and released by folded domains powers conformational transitions that enable catalysis, ligand gating, mechanotransduction, and allosteric regulation.[229,230] Therefore, understanding how EFs influence protein function requires examining their impact on protein mechanics – a topic that has been explored through MD simulations under applied fields.

MTs form the cellular skeleton and guide mitosis, motility, and organelle transport (Section 18, ref. 132). Since the subunits of MT, αβ-tubulin dimers, are strongly charged, they can couple to an external EF. Saedi *et al.*[218] pulled the tubulin dimer *via* a virtual spring while subject to an EF in a MD simulation: a static 30 MV m^{-1} field softened the dimer, whereas a 1 GHz field of the same amplitude stiffened it; at 10 GHz the response was negligible because the field direction flipped too rapidly for effective coupling. Using the same protocol, Setayandeh & Lohrasebi[219] showed that 30 MV m^{-1} fields at 5 GHz increased rigidity of dimer pairs along the MT axis, whereas 1 and 6 GHz fields enhanced flexibility, mimicking taxol-stabilising effect. These studies demonstrate that EFs have the potential to modulate protein nanomechanics to achieve diverse functional outcomes, and can also be harnessed as a force handle in electromechanical force spectroscopy.

2.5 Effects on protein interactions

Protein interactions, encompassing both protein–protein interactions (PPIs) and protein–ligand (throughout our text, ''ligand'' refers to a non-protein molecule) interactions (PLIs), are fundamental to biological function and the assembly of quaternary structures. Such interactions drive the self-assembly of protein complexes, protein oligomers and polymers, and regulate processes ranging from enzymatic catalysis to signal transduction. The intermolecular forces stabilizing these complexes (hydrogen bonding, hydrophobic contacts, electrostatic interactions, *etc.*) can be sensitive to external perturbations like EFs, influencing their conformation and interaction propensity. From a thermodynamic standpoint, protein–protein interfaces are especially appealing targets for EF perturbation, because dissociating them entails overcoming a lower energy barrier than that required to trigger structural changes in individual proteins, such as unfolding.[231]

2.5.1 Protein–protein interactions: quaternary structure, multimeric complexes, fibrils and polymers. State-of-the-art molecular-dynamics simulations spanning sub-nanosecond to microsecond scales reveal how EFs from 0.01 to 1 GV m^{-1} tilt the free-energy landscape of PPIs. Radio-frequency EFs of 30 MV m^{-1} weakened the kinesin–tubulin interface by ~20%[232] which could lead to disrupted stepping kinetics; a paclitaxel-stabilised lattice showed even lower kinesin affinity under identical conditions.[233] Beyond cytoskeletal proteins, static EFs of 0.1–1 GV m^{-1} aligned peptide dipoles, favouring α-helical states and dissolving pre-assembled β-sheets.[185] For Aβ oligomers, dimers and trimers unravelled whereas pentamers kept an intact hydrophobic core, implying a size-dependent stability threshold.[214,234] ApoC-$II_{60–70}$ displayed a triphasic response: rather weak EFs (<7 MV m^{-1}) promoted β-hairpins that seed fibrils, intermediate fields (40–70 MV m^{-1}) disrupted this motif, and stronger fields elongated the peptide along the field vector, preventing aggregation.[153] Prusa *et al.*[46] studied EF effects on a 13-protofilament ring of tubulin heterodimers (periodically repeated to represent a MT wall) fully solvated with ions, and exposed to a static EF of 50 or 100 MV m^{-1}. EF orientation, magnitude and temperature, but not the ionic strength, influenced MT integrity: both field strengths repeatedly open the lattice at the protofilament lateral interface, always on the cathodic side, see Fig. 9. The study suggested that such openings may modulate MT stability and the rates of polymerisation and depolymerisation. Across these studies, electro-torque on permanent dipoles, dielectric polarisation, and field-driven water ordering emerged as common microscopic drivers.

Electrowetting-on-dielectric (EWOD) stacks platforms confine the applied voltage to the solid PDMS/Teflon dielectric and the nanometre-thin electrical double layer, leaving the interior of the micro- to nanolitre droplet virtually field-free. The resulting Maxwell stress at the three-phase line drives controllable droplet deformations that can be tracked *in situ*. Sen *et al.* used this oscillatory actuation to fragment pre-formed human serum albumin (HSA) fibrils in a sharply frequency-dependent manner, cutting ThT fluorescence by 60% at the 20 Hz optimum frequency.[235] An analogous EWOD geometry biased with a static 8 MV m^{-1} EF[227] produced a comparable loss of fibril-sheet content, confirmed by CD, AFM and TEM (Fig. 10E). Because the EF scarcely penetrates the liquid in EWOD platforms, both studies most likely induce bulk hydrodynamic shear (see Section 3 on indirect EF effects) and interfacial electrocompression rather than a direct bulk-field effect on the proteins.

Intense picosecond THz pulses provide a complementary route. Using 0.15–3 THz bursts with peak fields 40 MV m^{-1}, Hough *et al.* showed that polymerised MTs disassembled within minutes (Fig. 11C); the rate scaled with both field amplitude and spectral content, and band-pass filtering revealed maximum efficacy near 0.5 THz.[25] At the level of tubulin dimers, Chafai *et al.* exposed purified protein to a train of 2 MV m^{-1}, 10 ns EF pulses and found a dose-dependent shift from normal nucleation–elongation kinetics to suppressed assembly, tracked by turbidimetry, intrinsic fluorescence and zeta-potential changes; below 200 pulses the effect was largely reversible, whereas ≥400 pulses produced persistent inhibition,[21] with 800 pulses leading to a changed self-assembled tubulin structure as probed by AFM, see Fig. 11B. Analogous disassembly-promoting behaviour of an intense EF is observed with pathogenic protein aggregates. Jurgelevičiūté *et al.* treated isolated Sup35NM prion fibrils with PEF (10 pulses, either 50 or 1000 μs).[238] The AFM imaging revealed progressive shortening and, at 2 MV m^{-1}, complete breakup into oligomers, see Fig. 11A. Actin responded oppositely to continuous-wave 0.46 THz irradiation (power density ~0.6 W cm^{-2}), which accelerated the elongation phase of *in vitro* actin polymerisation, generating 3.5-fold more filaments without detectable denaturation, as verified by SiR-actin microscopy and pyrene fluorescence.[236]

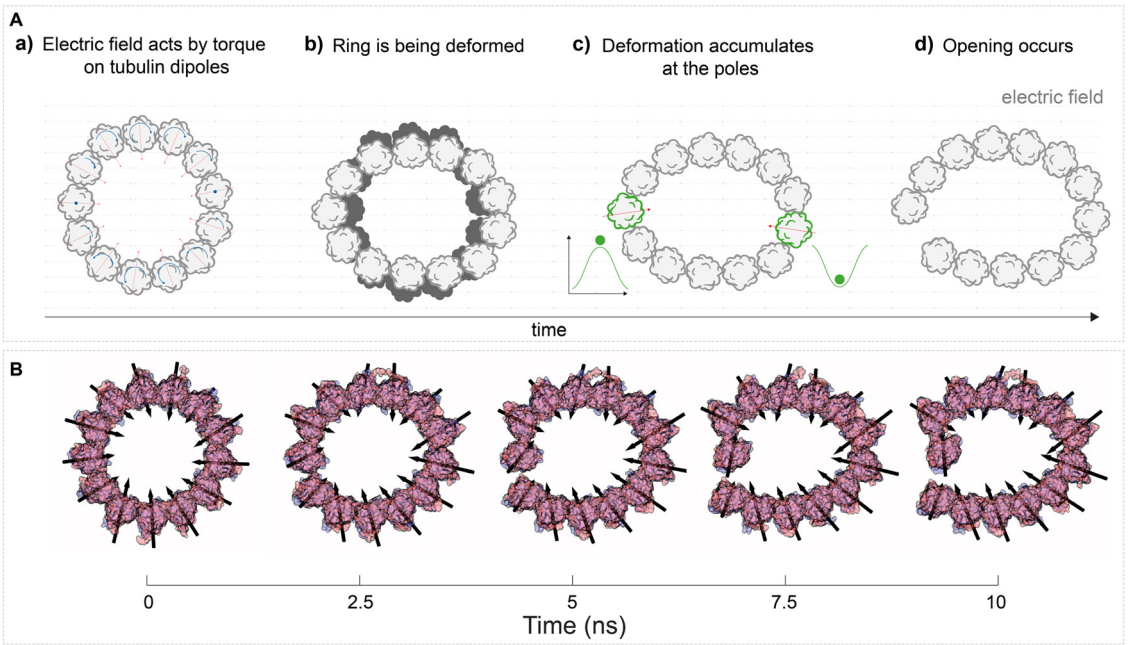

Fig. 9 EFs can affect highly ordered protein structures, such as cytoskeleton protein polymers like MTs. (A) A schematic mechanism of EF action on a MT, where the opening of the MT wall occurs due to the action on dipoles of individual tubulin subunits (B) snapshots from a representative MD simulation. Adapted with permission from ref. 46. © (2021) Elsevier.

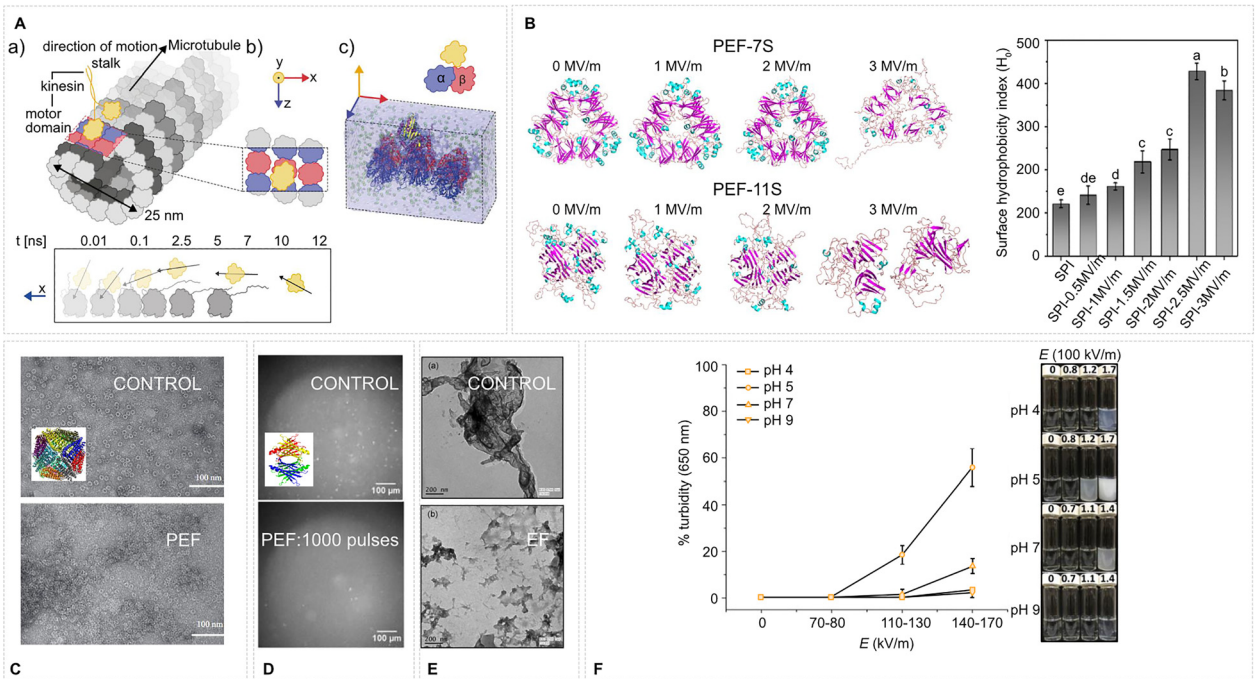

Fig. 10 EFs affect protein–protein interactions. (A) A kinesin motor domain on a segment of an MT is detached within a few ns by a 100 MV m^{-1} EF in MD simulations. Adapted with permission from ref. 225. © (2023) Elsevier, (B) An EF disassembles protein isolate complexes in MD simulations which is corroborated by an increase of surface hydrophobicity in experiment (PEF firing frequency 1000 Hz, bipolar square wave: 40 μs pulse, 200 μs gap, 40 opposite polarity pulse, N = 25 pulses) as probed by ANS fluorescence – both effects are EF strength-dependent. Adapted with permission from ref. 180. © (2024) Elsevier. (C) Transmission electron microscopy evidences that an EF (2 + 2 μs bipolar pulses, 1 MV m^{-1}, firing frequency 2 kHz) causes the disassembly of ferritin cage-like structures. Adapted with permission from ref. 141. © (2021) Elsevier. (D) A 120 MV m^{-1} (1 ns pulse width, 1.7 Hz firing rate, N = 1000 pulses) pulsed EF promotes degradation of transthyretin aggregates. Adapted from ref. 226 – CC BY 4. (E) Transmission electron microscopy images of human serum albumin fibrillar solutions: (a) without an applied EF, and (b) after exposure to an EF of approximately 8 MV m^{-1} for 10 min. Adapted with permission from ref. 227. © (2014) IOP. (F) Turbidity, reporting protein aggregation, of ovomucin-depleted egg white solutions (10% w/w, pH 4–9) after PEF treatment at varying EF strengths, while maintaining a constant specific energy input W_{spec} = 713 kJ kg^{-1}. Adapted with permission from ref. 228. © (2017) Elsevier.

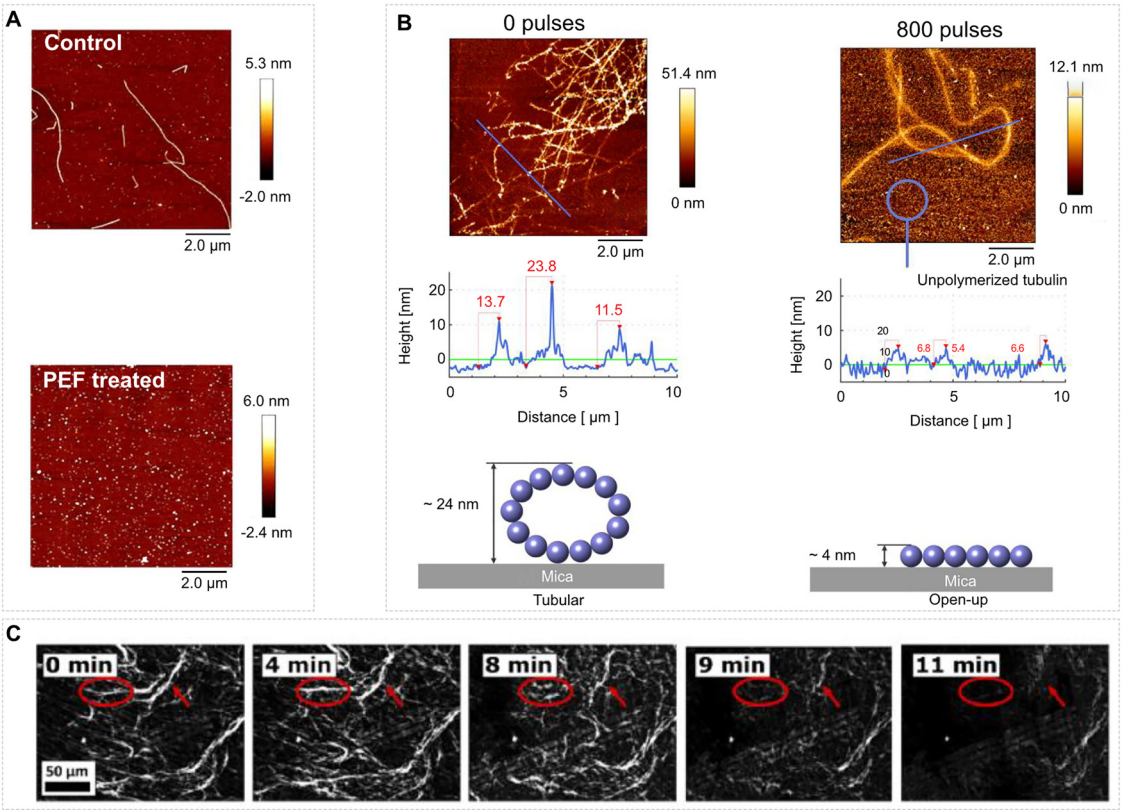

Fig. 11 Imaging of EF effects on protein fibers: (A) AFM imaging of the effects of pulse electric treatments of fiber-forming proteins. Sup35NM amyloid fibrils before and after PEF treatment (2 MV m^{-1}, 10 pulses, 1 ms pulse duration, 1 Hz firing frequency) – adapted from ref. 238 – CC BY 4. (B) Control sample of self-assembled tubulin and the self-assembly from a tubulin treated by a PEF (2 MV m^{-1}, 800 pulses, 10 ns pulse duration, 1 Hz firing frequency) – adapted with permission from ref. 21. © (2019) Wiley. (C) Intense picosecond (subTHz) electric pulses cause MT fragmentation (40.9 MV m^{-1}, 1 ps pulse duration, 1 kHz firing frequency). Here we show a time dependence of this process captured using fluorescence microscopy – adapted from ref. 25 – Open Access license of The Optical Society/OPTICA.

In the case of PPIs in amorphous-protein aggregation, aggregates of amorphous proteins were subjected to an oscillating EF. When their field response was observed using time-resolved polarized optical microscopy, they revealed the disintegration of large aggregate clusters as well as field-induced deformation, reorientation, and enhanced polarization. Further, amorphous aggregate suspensions' collective microscopic dynamics were investigated using small-angle dynamic light scattering. The intensity auto-correlation function exhibited field-enhanced local oscillations that were associated with two distinct elastic moduli – drawing attention to the potential of EFs to regulate protein-aggregation processes.[237]

PEFs (0.1–3 MV m^{-1}, μs bursts) are widely used in food processing to affect PPIs: ovalbumin at neutral pH aggregated modestly, whereas at pH 4 or 9 it remained monomeric.[228] Soybean proteins showed a biphasic trend, where 0.5–1.5 MV m^{-1} unfolded tetramers and released subunits, but $\geq$2 MV m^{-1} exposed hydrophobes and thiols that re-cross-linked the proteins[180] (see also Fig. 10B). Time-resolved fluorescence and Ellman's assays pinpointed radical generation as a secondary pathway, indicating indirect electrochemical effects of EFs taking place as well (see Section 3.2). For the allergen tropomyosin, 0.5–1 MV m^{-1} bursts opened coiled-coil dimers and raised IgE binding by ~30%, whereas prolonged or stronger treatment compacted the structure and lowered immunoreactivity.[134]

Together, these studies demonstrate that intense static, pulsed or THz-frequency EFs can decisively remodel protein–protein contacts (from weakening kinesin–tubulin binding and accelerating actin growth to fragmenting amyloids) highlighting a versatile, rapidly switchable handle for manipulating quaternary, multimeric and polymeric protein structure *in vitro* and *in vivo*: the selective dismantling of amyloid fibrils or weakening of motor-track contacts suggests non-invasive anti-aggregation therapies and neuromodulation strategies.[133,237] Conversely, reinforcing or creating PPIs with tuned EFs could stabilise fragile enzyme assemblies in biosensors or power nanobiomachines. In agri-food technology, PEFs were demonstrated to deliver chemical-free control of gel texture, solubility and allergenicity.[134,180,228]

2.5.2 Effects on protein–ligand binding. Precise binding of proteins to their ligands, substrates, and co-factors underlies essential biological functions – from enzyme catalysis and metabolic regulation to signal transduction. Emerging evidence indicates that intense external EFs can modulate these interactions by reshaping protein conformations and intermolecular forces (Fig. 12). MD simulations have revealed atomic-level effects: for example, applying a static field of 30 MV m^{-1} to a GPCR

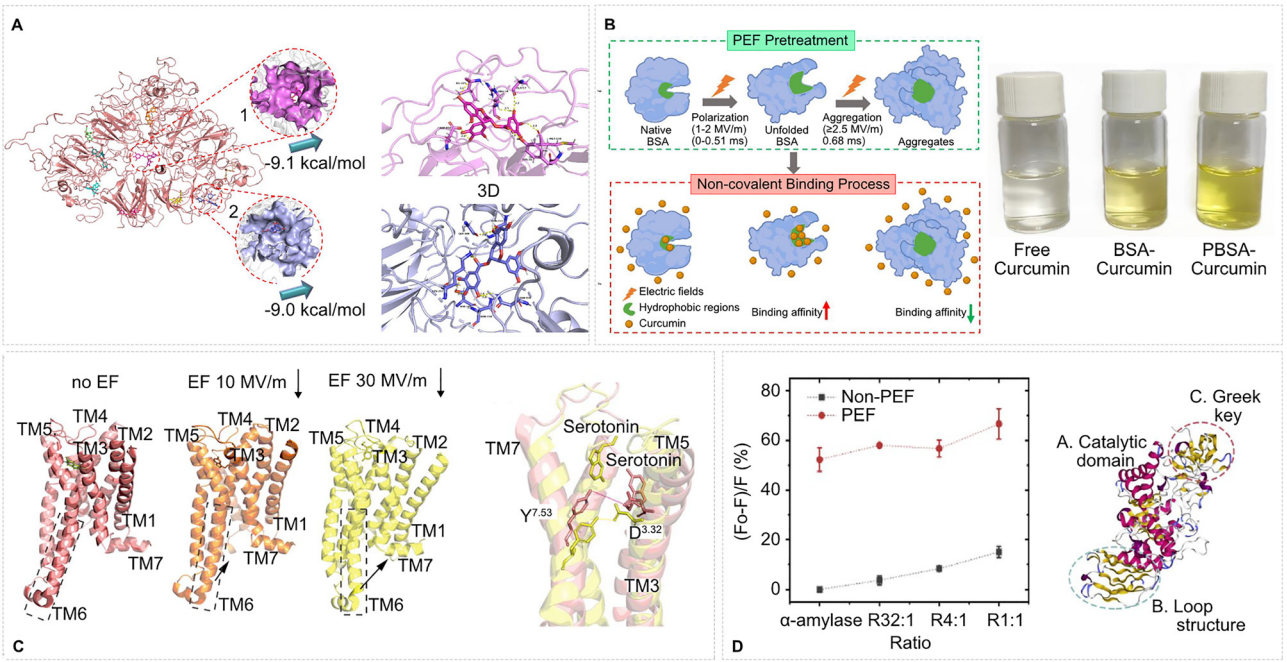

Fig. 12 Protein–ligand interactions modified by EFs. (A) In PEF-treated (1 MV m^{-1}, 40 μs pulse, firing frequency 1 kHz, N = 20 pulses) pea protein isolate, the ligand (EGCG – epigallocatechin-3-gallate) occupies two high-affinity pockets (sites 1–2; ΔG = −9.1/−9.0 kcal mol^{-1}), expanding the total docking sites (obtained from molecular modeling) from four in the control structure (no EF – not shown) to ten and increasing hydrophobic contacts from five to twelve through newly exposed residues such as Pro457 and Trp[129]. Adapted with permission from ref. 126. © (2023) Elsevier. (B) Schematic representation of the relationship between the curcumin-binding capacity and structural properties of BSA after PEF treatment. Photos: Visual inspection of free curcumin solution (left), BSA curcumin complex solution (middle) and PEF-treated BSA curcumin complex solution (right). Adapted with permission from ref. 179. © (2022) Elsevier. (C) Snapshots of the 5-HT1AR-serotonin complex at 600 ns in (from left) no EF, 10 MV m^{-1} EF, and 30 MV m^{-1} EF, serotonin is shown as sticks, and (right) overlay of 5-HT_{1A} receptor structures from no EF (pink) and 30 MV m^{-1} EF system (yellow) MD simulations, spotlighting the conformational shift at the $D^{3.32}$–$Y^{7.53}$ lock. Adapted with permission from ref. 135. © (2025) Elsevier. (D) (Left) Relative intrinsic fluorescence quenching of α-amylase/pectin complexes after PEF treatment. The ordinate shows the fractional decrease in fluorescence, $(F_0 - F)/F_0$, while the abscissa lists the mass ratios of α-amylase to pectin (R32 : 1, R4 : 1, R1 : 1). PEF-treated samples (red circles) exhibit markedly greater quenching than non-treated controls (black squares), data represent mean ± SD (n = 3). (Right) Structure of α-amylase. Adapted with permission from ref. 167 © (2020) Elsevier with permission.

(5-HT_1A receptor)–serotonin complex caused an inward shift of an α-helix (TM6) that perturbed serotonin binding and receptor activation.[135] By contrast, a mixed quantum-classical simulation of myoglobin covalently binding CO under a 1 GHz microwave EF found no significant perturbation at field strengths far below intrinsic molecular forces, implying a threshold EF strength is required to alter ligand-binding kinetics.[190] Experimentally, a variety of spectroscopic techniques (fluorescence quenching assays, CD, UV-Vis absorption, *etc.*) have been used to monitor field-induced changes in protein structure and binding. These studies show that EFs can both stabilize and disrupt binding interactions depending on conditions. For instance, *in situ* CD and fluorescence of β-lactoglobulin under moderate AC fields revealed field-dependent unfolding with increased surface hydrophobicity (ANS dye binding) yet a preserved affinity for its native ligand (retinol), indicating a distinct partially-unfolded state retaining co-factor binding.[178] Terahertz irradiation of serum albumin (3–4 THz) similarly induced subtle secondary-structure alterations and dose-dependent changes in hormone (progesterone) binding capacity.[239] In the context of PEFs – a non-thermal high-intensity treatment – numerous studies demonstrate enhanced binding or reaction outcomes due to field-induced protein polarization and partial unfolding. PEF pretreatment of BSA at 1.5 MV m^{-1}, for example, increased the curcumin–BSA binding constant by nearly 7-fold by exposing buried hydrophobic pockets, whereas exceeding 2.5 MV m^{-1} led to over-denaturation and weakened affinity.[179] Likewise, PEF-assisted Maillard reactions of BSA with glucose or starch yielded higher glycation degrees and superior emulsifying properties, attributed to field-driven unfolding that increased reactive site exposure (with optimal EF ranges of 0.3–1.5 MV m^{-1} before deleterious effects set in).[240,241] On the other hand, intense PEFs can impair function: applying 2 MV m^{-1} to enzyme–polysaccharide complexes caused aggregate β-sheet formation and an ∼80% loss of α-amylase activity, underscoring the disruptive effect of field exposure.[167]

These findings illustrate that strong EFs are potent modulators of protein–ligand/substrate binding, capable of enhancing interactions (by transiently altering conformations to improve ligand accessibility and binding affinity) or inhibiting them (*via* induced unfolding or misfolding). This knowledge opens up opportunities for innovative applications – from non-thermal control of enzymatic reactions and protein processing (*e.g.* tailored glycation and improved drug/nutrient binding) to

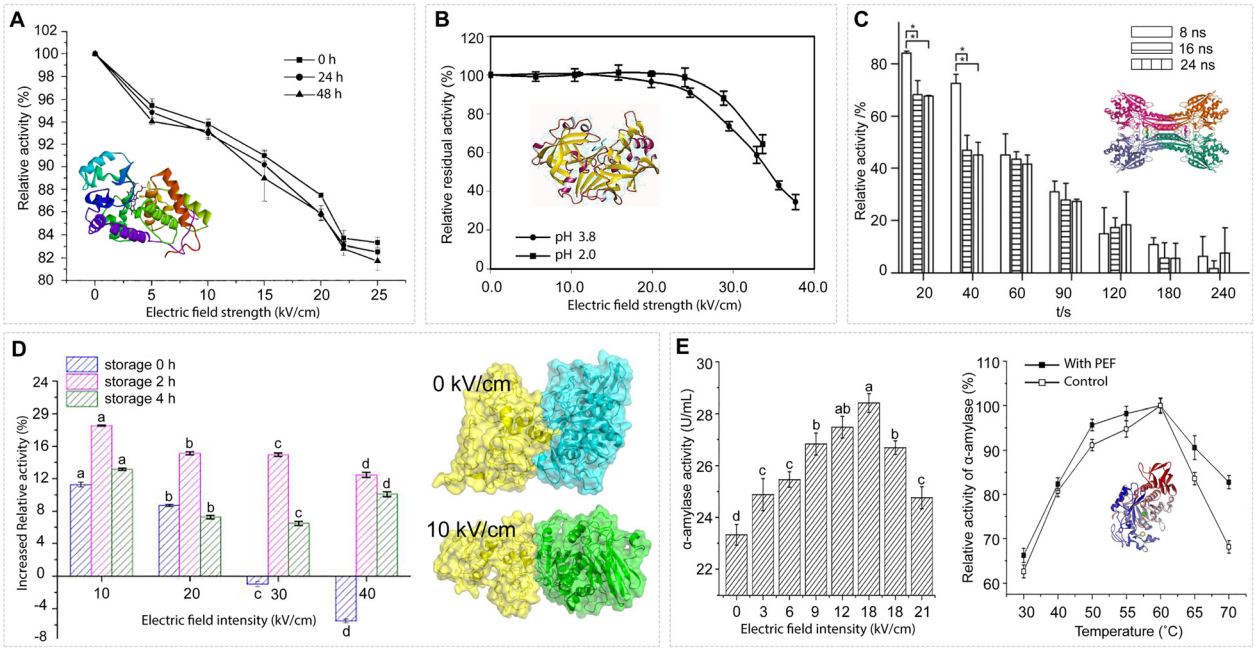

Fig. 13 EF effects on proteins' enzymatic functions. (A) Inactivation of horseradish peroxidase (HRP) exposed to EF strengths varying from 0.5 to 2.5 MV m^{-1} with 207 pulses during storage at 4 °C, respectively (measured immediately, 24 h, or 48 h after PEF treatment). The treatment temperature did not exceed 40 °C. Adapted with permission from ref. 242. © (2005) Elsevier. (B) Inactivation of pepsin by PEFs. The width and total treatment time were 2 μs (bipolar pulses) and 126 μs, respectively. The media are 7.5 mM HCl with a pH of 2.0 and an electrical conductivity of 0.391 S m^{-1}, and a water–phosphate–acetate mixture with a pH of 3.8 and an electrical conductivity of 0.345 S m^{-1}. Adapted with permission from ref. 162. © (2004) American Chemical Society. (C) The relative activity of CPG2 after nsPEF exposure; relative activity (%) as a function of total exposure time t (s). *$p < 0.05$. Adapted with permission from ref. 243. © (2015) Elsevier. (D) Changes in the enzyme activity of alcalase after PEF treatment for different storage times. Data were expressed as the mean ± SD, $n = 3$. *a*, *b*, *c* indicated that the enzymatic activity of alcalase was significantly different ($p < 0.05$). The docking model between a substrate (casein) and the alcalase molecule was generated by MD simulations under EF strengths of 0 and 1 MV m^{-1}. Adapted with permission from ref. 244. © (2022) Elsevier. (E) Left: Effect of PEF treatment (pulse width, 2.5 μs; frequency, 1128 Hz) at different EF intensities on the enzymatic activity of α-amylase (0.2 mM phosphate buffer, pH 6.0; enzyme concentration, 23 U mL^{-1}). Error bars represent standard deviation. The different letters mean the data of two samples are significantly different ($p < 0.05$). Right: Temperature dependence of α-amylase enzymatic activity (enzyme concentration, 23 U mL^{-1}) with and without PEF treatment. PEF treatment: EF strength, 1.5 MV m^{-1}; flow rate, 100 mL min^{-1}; pulse width, 2.5 μs; frequency, 1128 Hz. Error bars represent standard deviation. Enzyme activity at the optimum temperature is considered 100%. Adapted with permission from ref. 245. © (2016) Springer Nature.

the remote tuning of receptor activation and protein function in biomedical and biotechnological settings.

2.6 Effects on additional protein functions

2.6.1 Enzymatic function. A large class of proteins function as enzymes to catalyze essential biochemical reactions in living systems and industry, exhibiting remarkable specificity and efficiency.[246] Enzymatic activity depends on the protein's structure and chemical environment, so external perturbations like an intense EF can alter function by inducing conformational changes or modifying active-site properties. For example, simulations show static fields can lower the pK_a of a catalytic cysteine (thioredoxin Cys35) by altering its electrostatics,[182] and experimental nanosecond 1 MV m^{-1} pulses can eject a Zn^{2+} cofactor from a zinc-dependent enzyme, inactivating it (Fig. 13C) without global unfolding.[243] Experimentally, PEFs often inactivate enzymes non-thermally by inducing partial unfolding. Significant activity loss with corresponding secondary and tertiary structure changes has been observed in many enzymes: *e.g.*, horseradish peroxidase and papain show reduced activity (on the order of 20–50%) and α-helix content after PEF treatment, despite minimal heating,[162,242,247] see Fig. 13A and B. In milk, a PEF achieved ~90% inactivation of plasmin protease under mild conditions.[248] The sensitivity to a PEF is enzyme-specific: some enzymes (lipase, glucose oxidase) lose >70% activity while others (alkaline phosphatase) are much more resistant or even activated (lysozyme, pepsin) under high-field pulses.[249] Similarly, exposure to microwave-frequency fields (~10 GHz) can irreversibly inactivate thermophilic enzymes *via* structural rearrangements, independent of bulk heating.[250] Furthermore, PEFs can affect enzyme function within complex food matrices: in α-amylase–pectin mixtures, PEFs caused ~80% activity loss and promoted aggregation of enzyme–polysaccharide complexes.[167] Mechanistic studies point to specific molecular targets: a PEF was shown to act on tryptophan residues in α-amylase's active site, disrupting its conformation and reducing activity by ~70% without the aggregation seen in heat denaturation.[127] Even extremely high-frequency fields (~100 GHz) can subtly affect enzymes: for instance, 100 GHz irradiation slightly reduced alkaline phosphatase activity and destabilized antigen–antibody binding when the proteins were free in solution (but not when immobilized), suggesting effects *via* altered molecular rotations

or vibrations.[164] Conversely, under certain conditions EFs can enhance enzymatic activity, see Fig. 13E. A moderate (0.1 kV m^{-1}) oscillating field at low frequency (1–60 Hz) increased α-amylase activity by up to ~41%, an effect disappearing at higher frequencies.[246] Likewise, a PEF at ~1.5 MV m^{-1} boosted α-amylase activity by ~22%, broadening its temperature optimum and improving kinetic parameters (lower K_m, higher V_{max}), concomitant with a slight increase in the α-helix structure.[245] A mild PEF (~1 MV m^{-1}) also enhanced alcalase protease activity (~11%), apparently *via* partial unfolding that improved substrate accessibility, as supported by molecular docking analysis.[244] These findings carry important implications. PEF-based enzyme inactivation has clear applications in food preservation: it can deactivate spoilage enzymes or unwanted enzymatic activity while preserving food quality, as demonstrated by non-thermal PEF treatments that maintain flavor/nutrients[242] and effectively inactivate enzymes like plasmin in milk.[248] PEFs can also halt enzyme-driven processes at desired endpoints; for example, ~70% PEF inactivation of a commercial protease mix (Protamex) was sufficient to stop protein hydrolysis in a food matrix without heating.[251] On the other hand, gentle field treatments can be harnessed to improve beneficial enzymatic processes: pretreating whey protein with high-voltage pulses greatly increased its subsequent digestibility by trypsin/chymotrypsin, boosting the yield of bioactive peptides.[252] Thus, depending on EF strength and exposure, EFs can either diminish enzyme function *via* structural disruption (or cofactor removal) or enhance it by modulating conformation, offering a novel means to control enzymatic activity in various applications.

2.6.2 Membrane protein function: Transmembrane proteins. Another important application of EFs in transmembrane proteins lies in electroporation, which, in and of itself, is becoming more important in the expanding fields of nano-medicine and in electrochemotherapy. This rupture of a phospholipid-bilayer membrane – pivotal to the structural stability of many biomaterials – can be brought about by a strong externally-applied EF. This connects the cytosol and cytoplasm, increasing the permeability for water, and, possibly, ions that are not typically permitted through in most cell lines,[253] of course, this depends on the limiting solubility of the solute in the aqueous solvent,[254] and is affected by the electrostatic environment[255] inside such cells for conductivity[256] and diffusivity.[257] Indeed, the manipulation of electroporation may allow for drug-free therapies in medicine and ion transport in desalination, and a particular ''case study'' of such electroporation phenomena in transmembrane proteins lies in aquaporins. In mammalian life, eleven different aquaporins (AQPs) have been reported,[258] and they all play different roles in different locations of the body. In humans, urea production and water retention in the kidneys[259] are among the most important AQP-controlled processes; also if the protein is genetically defective, it can lead to diabetes[260] and polyurea. In recent times, Marracino *et al.* applied MD with an EF to render an electropore stable in h-AQP4 for extended periods of tens of nanoseconds, seeing at first hand novel phenomena of electropore formation within transmembrane proteins, as opposed to the phospholipid bilayer.[261] There, the tetramer configuration can facilitate, under certain field-mediated situations, the formation of this 'fifth-pore' along the tetramer's axis; this arises due to dipole coupling of some protein residues with the applied field[261] (*vide infra*). The approach was adapted to give rise to a stable pore,[261,262] inside a maintaining EF and a sustaining EF. It was remarked, in passing, in ref. 261, that this pore metastability brings about occasional ion-permeation events *via* pores. As Marracino *et al.* found, it is the ready dipole alignment of ASP69 which brings about the action of membrane poration *per se*.[261] We note that Bernardi *et al.* performed more detailed MD studies on field-driven ionic permeability through these h-AQP4 electro-pores, including a mechanistic and statistical study of permeation events,[263] building on analysis techniques of diffusivity and permeability calculations of ref. 264. Recently, ionic permeation has been found through a pore formed in a human–AQP4 transmembrane protein subject to a static EF.[263,265] Recently, CaCl salt has been studied for AQP ionic conductivity through electropores,[265] although this study was focussed more specifically on dwell-time and mean-first-passage-time distributions.

Similarly in ref. 266 it is shown that PEFs can induce pores in the voltage-sensor domains of different voltage gated transmembrane channels. Such fields can create conductive pores which evolve into complex pores stabilized by lipid molecules followed by unfolding of the voltage sensor domain from the channel. The mechanism is related to the degree of hydration of the sensor: the more hydrated the sensor is, the more electrostatically favorable for the entry of ions, and the more easily it porates (Fig. 14).

Experimental EF effects were demonstrated on membrane proteins as part of isolated membranes or in cells. One class of works exploited electro-optical approaches mentioned above. A common target protein was bacteriorhodopsin in purple membrane, in which a pulsed EF induced pH change,[168,269,270] structural effects[112,115,171,172] and DC- or AC-fields caused conformational changes.[110,169,170] Another class of works focused on oscillating EF effects on ATPases: a pulsed EF drove the ATP synthesis[271] and AC fields drove cation transport across the membrane in a resonant-like manner[272] (Rb^+,[273] Na^+.[274] Follow-up works generalized the concept and proposed that enzymes can harness energy from various EF waveforms,[275–279] including stochastic ones,[280–282] using electroconformational coupling model.

2.6.3 Photonic/luminescence functional properties. Proteins often exhibit intrinsic and extrinsic fluorescence or luminescence, which are instrumental for probing their structure and function *in vitro* and *in vivo*.[283] These photonic properties (emission intensity, spectrum, polarization, *etc.*) are sensitive to the protein's environment, and external EFs can markedly influence them. Strong static EFs, for example, can perturb the energy levels of a protein chromophore (Stark effect), leading to spectral shifts or fluorescence quenching if the excited-state dipole differs from the ground state.[283] Insights from theory and MD simulations suggest that extremely high field strengths (~10^7 V m^{-1}) are often required to observe non-thermal effects on protein electronic states.[284] Notably, proteins' own internal electrostatic fields of similar magnitude can

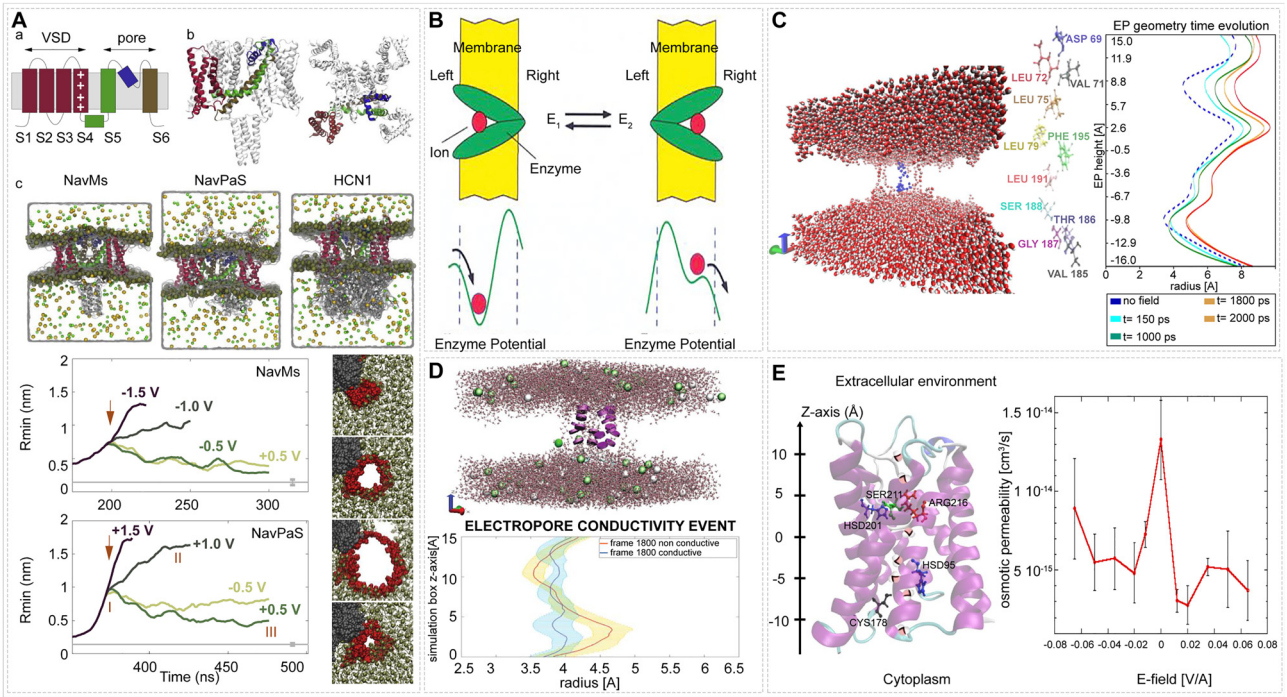

Fig. 14 EF effects on membrane protein functions. (A) Structure of the voltage-gated ion channels (VGICs); progression of the radius of complex pores generated by the increasing applied EF. Adapted with permission from ref. 266. © (2020) Elsevier. (B) The Michelis Mentin enzyme will behave like a Brownian motor. The E_1 to E_2 transition can be induced by an applied EF. Adapted with permission from ref. 267. © (2003) Association of Asia Pacific Physical Societies. (C) Central intraprotein electropore; evolution of the electropore's shape during the simulation with an applied EF. Adapted from ref. 268 – CC BY. (D) Conduction through an endogenous channel; approximate schematic of the electropore-channel radial shape. Adapted with permission from ref. 263. © (2019) Royal Society of Chemistry. (E) Depiction of layout of AQP4 and osmotic permeability static-field pulses applied at various EF strengths (V/A). Adapted from ref. 261 – CC BY.

also modulate chromophore fluorescence by restricting molecular motions.[285] Experimentally, EF effects on protein fluorescence have been investigated using various approaches. Electrofluorescence spectroscopy under DC fields reveals field-induced fluorescence quenching in GFP mutants (attributed to an EF-enhanced non-radiative decay rate).[283] In the microwave regime, intense alternating fields (GHz frequencies) induce changes in fluorescence emission anisotropy, indicating orientational effects beyond ordinary thermal heating.[284] Conversely, static fields up to 10^7 V m^{-1} applied to immobilized proteins (*e.g.*, the metalloprotein azurin) caused no detectable change in intrinsic tryptophan fluorescence, implying no significant EF-induced unfolding.[286] Such results demonstrate that many proteins can withstand very strong EFs without loss of function, a promising sign for bioelectronic applications that integrate proteins into high-field environments.[286] At the same time, the ability to tune protein luminescence with external fields provides a novel avenue for controlling optical signals and developing advanced spectroscopic probes of protein dynamics.[283,284,286–288]

3 Indirect effects of EF exposure

The EF applied to protein solutions can impart a variety of indirect stresses on the proteins *via* physical and chemical changes in the surrounding medium. These indirect effects are distinguished from the direct interactions of the EF with the protein's molecular structure described in the sections above, and instead involve secondary phenomena like heating, fluid motion, shockwave generation, electrolysis-driven pH shifts, reactive chemical species formation, and gas bubble formation. Such effects come into play for high-field exposures across the spectrum of DC, AC, pulsed, radio-frequency (RF), and microwave fields, especially at field strengths on the order of 0.1 MV m^{-1} and above. In this section, we review the major indirect mechanisms by which intense EFs can influence protein structure and stability. We exclude cases that involve plasma formation or dielectric breakdown (sparking), focusing instead on sub-breakdown conditions where the field-induced effects are non-ionizing. The indirect pathways are categorized into electrophysical effects – arising from the physical consequences of the EF (such as thermal and mechanical perturbations) – and electrochemical effects – arising from field-induced chemical reactions or species in the solution. All types of proteins (enzymes, structural proteins, antibodies, *etc.*) can be susceptible to these indirect stressors, although their specific responses may vary depending on factors like stability, size, and environment.

3.1 Indirect electrophysical effects of EFs

3.1.1 Heat generation. One of the main indirect effects of intense EFs in conductive solutions is Joule (ohmic, resistive) heating. When an EF with field strength E is applied across a

medium with conductivity σ, heat is generated at a rate $P = \sigma E^2$. Similarly, microwave fields (GHz range) deposit energy in lossy dielectrics (*i.e.*, those with imaginary part of relative permittivity $\varepsilon'' > 0$, such as water) *via* dipolar rotation, leading to dielectric heating at a rate $P = \omega\varepsilon_0\varepsilon'' E^2$, where ω is the angular frequency of the EF, and ε_0 is the permittivity of vacuum. At EF strengths of 0.1 MV m^{-1} or higher, this can rapidly raise solution temperatures by tens of degrees Celsius unless controlled. Proteins are sensitive to temperature: many enzymes and antibodies unfold between 40–80 °C.[294] For instance, Zhao *et al.* showed that strong EFs applied in capillaries caused measurable temperature rises and corresponding unfolding of myoglobin, cytochrome *c*, and carbonic anhydrase II, with more stable proteins requiring more heat to denature.[295] Localized heating near electrodes or in hotspots can further intensify damage,[296] leading to precipitation or aggregation. Even short pulses can generate non-uniform heating in boundary layers. All these effects have to be mitigated (cooling, and short pulse protocols) or accounted for using electromagnetic and thermal simulations[297] as well as experimental temperature monitoring[298] isolating true EF effects from heat artifacts.

3.1.2 Heat and EF induced flows. Intense EFs can induce fluid motion through several mechanisms that contribute to indirect effects on proteins.[299] Key flow types include: (1) electrothermal convection from temperature gradients due to Joule[300] or dielectric[301,302] heating or thermophoresis;[303] (2) electrokinetic flows, such as electroosmosis/symmetry-broken electrophoresis and dielectrophoresis.[304–308]

In practice, electroosmotic contributions are strongest when charged interfaces (electrodes, channel walls, bubbles) are present and the electrical double layer can charge within the field period. The characteristic charging time τ_c sets a frequency crossover: for $\omega\tau_c \gtrsim 1$ (often $\gtrsim$10–100 kHz in microscale geometries) AC electroosmosis diminishes markedly, whereas at 0.1–10 kHz it can generate steady vortical flows even at modest fields of order kV m^{-1}.[304–306] Consequently, flow-induced hydrodynamic interactions can be important in concentrated protein suspensions and near-wall geometries where long-ranged flows enhance collision rates and promote field-assisted aggregation or adsorption. In contrast, in dilute bulk solution away from boundaries (typical for many spectroscopic assays), direct electrophoretic/dielectrophoretic and dipolar interactions between proteins are usually the dominant field couplings, while electroosmotic flow mainly enters indirectly by redistributing heat and reactive species.[299,308]

These flows have dual consequences. On the one hand, they improve heat and species transport and mixing, preventing localized extremes of temperature or electrochemically produced species that would otherwise damage proteins. On the other hand, flow also introduces hydrodynamic shear and increases contact between proteins and interfaces, such as gas bubbles or electrodes, where adsorption and unfolding can occur.[309] In summary, EF-induced flows can either protect or damage proteins depending on their magnitude and context. Controlling flow regimes is therefore essential in high-field experimental design.

3.1.3 Shockwaves. Rapid energy deposition by a nanosecond PEF makes the liquid expand faster than it can relax acoustically, launching a shockwave – an abrupt, high-frequency pressure transient. A single 600 ns, 1.3 MV m^{-1} pulse between micro-electrodes produced a 2.5 MHz, >13 kPa wave in saline, confirming that a ns-PEF creates measurable shocks.[310] Peak loads of 10–100 kPa are too small and transient to unfold globular proteins, which typically require sustained pressures $\geq$200 MPa.[311] More damaging is the cavitation seeded during the negative-pressure tail of the wave: nanosecond optical diagnostics have visualised voids at −20 to −30 MPa in pulsed needle-electrode fields.[312] Imploding bubbles reach 4000–5000 K and hundreds of bar, emitting radical species, micro-jets and secondary shocks that can damage biomolecules[313,314] similarly to the electrochemistry processes outlined below. Macroscopic evidence comes from simple vial drops – cavitation appeared within 30 μs and drove antibody aggregation.[315] Atomistic simulations corroborate these findings: while a planar shock compresses proteins elastically, an asymmetric void collapse ejects a nano-jet that leaves the molecule partially unfolded and aggregation-prone.[316] To protect labile proteins against these one can limit pulse energy, degas buffers or potentially add acoustic dampers; conversely, cavitation can be harnessed deliberately for protein unfolding and aggregation, tissue ablation or sterilisation. These mechanisms must be considered when evaluating the effects of intense EFs on proteins.

3.2 Indirect electrochemical effects of EFs

3.2.1 pH change. Intense pulsed (or low-frequency) EFs can force faradaic reactions at electrodes, driving steep local pH shifts:

$$\text{Anode: } 2H_2O \rightarrow O_2 + 4H^+ + 4e^-$$

$$\text{Cathode: } 2H_2O + 2e^- \rightarrow H_2 + 2OH^-$$

Within several ms pulses, when an intense EF is applied driving direct-current, the anodic boundary layer can acidify to low pH while the cathodic layer simultaneously alkalinises to high pH, provided the rate of electrolysis outstrips the local buffer capacity.[317] Such pH changes rapidly protonate or deprotonate ionisable side chains, disrupting salt bridges, neutralising charge balance, and triggering unfolding or aggregation, see the review[318] on general pH dependence of protein stability. For example, in electrospray ionisation capillaries acting as anodes, Konermann *et al.* detected >2-unit pH drops that unfolded cytochrome *c*, evidenced by higher charge-state spectra; raising flow or altering grounding decreased electrolysis and preserved the fold.[319] This demonstrates that apparent EF effects may actually be hidden pH artefacts. Increasing buffer strength often increases electric conductivity and hence current, so H^+/OH^- production scales up and the width of the pH front changes only marginally.[320] Thus ''more buffer'' rarely solves the problem. The pH shifts can be minimized (i) using short bipolar pulses, (ii) adding sacrificial or ion-exchange layers on electrodes,[321] (iii) separating the sample *via* salt bridges,[322] or accounted for by monitoring pH or applying matched chemical controls. Electrode-driven pH excursions, not the EF itself, often

compromise protein integrity under intense EFs. Proper pH monitoring and mitigation are essential before attributing structural changes to direct EF–protein interactions.

3.2.2 Reactive species generation. RXS (X = O, N, S, Cl,...)[323] can be produced by EFs either through faradaic reactions (always present for resistive current at electrode–electrolyte interface)[324] or by an extremely large EF if it leads to shockwaves, cavitation[310,312] and following sonochemistry. Principally, the consequent effect of RXS species on proteins is similar regardless of their origin. At anodic potentials, water oxidation yields $^{\bullet}OH$ which diffuses or dimerises to H_2O_2; cathodic O_2 reduction gives $O_2^{\bullet -}$.[324] Cavitation adds pyrolytic $^{\bullet}OH$ and $^{\bullet}H$, plus $NO^{\bullet}$ in air-filled bubbles.[314] These species consequently produce secondary ROS/RNS that oxidise Met, Cys, Tyr, Lys and backbone α-carbons, raising carbonyl content, cross-linking dityrosine or fragmenting chains.[325,326] We recently showed[324,327] that BSA remained largely intact under a microsecond PEF alone, whereas the addition of exogenous H_2O_2 markedly increased oxidation signals.[324] This indicates that, for these pulse conditions, protein damage is dominated by indirect ROS chemistry (electrochemically generated) rather than by a direct EF-induced conformational disruption.

3.2.3 Bubble formation. Electrolysis, boiling hotspots and cavitation all inject gas–water interfaces. Proteins adsorb to the surfaces of stable bubbles, unfold as hydrophobic cores contact the gas phase and desorb as aggregation-prone species. Cryo-EM studies reveal ~80% denaturation of fatty-acid synthase at the air–water interface,[328] while "do-not-drop" tests linked vial impact to bubble-induced protein particles *via* cavitation and radical chemistry.[315] In EF devices, anodic O_2 and cathodic H_2 bubbles combine pH extremes with interface stress, often leaving crusts of precipitated protein on electrodes. Degassing, pulse trains that allow gas purge, and low-level surfactants that shield interfaces are practical safeguards.

Each indirect pathway: heating, electro-hydrodynamic flows, shock-cavitation, pH drifts, ROS/RNS reactions and bubble interfaces – can appear simultaneously in a high-EF protocol. Disentangling them through temperature probes, pH indicators, radical scavengers, acoustic sensors, *in situ* imaging and spectroscopy enables rational process design, whether the goal is to dissect the mechanism of EF action or for biotechnological or industrial applications.

4 Discussion

4.1 EF strength and timescale: their scaling and (mis)match between simulations and experiments

In most of the works aiming to probe the direct effects of EFs on proteins, the fields have to exceed certain threshold EF strength for the effect to manifest, see Fig. 15. In many cases, that limit would be EF strengths on the order of hundreds of MV m^{-1}, although the exact threshold for such effects depends very much on the protein systems and experimental conditions and goes down to 10 kV m^{-1}.[125] It is insightful in this context to consider the strength of EFs that occur naturally in cells and proteins. Typical membrane potentials across the cell membranes of eukaryotic cells are approximately 100 mV, which if one assumes a membrane thickness of about 4 nm[329] yields field strengths of up to tens of MV m^{-1}. EFs inside the catalytic sites of enzymes reach EF strengths of GV m^{-1} and beyond.[34,41,222] Therefore, we do not focus on weak and ultra-weak EF (< 0.1 kV m^{-1}) effects, where direct effects of EF on molecules are expected to be negligible compared to thermal electric noise. For this reason, the weak

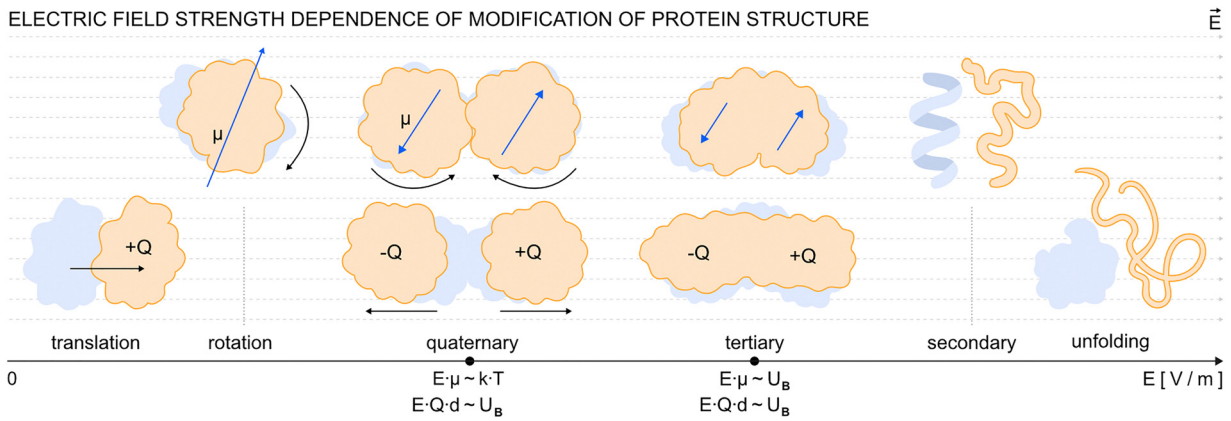

Fig. 15 Primary EF effects on proteins depend on EF strength E and protein structure. The geometrical direction of effects is consistent with the fact that the EF vector is pointing from left to right. The protein always undergoes translation (electrophoretic force) as long as it has non-zero effective electric charge Q. Rotational force is also acting on the protein proportional to the dipole moment μ of the protein (blue arrow). Translation and rotation effects of the EF on whole proteins (rigid body motions) are taking place at any field strength values. When the torque magnitude $T = E{\cdot}\mu$ significantly exceeds the energy due to rotational thermal motion (kT), the rotation becomes deterministic. In a multimeric protein complex, the translational force and rotation force due to the EF act also on the local charges Q_L and dipoles, respectively, of individual subunits. If the EF force is higher than some threshold force, (*i.e.* interaction energy between the EF and charges and dipoles and overcomes the binding energy (E_B) between the monomer), it can cause disassembly of the complex, hence disrupting the quaternary structure. Within a protein, EF effects on the local charges and dipoles can cause deformation of the protein and affect tertiary structure. Similarly, the EF can affect the secondary structure and a very high EF strength can lead to protein partial unfolding and denaturation. One has to keep in mind that the real picture is statistical: the thresholds are not sharp since the EF changes the probability of events.

electromagnetic field effects on biological systems present major controversies in the bioelectromagnetic research and have been a focus of other reviews.[330–338]

Both computational modeling and experimental studies consistently demonstrate the influence of EFs on proteins, with clear evidence of translational and rotational motion, as well as strong indications of EF-induced changes in secondary, tertiary, and quaternary structures. However, a comparison of EF strengths and timescales used in these two approaches (Table 2 *vs.* 3) reveals substantial discrepancies. MD simulations typically employ EF strengths that are significantly (often several orders of magnitude) higher than those used in experiments, and they operate over much shorter timescales. These differences arise from fundamental limitations inherent to molecular simulation methods. MD simulations are restricted to nanosecond-to-microsecond timescales due to computational cost, which necessitates the use of elevated field intensities to induce observable structural changes within such brief periods. Furthermore, the systems modeled in MD are highly idealized: they are small in size and lack real-world complexities such as dislocations, grain boundaries, impurities, and environmental heterogeneity (*e.g.*, variable solvent conditions). The use of empirical interatomic potentials (force fields), which approximate rather than fully capture quantum interactions, further limits accuracy. Additionally, temperature control mechanisms such as thermostats may artificially suppress slow conformational dynamics, further limiting the observable impact of low-intensity fields. As a result, simulations conducted at experimentally realistic field strengths, but at significantly smaller durations, frequently show only limited effects, such as electrophoretic motion, without substantial conformational changes. To overcome these limitations, MD simulations often rely on stronger EFs to accelerate rare events – such as folding, unfolding, or large-scale domain reorientation – that would otherwise occur over milliseconds or longer. This approach enables researchers to probe mechanisms of field-induced structural change within accessible simulation windows. Thus, the application of higher EF strengths in MD simulations, beyond those typically used in experimental settings, is a practical necessity driven by limitations in accessible timescales, system sizes, and the fidelity of current force fields. Although the quantitative thresholds for structural changes observed in simulations may not align directly with experimental values, the underlying mechanistic insights remain highly valuable. Bridging this gap requires the integration of multiscale modeling approaches, the refinement of interatomic potentials, and the development of scaling frameworks that enable a more accurate translation of computational findings into experimentally relevant predictions.

From a purely academic perspective, one approach is to bring the experimental time scales in line with the ones of simulation. That can be done using fast and ultra-fast spectroscopy techniques[339,340] and advanced ultra-fast single molecule or super-resolution imaging and microscopy techniques,[341,342] see Fig. 16 for a graphical overview of the variety of systems used to expose the proteins to EFs. For the advanced techniques to serve the research on EF effects on proteins, it is necessary to integrate them with EF exposure systems so that the effects can be analyzed in real time during the EF pulse and also shortly after to match the short simulation time scales. Still, there will be a physical limit to the strength of an EF that can be applied for a water-based protein sample for a given time before dielectric breakdown occurs. Although the dielectric strength for distilled water (at 25 °C and normal atmospheric pressure) is approximately 30 MV m^{-1} for a static (long duration) field, this threshold increases if the field acts only for a short time. For instance, small area and small gap systems can hold up to 100 MV m^{-1} up to 100 ns and up 400 MV m^{-1} up to 20 ns[343] and this threshold might depend on conductivity.[344]

However, for practical applications, one might need to use longer duration electric pulses and lower EF strength. In that case, the molecular modeling strategies should comply and extend the time scale to bridge to the experiment. This is possible either by increasing computational power or applying further coarse-grained approaches in the simulations,[345,346] which will enable the analysis of either longer time scales or larger protein systems. Longer simulations will also be able to address the question of the reversibility of the EF-induced conformational and structural changes in proteins.[125,216,266,347,348] To increase the match between molecular modelling predictions and experiments, a promising avenue in a different direction to coarse-grained simulations is to include electronic effects, which are absent in classical MD simulations with standard (non-polarizable) force fields. Including electronic effects can be done by employing polarizable force fields[349] or even more accurate approximations using *ab initio* calculations[350,351] – such effects contribute to the molecular polarization due to external EFs and hence might influence the effects and their thresholds in simulations.

Theoretical considerations bringing together EF strength and time scales required for effects on proteins to take place have the ability to integrate the effects from molecular simulations and experiments. The classical work of EF effects on the chemical reactivity of molecules, including proteins, from a thermodynamic perspective, is that from E. Neumann.[352] We recently proposed a related theoretical approach on a single molecule level and verified its utility in EF-mediated dissociation of a kinesin protein from an MT-model (lattice of tubulin heterodimers).[225] There, we quantified the time needed to detach the kinesin from tubulin in each simulation. To rationalise the observed dependence of kinesin–MT dissociation on EF strength, we recast the detachment process and its timescale within an Arrhenius framework assuming a single energy barrier. While demonstrated on this single protein complex system, we believe that this approach could be used generally for any process where the EF is acting to lower the energy barrier, hence modifying the rate of the process. In the absence of an applied EF, the rate (having units s^{-1}) is (for the particular case in our work,[225] it was the kinesin detachment rate from the MT)

$$k_{\mathrm{OFF}_0} = A \exp\left(-\frac{\Delta E_a}{k_B T}\right), \quad (1)$$

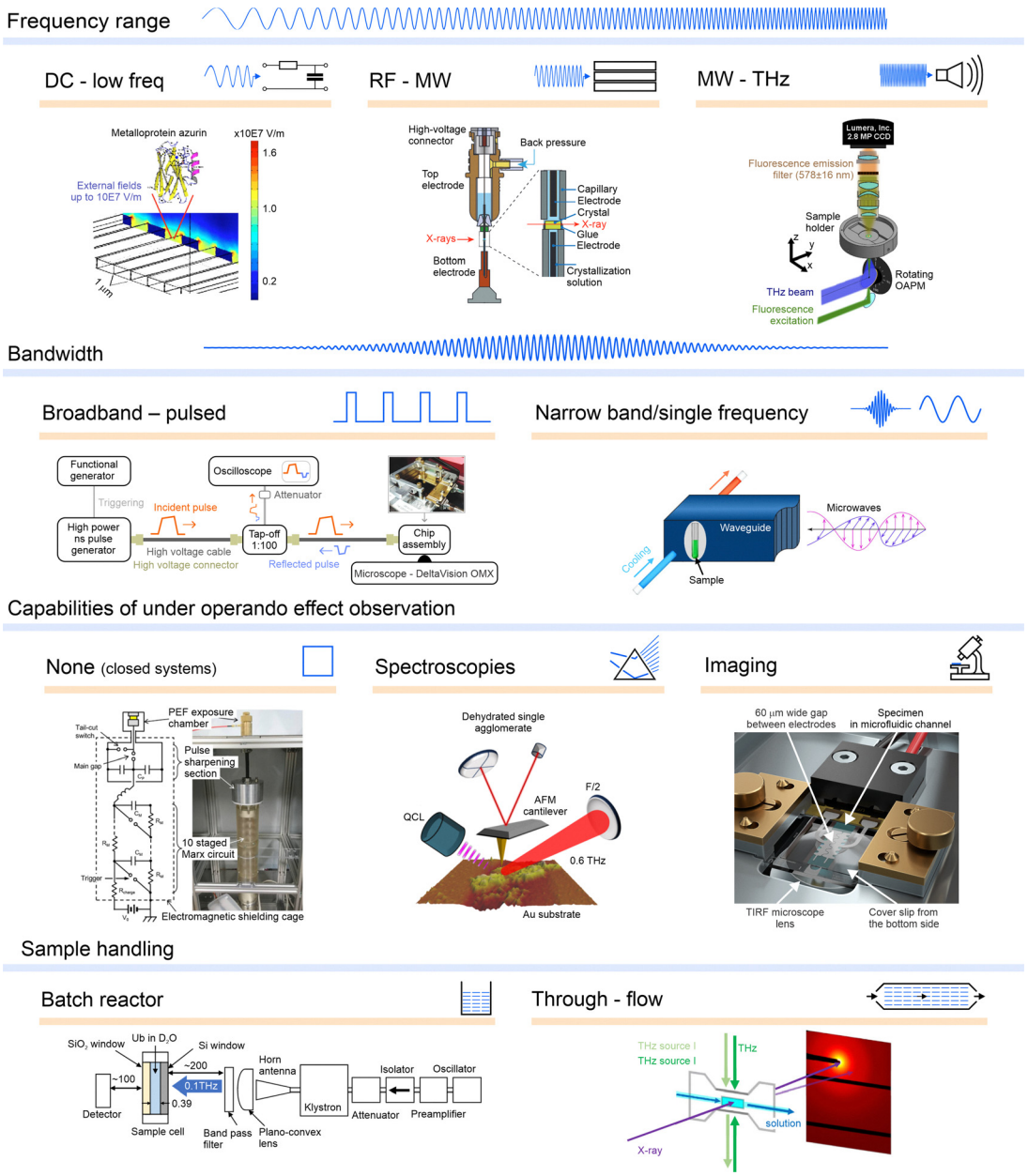

Fig. 16 Exposure systems delivering EFs to protein samples categorized according to the EF frequency range, bandwidth, observation capabilities under *operando*, and sample handling. **Frequency range:** *DC-low frequency*—electrode configurations that impose static or slowly varying fields on proteins, often in capacitor-like arrangement or as coplanar electrodes, such as in ref. 286, reproduced with permission, © (2005) AIP publishing; *RF-microwave*—cells that expose samples to radio-frequency or microwave range signals usually employing transmission lines or waveguides, example from ref. 22, reproduced with permission, © (2016) Springer Nature; *Millimetre-wave/terahertz*—quasi-optical platforms that illuminate proteins with high-frequency EF, as in, *e.g.*, ref. 25, adapted with permission from © Optical Society of America. **Bandwidth**: *broadband, pulsed* – often transmission-line-based geometries for delivering nanosecond–microsecond field pulses with wide spectral content, such as in ref. 289, with permission; *narrow-band, single frequency*—resonator or waveguide, or for low-frequencies even a simple capacitor assemblies, providing monochromatic excitation at a selected frequency, *e.g.* ref. 290, reproduced under CC BY 4. **Under-*operando* observation**: *none*—closed reactors for bulk treatment without real-time monitoring, *e.g.* ref. 226, reproduced under CC BY 4. *Spectroscopies*—field-delivery setups compatible with simultaneous optical, vibrational, or electronic probes such as in ref. 291, adapted with permission from IEEE (©2024); *imaging*—transparent or open-access devices that enable concurrent microscopic visualisation, such as in ref. 292, adapted under CC BY 4. **Sample handling**: *batch reactor*—static chambers in which the sample remains stationary during exposure,[163] adapted under CC BY 4; *through-flow*—flow-through reactors allowing continuous processing under field stimulation and in-line probing,[293] adapted under CC BY 4.

Table 1 Typical orders of magnitude of external EF strengths and forcing protocols across common modalities in protein–EF research. For pulsed modalities we report the pulse width τ_p and the cumulative "on-time" $\tau_{on} = N\tau_p$ (sum over N pulses). Values are approximate and intended as guidance; specific implementations vary with geometry, conductivity, and waveform

Modality	Typical E	Forcing protocol (τ_p, N, τ_{on})	Notes/dominant couplings
All-atom MD (uniform static/AC)	10 MV m^{-1}–10 GV m^{-1}	Continuous (static/AC); $\tau_{on} \approx$ 50 ps–5 μs	High E often used to access rare events on short trajectories; bulk periodic solvent, limited interfaces.[79,138,181]
EF-X in crystals (nanosecond pulses)	50–100 MV m^{-1}	$\tau_p \approx$ 50–500 ns; $N \approx 1$; $\tau_{on} \approx \tau_p$	Direct, ultrafast perturbation; can drive coordinated motions along functional modes.[22]
THz/mm-wave irradiation (pulsed or gated)	0.1 kV m^{-1}–100 MV m^{-1}	Ultrafast: $\tau_p \approx$ 0.5–10 ps; gated trains: $\tau_p \sim$ 0.1–1 μs; $N \sim 10^5$–10^8; $\tau_{on} \sim$ 1 μs–10 s	Couples to collective modes; can be nonthermal or thermal depending on absorption and duty cycle (instantaneous E *vs.* duty).[24,25,163,177,293]
Electrode-based PEF (solutions/cells)	0.1–10 MV m^{-1}	$\tau_p \approx$ 1 ns–1 ms; $N \sim$ 10–10^4; $\tau_{on} \sim$ 1 μs–100 ms	EF direct effects are often mixed with Joule heating and electrode reactions; elapsed treatment time can be $\gg \tau_{on}$.[134,243,343,355]
Low-frequency AC/DC (microfluidics, electrodes)	1 V m^{-1}–100 kV m^{-1}	Continuous/sinusoidal: $\tau_{on} \approx$ 1 s–days (period $\sim$ 1 μs–1 s)	Electroosmosis/ICEO (induced charge electro-osmosis) and electrohydrodynamic flows can dominate near interfaces at low f.[165,173,304–306]

where A is a pre-exponential factor, ΔE_a the activation barrier, k_B the Boltzmann constant and T the absolute temperature. An external EF performs work on the protein system to effectively lower the barrier ΔE_a. Treating the EF as a force acting along the reaction coordinate leads to a modified Arrhenius expression[353,354]

$$k_{OFF}(E) = A \exp\left[-\frac{\Delta E_a - E I_E}{k_B T}\right] = k_{OFF_0} \exp\left(\frac{I_E}{k_B T} E\right), \quad (2)$$

where E is the EF strength (*e.g.* in MV m^{-1}) and I_E (C m) quantifies the coupling between the field and the reaction coordinate and has units of dipole (C m) and it is denoted in the literature as $\Delta\mu$[22] or ΔM[352] – change of a dipole moment between the two states (before and after the transition). Expressing the rate in logarithmic form yields a linear relation

$$\ln k_{OFF}(E) = \ln k_{OFF_0} + \frac{I_E}{k_B T} E, \quad (3)$$

which is a convenient form of equation: the slope directly reports on $I_E/(k_B T)$. We further pondered about the physical origin of the interaction term I_E. While the nature of I_E will be conceptually similar across proteins systems (related to charges and dipoles affected by the EF in a particular process), the magnitude I_E will be very much protein and process specific. In the case of our earlier work,[225] both the torque on the kinesin/β-tubulin dipoles and direct electrostatic work on charged residues cooperate to lower ΔE_a, accelerating detachment at high EF strengths. As such, eqn (2) provides a compact quantitative framework for bridging the EF strength and time scales (*via* rate) of a process and is broadly applicable to other molecular and protein systems subjected to an EF. Beyond structural descriptors, many studies now quantify EF effects directly in functional metrics such as binding affinities, catalytic rates, transport fluxes, and assembly/disassembly kinetics, which enables comparisons across systems and modalities. Examples span multi-fold changes in binding constants,[179] strong activity modulation in enzymes,[167] and pronounced acceleration of motor–protein detachment kinetics under intense fields.[225] Reporting calibrated local fields alongside such quantitative functional observables will be essential for translating mechanistic insights into predictive, application-oriented design.

To provide an at-a-glance overview for non-specialists, Table 1 summarizes typical external-field strengths and effective forcing timescales across common modalities in protein–EF research. For pulsed modalities, we distinguish the single-pulse width τ_p from the cumulative "on-time" $\tau_{on} = N\tau_p$ (sum over N pulses); the elapsed experiment time can be much longer due to interpulse gaps.

4.2 Solvent- and ion-mediated contributions: bridging direct and indirect effects

External EFs always act on proteins within a solvent/ion matrix; thus even ostensibly "direct" EF–protein couplings are frequently mediated by the reorganization of hydration water and mobile ions. In bulk water, molecular simulations show that static EFs induce pronounced anisotropy in structure and dynamics (hydrogen-bond kinetics, reorientation and translation),[356] while oscillatory fields can drive non-equilibrium responses that depend on frequency and field amplitude.[357] At sufficiently strong fields, water can also exhibit enhanced proton-transfer/dissociation behavior and nontrivial thermodynamic (including entropic) contributions.[358,359]

These solvent responses feed back on proteins by (i) changing effective dielectric screening and local electrostatic potentials, (ii) modifying hydration-shell friction and thus rotational diffusion and conformational kinetics, (iii) reshaping ion atmospheres and interfacial double-layer dynamics (thereby enabling electroosmotic/ICEO flows), and (iv) providing chemical pathways for electrochemistry-driven ROS/RNS formation in electrode-based geometries. A unified perspective is therefore to treat observed protein responses as a superposition of intramolecular EF coupling and solvent-/interface-mediated contributions, with the relative weight determined by waveform, frequency, conductivity, and boundary conditions. This framework also helps rationalize why similar nominal E can yield different outcomes in simulations (periodic bulk solvent, no electrodes) *versus* experiments (finite cells with interfaces and electrochemical constraints) and it is therefore important to consider such differences when comparing results obtained under seemingly identical conditions.

4.3 Research at higher complexity scales: protein-containing biosystems and biosamples

There are classes of research works that observe the effects of EFs on proteins in complex systems. While the complexity of the systems (cells, tissues, complex food matrices) makes it difficult to assess whether direct or indirect EF effects are in place or the effects were taking place indirectly through other non-protein biomolecular components or indirect EF effects, these works seem to share common effects at the level of proteins so we briefly review them here. In one class of the works, typically from food research and biotechnology,[51,54–57,59–63,241,360–364] often the complex samples containing proteins (mostly enzymes) were exposed to EFs. We excluded these studies from Table 2 in cases when the protein type and content of the protein-containing sample (intact or homogenized fruit, plant, or meat tissue) is undefined or the EF is used also for substantial thermal treatment, hence obscuring the mechanism of EF action. However, the results therein are relevant for research in the food industry and also provide an indication of and inspiration for research on the EF effects on proteins. The techniques employed to explore EF effects on proteins included native PAGE,[365] SDS–PAGE,[366,367] UV absorption spectroscopy,[366,367] intrinsic (Trp or Tyr) fluorescence,[368–371] CD spectroscopy,[371,372] FTIR spectroscopy,[366,373–375] Raman spectroscopy,[376] accessible sulfhydryl group content determination,[176,365–367,371,372,377,378] high-performance size-exclusion chromatography,[372] high-performance liquid chromatography,[365] protein surface hydrophobicity assay,[367–369,377] dynamic light scattering,[176,365,372,378,379] turbidity analysis,[367] transmission electron microscopy,[379] viscosity measurement,[378,379] and enzyme activity assay.[380–383] The results in these studies align with those in Section 2 and Table 2: the EF exerted effects on the conformational change,[366–369,371,375,376,378] protein secondary structure,[366,371–375] partial or complete protein unfolding,[367,370,371,375–377] and affected the enzymatic activity,[382,383] aggregation,[176,365,367,375,378] changed immunoreactivity[371] and rheological properties of the sample.[176,365,377,379]

Another class of works focused on the analysis of (mostly pulsed) EFs on proteins and their structures in cells. In such works, it was not possible to determine whether the effects of the EFs on the protein structures in the cells were direct or indirect (*e.g.*, down-stream effects owing to plasma or internal membrane electroporation and change of intracellular ionic concentration or consequent cell swelling[384]). In these studies, most of the tools used to explore such effects were fluorescence-based microscopy techniques (epifluorescence, confocal), which enabled localization and visualization of the protein structures, such as cytoskeleton fibers. For instance, the effects of pulsed EFs on cytoskeleton structures were explored in several works.[65] It was found that a MT network was disrupted[289,385–388] or more densely packed[389] either immediately or with some delay after electric pulses were applied. A recent study demonstrated the possibility to remodel the MT cytoskeleton in cells without a complete de-polymerization phase.[390] Furthermore, the effects of a PEF were also observed on actin filaments[391] in plant cells and in animal cell cultures.[386,389,392–394] In some studies,[395,396] the finding that the presence of Ca^{2+} in the buffer was required to obtain the EF effect strongly indicated that the EF acted only indirectly on actin filaments through modification of calcium signaling.

These *in vivo* (*i.e.*, in cells) observations of effects of EFs on protein-based structures are biologically and biotechnologically significant, as they enable control of the cell fate with a physical EF handle. Although in most cases they can not provide a mechanistic understanding of the primary target of EF action, they provide inspiration for researchers to generate hypotheses for further *in vitro* research, such as in ref. 397.

4.4 Further outstanding questions for future research

4.4.1 How does protein structure affect the protein's susceptibility to EFs? Empirical evidence directly linking protein structure content to EF susceptibility is still sparse: beyond two atomistic studies,[68,184] there is no systematic mapping across folds. These works tentatively suggest topology-dependent behavior (*e.g.*, comparatively modest perturbations for some α-helical segments under oscillatory EFs *versus* strand orientation-dependent responses in β-sheets), but the limited protein set, simulation timescales, and model conditions preclude general conclusions. Parallels with single-molecule pulling[398] indicate that architecture governs responses to directed perturbations (α-helices "unzip," β-sheets resist *via* shear), hinting that EFs – acting along charge distributions rather than through tensile loading – could produce analogous, structure-specific effects; however, such analogies must be drawn with care given the different coupling mechanisms and timescales. Resolving how protein structure affects EF susceptibility will require coordinated experiments and simulations across diverse folds (including intrinsically disordered regions), with controlled field strengths, orientations and waveforms (static, pulsed, oscillating), and orthogonal structural and functional readouts.

4.4.2 What is the reversibility of the EF effects on proteins? The reversibility of protein structural changes under EFs is only sparsely documented, with most reports scattered across disparate experimental and computational studies. Nonetheless, emerging evidence suggests that reversibility is possible below certain system-specific thresholds of field magnitude, exposure duration, and orientation, while exceeding these limits tends to yield irreversible outcomes.

In early PEF work, ovalbumin exposed to 2.7–3.3 MV m^{-1} exhibited transient activation of sulfhydryl groups and minimal spectroscopic changes, with recovery of the native-like state over minutes to hours,[399] consistent with partial unfolding followed by refolding. In cytoskeletal systems, intense nanosecond pulses at 2 MV m^{-1} modulated tubulin conformation and *in vitro* MT assembly; recovery of repolymerization capacity after cold depolymerization was observed at modest pulse numbers, while high-dose exposures led to incomplete restoration, indicating a graded shift from reversible to irreversible.[21] The recent study by Wang *et al.*[180] on soy protein isolates mapped a critical intensity near 1–1.5 MV m^{-1}, below which depolymerization and aggregation changes reversed within $\sim$30 min, while at $\geq$2 MV m^{-1} reaggregation was stabilized by hydrophobic and disulfide crosslinks.

Table 2 Proteins in EFs: experimental studies meeting the criteria for well-defined EF exposure parameters, isolated protein samples, iso-thermal conditions, and confirmed protein identity. NR = not reported. If EF strength was not reported, we either calculated it from available information, where possible, or we provide another closest related quantity

Protein [reference]	EF strength	Pulse width/ duration	Frequency	Exposure	Techniques used	Effects observed	Temp.
Alcohol dehydrogenase[405]	0, 1.2–2.8 MV m^{-1}	40 μs (bipolar square wave, details NR)	1 kHz	75 (calculated from effective treatment time 0–4.5 ms)	Enzymatic activity assay, FTIR, CD, TRP/TYR fluorescence, UV-absorption, SDS–PAGE	Secondary structure, tertiary structure, enzymatic activity	10–35 °C
α-Amylase[245]	0.3–2.1 MV m^{-1}	2.5–20 μs	1128 Hz	80 pulses	Enzyme activity assay, CD, Trp fluorescence	Enzymatic activity (increased/decreased); structural: secondary structure (increase of α-helices and turns, decrease of β-sheets), tertiary structure (increase in Trp fluorescence)	25 °C
α-Amylase[246]	100 V m^{-1}	Continuous sine wave	1 Hz to 1 MHz	250 s	Enzyme activity assay	Enzymatic activity (increased at lower frequencies)	60 °C
α-Amylase[127]	0.25–1.25 MV m^{-1}	10 μs	1–30 Hz	40 min	Enzyme activity assay, UV-absorption and fluorescence spectroscopy	Enzymatic activity (reduced); structural: conformation change near the tryptophan residues	50 °C
α-Amylase/-pectin complexes[167]	0–2 MV m^{-1}	Bipolar 40 μs pulses	1 kHz	1.02 (2.03) ms	Enzyme activity assay, DLS and zeta-potential, intrinsic fluorescence, FTIR, DSC, confocal light scanning microscopy (CLSM), SEM	Enzymatic activity (decreased); structural: secondary structure (decrease of α-helices and increase of β-sheets), polarity of Trp microenvironment, charge redistribution, and strengthen of protein–polysaccharide association	30 ± 0.5 °C
α-Amylase, lysozyme, lipase, peroxidase, alkaline phosphatase, polyphenol oxidase, glucose oxidase, pepsin[249]	1.3–8.7 MV m^{-1}	2 μs	0.5 Hz	30 and 100 pulses at 2 s pulse period	Enzyme activity assays	Enzymatic activity was reduced either vastly (lipase, glucose oxidase, and heat-stable α-amylase), moderately (peroxidase and polyphenol oxidase), or slightly (alkaline phosphatase), lysozyme and pepsin showed diverse activity patterns under certain voltages	20 °C
β-Lactoglobulin[406]	1.25 MV m^{-1}	2 ms	0.07 Hz	1–10 pulses	DSC, SDS–PAGE, TEM, sol–gel transition assay	Thermal stability was greatly reduced; the gelation rate was enhanced; structural: denaturation, aggregation	4–35 °C
β-Lactoglobulin[407]	800 W	Continuous irradiation	2.45 GHz	5 s	Polarimeter	Enhanced kinetics of the folding and denaturation processes	4–44 °C
β-Lactoglobulin[252]	Up to 4×10^5 kW	10 μs	1 Hz	1 and 10 min (30 and 300 pulses)	OPA assay, determination of the kinetic parameters, CD	The tryptic and chymotryptic hydrolysis was significantly improved, the catalytic efficiency was improved; structural: electrical pretreatments induced changes in the 3D structure of the protein bringing it to a transient or a pseudo-unfolded state	37 and 85 °C
β-Lactoglobulin[178]	0–1 kV m^{-1}	NR	50 Hz–1 MHz	NR	CD, Trp fluorescence, ANS fluorescence, quenching analysis-retinol	Secondary structure (increase of random coil fraction, decrease of β-sheets); tertiary structure: (unfolding - Trp fluorescence was increased at 90 °C and decreased at 70 °C, higher affinity of hydrophobic compounds when exposed to higher temperatures); higher affinity for retinol (especially at lower frequencies)	20–95 °C
Actin[236]	0.46 THz radiation with an energy dose of 5.7 mJ cm^{-2}	10 ms	1 Hz	1200 pulses (20 min duration of experiment)	Polymerization assay, fluorescence microscopy	Activation of the elongation phase of actin polymerization	25 °C
Alkaline phosphatase (AP), antidinitrophenyl (anti-DNP) with its antigen[164]	0.08 W m^{-2}	Continuous irradiation	100 GHz	1–2 h	Enzyme activity and kinetics assay	AP: irradiation may lead to other structural alterations of the enzyme that impose conformational changes affecting the turnover of the enzyme, thereby reducing the number of active enzyme molecules in the solution, anti-DNP: no effects	25 °C

Table 2 (*continued*)

Protein [reference]	EF strength	Pulse width/ duration	Frequency	Exposure	Techniques used	Effects observed	Temp.
Amyloid-β (Aβ)[177]	0.73 mW mm^{-2} [E = 2340 V m^{-1}]	2 ms	Repetition rate 100 kHz (34.88 THz)	NR	ThT fluorescence binding assay, FTIR	The aggregation speed ratio decreased to approximately 80%; the THz wave at 34.88 THz significantly slowed down the fibrotic progression; secondary structure (the structure of the β-sheets was transforming to a looser structure with more coil and bend regions)	37 °C
Amyloidogenic fragment (1–27) and non-amyloidogenic fragment[408]	177 V m^{-1} (calculated from spatial dose 150 mJ cm^{-2} and duty cycle)	1 ms	5 Hz	Up to 30 min	Scanning electron microscopy, thioflavin T fluorescence, polarized light microscopy (congo-red staining), synchrotron-radiation IR micro-spectroscopy	Fibril aggregation of the peptides, increased formation of β-sheets. The effect present in amyloidogenic sequence, not in non-amyloidogenic ones. Equivalent heating did not cause fibril formation	27–30 °C
Citrate synthase-α-crystallin[409]	1.443 kV m^{-1} (calculated from average SAR 4.85 kW kg^{-1}, assuming water as the material)	10, 15, and 20 s	2.45 GHz	Continuous irradiation (as a characterized artifact the MW EF peaked by 3–8-fold above the average amplitude each 50 Hz)	Surface plasmon resonance	Unfolding occurred at significantly lower temperatures	25 °C, 29.5–44 °C
BSA[179]	0, 1, 1.5, 2, 2.5 and 3 MV m^{-1}	40 μs	1 kHz	0.34–1.02 ms	Fluorescence spectroscopy (fluorescence quenching, intrinsic fluorescence), CD, zeta potential, UV-absorption, ANS fluorescence, Ellman's assay, BSA/PBSA-curcumin binding affinity assays	Moderate PEF treatment induces the partial unfolding of BSA, exposing more hydrophobic cavities, thereby facilitating the non-covalent binding of curcumin to the protein (surface SH content was increased as well); however rigorous PEF treatment conditions caused BSA aggregation and weakened the binding ability of BSA to curcumin (increase of intermolecular disulphide interactions, excessive exposure of hydrophobic groups – hydrophobic collapse); secondary structure (decrease of α-helix structures, increase of β-sheet, β-coil and random coil content)	≤30 °C
BSA[240]	0, 0.5, 1 and 1.5 MV m^{-1}	20 μs	1000 Hz	15, 20, 25, 30, 35, 40 and 45 min	SDS–PAGE, CD, attenuated total reflectance-FTIR, intrinsic fluorescence spectroscopy, UV-absorption, ANS fluorescence, Ellman's assay, DLS and zeta potential	The polarization effect of the PEF enhanced the emulsifying properties of BSA–glucose conjugates by accelerating the glycation reaction, while the ionization effect significantly suppressed the browning; secondary structure (decrease of α-helix content, increase of β-sheet, β-coil and random coil content); tertiary structure: unfolding	90 °C
BSA[241]	0.35, 0.45, 0.57, 0.81 MV m^{-1}	50 μs	NR	10 pulses	DLS, CLSM, ANS fluorescence, DSC, intrinsic fluorescence spectroscopy	At lower electric field strengths (0.35–0.57 MV m^{-1}), PEF treatment improved the browning intensity, the protein solubility and the grafting degree, and reduced the particle sizes, the fluorescence intensity and surface hydrophobicity of BSA/starch conjugates. At a higher EF strength (>0.57 MV m^{-1}), BSA/starch conjugates exhibited decreased protein solubility, grafting degree, and particle size increase	22.5–25.8 °C

Table 2 (*continued*)

Protein [reference]	EF strength	Pulse width/ duration	Frequency	Exposure	Techniques used	Effects observed	Temp.
BSA and bovine insulin[410]	15–20 mW kg^{-1}, 0.5 W	—	1.0 GHz	3 to 48 h	Light scattering measurements, TEM, thioflavin T (ThT) assay	BSA: aggregate formation; bovine insulin: amyloid fibril formation	BSA: 25 to 45 °C, bovine insulin: 60 °C
BSA, MTs[293]	156 V m^{-1} (from 6.5 mW cm^{-2} beam power density)	CW	500 GHz radiation	0.4 s irradiation time	SAXS	No structural changes	NR
BSA, MTs[293]	1.8 MV m^{-1}	600 fs	100 MHz pulse repetition rate, effective irradiation spectrum 0.1 to 6.0 THz	0.2–0.4 s	SAXS	No structural changes	NR, temperature rise due irradiation <0.12 °C
BSA lyophilized[239]	5–20 mW (only laser power value was provided)	NR	3.6 THz	60 min irradiation time	CD, UV-absorption, Trp fluorescence	Conformational changes – secondary structure (changes in the intensities of characteristic bands in UV absorption and CD spectra); modification of its functional characteristics – ligand binding parameters; as a ligand is added to the treated protein solution, fluorescence quenching is observed	NR
BSA, lysozyme[165]	78, 150, 300 and 500 V m^{-1}	NR	10 and 500 Hz	3 h.	CD, intrinsic (Trp) fluorescence	The tertiary structure of both lysozyme and BSA was affected, the secondary structure was perturbed in lysozyme (decrease of α-helices and increase of β-sheets); the electric force applied during EF exposure was significant to perturbing hydrogen bonds stabilizing the native structure of both proteins	22.7 °C to 24.2 °C
Carboxypeptidase-G2 (CPG2)[243]	1 MV m^{-1}	8, 16, 24 ns	10 Hz	20, 40, 60, 90, 120, 180 or 240 s	Enzyme activity assay, SEC, reverse phase-HPLC, SDS–PAGE, MS and CD, inductively coupled plasma-MS	Enzymatic activity (decreased)	NR
Cytochrome *c*, myoglobin, trypsin[411]	28–130 V m^{-1}	Static field	Static field	~90 min	Intrinsic fluorescence spectroscopy, attenuated total reflection infrared (ATR-IR), UV-VIS absorbtion, ThT fluorescence, CD, SEM	Secondary – (both the α-helix and β-sheet content decreased) and tertiary structure unfolding; amorphous aggregation	25 °C
Apoazurin[286,288]	1–10 MV m^{-1}	Static field	—	—	Intrinsic (TRP) fluorescence spectroscopy	Change (decrease) of fluorescence intensity, however no conformational change in the protein	20 °C
Ovomucin-depleted egg white[228]	70–170 kV m^{-1}	20 μs	300 Hz	NR	SDS–PAGE, turbidimetry	Aggregation	Below 50 °C
Elastin[173]	12 and 20 kV m^{-1}	Continuous exposure	Continuous exposure	More than 5 days	DLS and zeta-potential, field emission-SEM, FTIR and photoluminescence (PL) spectroscopy	Conformational changes in the secondary structure (increase of α-helices and decrease of β-sheets and turns); unfolding, denaturation and the size of the aggregates were reduced	RT
(Enhanced) green fluorescent protein (EGFP)[284]	250 mW	Continuous microwave irradiation (100 ps)	9.5 GHz	~4.5 min	Fluorescence emission anisotropy	Microwave irradiation affects polarization of the EGFP fluorescence	9.7–12.5 K
Ferritin[141]	1, 2, 3 or 4 MV m^{-1}	—	2000 Hz	—	Fluorescence spectroscopy, CD, intrinsic fluorescence spectroscopy, Raman	Secondary structure: as the EF intensity increased, the α-helix content showed a trend of first decreasing and then increasing, and the	RT

Table 2 (*continued*)

Protein [reference]	EF strength	Pulse width/ duration	Frequency	Exposure	Techniques used	Effects observed	Temp.
					spectroscopy, cold field emission-SEM, TEM	β-sheet content trend was the opposite; tertiary structure: partial unfolding, decrease in the stability; reversible self-assembly; aggregation (the solubility of ferritin decreased with increasing exposure of hydrophobic groups – breakage of hydrogen bonds and the transformation of SS bridges)	
Green fluorescent protein (GFPuv5)[283]	50 and 70 MV m^{-1}	∼60 ps	40 Hz	30 ms	Electric field modulation spectroscopy	Field-induced quenching of the fluorescence was observed, changes in the fluorescence decay profile – decrease in the fluorescence lifetime	RT
Horseradish peroxidase (HRP)[242]	0.5–2.5 MV m^{-1}	1.5 μs	10 Hz	207–1242 pulses	Enzyme activity assay, CD, intrinsic fluorescence spectroscopy	Enzymatic activity (decreased); secondary structure (decrease of α-helix content); tertiary structure (intrinsic fluorescence intensity increased)	Below 40 °C
HSA fibrils[227]	0–23 MV m^{-1}	Static field	—	10 min	ThT fluorescence, CD, FTIR spectroscopy, TEM, fluorescence microscopy	Secondary structure (decrease of β-sheet content), the initial propagation of the fibrils was followed by the disintegration of the fibrillar network into smaller aggregates	RT
HSA fibrils[235]	∼8 MV m^{-1}	Continuous exposure	5 to 100 Hz	1–6 min	ThT fluorescence, CD, turbidimetry, DLS, FTIR spectroscopy, fluorescence microscopy, high resolution-TEM	An initial fibrillar growth was followed by the destruction of amyloid fibrils into smaller aggregates; secondary structure (reduction of β-sheets, increase of α-helix, β-turns and random structure content)	25 ± 0.5 °C
Luciferase[412]	∼0.75 MV m^{-1}	—	100 kHz continuous sine wave	EF 5 × 100 s ON and OFF, for signal integration	Enzymatic assay, spectrometer	Decreased luciferase activity	22 °C
WT/A4V SOD1[413]	25 kV m^{-1}	—	DC (*via* saltbridge, 14–18 μA)	2–30 min	Electrophoresis, UV-VIS spectroscopy	A4V Zn4-SOD1 monomerized and partially unfolded	15 °C cooling of the capillary
Lysozyme[414]	3.5 MV m^{-1}	Bipolar square: positive 2 μs, 20 μs gap, negative 2 μs	—	300, 600, 900, 1200 μs	Activity assay, CD, micro-Raman spectroscopy	Activity of lysozyme decreased, changes in the secondary (loss of α-helices increase of β sheets and random coil) and tertiary structure (transition of S–S conformation)	Max 20 °C
Lysozyme[415]	3.5 MV m^{-1}	Bipolar: positive 2 μs, 15 μs gap, negative 2 μs	1 kHz	Total exposure 300, 600, 900, 1200 μs	Lysozyme activity assay, aggregation analysis, sulfhydryl groups analysis, surface hydrophobicity analysis, fluorescence analysis, circular dichroism	Activity of lysozyme decreased-irreversible, aggregation effect only for 1200 μs exposure, increasing number of accessible sulfhydryl groups (cleavage of the disulfide bonds), hydrophobicity increased with subsequently hydrophobic collapse for longer EF exposure than 600 μs, increasing intensity in fluorescence spectra and red shifts after EF (changes in tertiary structure), changes in secondary structure (loss of α-helices)	Below 60 °C
Lysozyme[416]	3.5 MV m^{-1}	2 μs	1000 Hz	Total exposure 300, 600, 900, 1200 μs	Activity assay, ANS-binding fluorescence, intrinsic fluorescence spectra, CD	Decreasing activity of lysozyme, hydrophobicity increased with subsequently hydrophobic collapse for longer EF exposure 1200 μs, increases of fluorescent emission intensity and red shifts, changes in tertiary structures according to near-UV CD analysis, conformational changes in secondary structure (loss of α-helices)	≤60 °C

Table 2 (*continued*)

Protein [reference]	EF strength	Pulse width/ duration	Frequency	Exposure	Techniques used	Effects observed	Temp.
Lysozyme (crystal)[417]	62 or 78 mW cm^{-2} (483 or 542 V m^{-1})	25 ms	0.4 THz	Effect studied expected within a single pulse	Structural analysis, X-ray crystallography	Electron density changes – consistent with a subtle longitudinal compression of the α-helix	Lower than 25 °C
Lysozyme[24]	0.15 kV m^{-1}	0.8 μs pulse filled 0.1 THz pulses	10 kHz	10 min	Microwave dielectric relaxation spectroscopy, NMR	Decrease of the dielectric permittivity, irradiation probably enhanced protein hydration – water with reduced mobility and more H-bonds,	25 °C
Hen egg-white lysozyme (HEWL)[418]	0, 1–2 MV m^{-1} (1 MV m^{-1} for H_2O hydration; 2 MV m^{-1} for D_2O hydration)	Static, N.A.	—	Continuous during QENS (quasi-elastic neutron scattering) acquisition (duration NR)	Incoherent QENS (BASIS; $\Delta E \approx 3.5$ μeV; $Q = 0.3$–1.1 $Å^{-1}$)	No measurable change in protein dynamics (up to 2 MV m^{-1}) or hydration-water relaxation times (1 MV m^{-1}); authors suggest threshold $E_c \sim$ 2–3 MV m^{-1} (breakdown-limited)	210–270 K
Lysozyme from egg white, albumin from bovine serum and urease from jack beans[419]	10, 15, 20, 25, 30 MV m^{-1}	5 ns	3 Hz	500 pulses	SDS–PAGE, native–PAGE, enzyme activity assay	Lysozyme and albumin without effect, urease: trimer and dimer shifted downward from 250 kV cm^{-1} in SDS–PAGE (quaternary and tertiary structure disruption), decreased enzymatic activity from 250 kV cm^{-1}	NR, max. rise 3 °C
Multi-protein system (lysozyme, ovalbumin, ovotransferrin)[420]	2.5 MV m^{-1}	2 μs	100 Hz	200, 400, 600, 800 μs	Chromatography, SDS–PAGE, turbidimetry	Turbidity measurement and SDS–PAGE shows that lysozyme could be the reason for aggregation in the multiprotein system during the PEF exposure due to electrostatic interactions and disulfide bonds, chromatography does not indicate aggregates inside samples	≤18 °C
Multi-protein system (diluted egg white)[421]	2.5 MV m^{-1}	2 μs	100 Hz	200, 400, 600, 800 μs	Soluble protein content determination, particle size distribution, and *Z*-average size measurement, zeta potential, protein carbonyl content measurement, free accessible sulfhydryl content determination, electrophoresis (native/ SDS–PAGE)	Soluble protein content decrease, *Z*-average particle size increases after 400 μm, creating aggregates, no increase in protein carbonyl content, slight increase in free sulfhydryl content creating aggregates, no increase in protein carbonyl content, a slight increase in free sulfhydryl content, electrophoresis showed that lysozyme was prone to precipitation with other protein components (ovalbumin, ovotransferrin)	≤18 °C
Lysozyme, pepsin[422]	3.5 MV m^{-1}	Bipolar: positive 2 μs, negative 2 μs, gap 20 μs	NR	100–1200 μs (lys.)/600 μs (pep.)	CD, enzymatic activity assay, sorbitol effect	Disruption of secondary structure (far-UV CD): lysozyme loss of α-helical structure and pepsin loss of β-sheet structure, unfolded tertiary structure (near-UV CD), sorbitol has a structural protective effect on both proteins against the PEF, enzymatic activity decreasing with a longer exposure to the PEF	≤45 °C
MTs[25]	40.9 MV m^{-1}	1 ps	Broad 1 THz spectrum (due to 1 ps pulse width), 1~kHz pulse repetition rate	Up to 11 min exposure (*i.e.* N = 660 000 pulses)	Light and fluorescence microscopy	MTs disassembly	RT
MTs[25]	10 MV m^{-1}	2.9 ps	1.5 THz, pulse 1 kHz firing frequency	Up to 11 min exposure (*i.e.* N = 660 000 pulses)	Light and fluorescence microscopy	MTs disassembly	RT
MTs[25]	3.7 MV m^{-1}	6.3 ps	0.5 THz, pulse 1 kHz firing frequency	Up to 11 min exposure (*i.e.* N = 660 000 pulses)	Light and fluorescence microscopy	MTs disassembly	RT

Table 2 (*continued*)

Protein [reference]	EF strength	Pulse width/ duration	Frequency	Exposure	Techniques used	Effects observed	Temp.
MTs[423]	0.6–2 kV m^{-1}	Continuous harmonic wave	3.5, 20, 29 GHz	200 s exposure time	Turbidimetry assay of MT polymerization kinetics	—	32–39 °C
Tubulin during polymerization[424]	2.5 V m^{-1}	2 ms	10 Hz	10 min during polymerization	Negative stain electron microscopy	Formation of parallel oriented arrays of MTs in the direction of the field	37 °C
MTs[425]	<50–190 kV m^{-1}	NR	10 kHz–MHz (sinus)	NR	Dark field microscopy	Parallel arrays of MTs are formed due to the dipole moment induced along the long axis of the MTs	25–28 °C
Ovalbumin (OVA), BSA, OVA + BSA[426]	2, 2.5, 3 and 3.5 MV m^{-1}	2 μs	200 Hz	400 μs	High-performance size exclusion chromatography, native/ SDS–PAGE, sulfhydryl groups analysis	Protein aggregation of OVA caused by decreasing sulphydryl groups (≤2.5 MV m^{-1}); no aggregation effect of BSA probably because of fewer sulfhydryl groups; aggregation effect of OVA + BSA caused by disulfide bond between proteins (≤2.5 MV m^{-1})	≤30 °C
Ovalbumin + divalent metal ions (Ca^{2+}, Cu^{2+}, Ba^{2+})[427]	0 to 5 MV m^{-1}	40 μs	1 kHz	565, 1130, 1695, 2260 μs	Raman spectroscopy, FTIR, fluorescence spectroscopy, surface tension, surface hydrophobicity,	Surface hydrophobicity and surface tension showed an enhanced trend at first and then reduced with pulse time. The spectra showed at the beginning of the pulse treatment, some hydrophobic amino acid side chains tended to be exposed. As PEF processing continued, ovalbumin's side chain groups were more inclined to be more intermolecular. Different metal ion types and pulse treatment times modified the protein structure of ovalbumin.	4 °C
Ovalbumin ± Ca^{2+} (ref. 161)	0 to 5 MV m^{-1}	15 μs	1 kHz	720 to 4320 μs	CD, TEM	PEF's linearly unfolding of secondary structure with increasing pulse intensity or treatment time (loss α-helix and decrease β-sheets) and perturbation on the tertiary structure was more significant than that on the secondary structure. the synergetic effect PEF + Ca^{2+} increases the effect of unfolding of the secondary structure + creating nanotubes followed by an aggregation effect with increasing conductivity.	20 to 45 °C
Ovalbumin/egg white[399]	2.7–3.3 MV m^{-1}	0.3 or 0.9 μs	1.1 Hz	50–400 pulses (exponential decay)	Free sulfhydryl group content analysis by DTNB, UV-spectroscopy, gelation effect of egg white	Probably reversible partial protein unfolding, not caused any visible aggregation, without changes in gelation properties of egg white	<29 °C
Ovomucoid (IgG1 and IgE antibodies)[428]	1, 2, 3 or 4 MV m^{-1}	NR (similar works from the related groups use 2̃ μs)	2000 Hz	Flow rate 3.2 mL min^{-1} (neither the chamber volume nor the residence time is provided)	SDS–PAGE, SEM, contact angle assay, CD, FTIR spectroscopy	PEF reduced the binding ability of IgG1 and IgE in OVM, no changes in primary structure, changes in secondary structure – α-helix and β-sheets decrease, PEF treatment induced the expansion of protein molecules, and increased intermolecular forces in solution, surface hydrophobicity increased, total accessible -SH content increased, SEM showed changes in microstructure of OVM (rod-shaped and spherical shape was transformed into irregular flake structure structures under the influence of the PEF)	25 °C
Pea protein isolate[126]	0, 0.5–2.5 MV m^{-1}	40 μs (monopolar square wave)	1 kHz	20 (calculated from effective treatment time 0.8 ms)	Surface hydrophobicity analysis, CD, intrinsic fluorescence spectroscopy, UV-absorption, antioxidant activity analysis	Secondary structure, tertiary structure, unfolding, increased antioxidant capacity	<30 °C

Table 2 (*continued*)

Protein [reference]	EF strength	Pulse width/ duration	Frequency	Exposure	Techniques used	Effects observed	Temp.
Papain[247]	2–5 MV m^{-1}	4 μs	1.5 kHz	200 or 500 pulses, total time 0.8 or 2 ms	Far UV CD, determination of papain activity and free cysteine content, reducing agent prevents oxidation	Significant reduction of activity after 24 hours, decrease of free cysteine content after 24 hours, no change of pH after PEF exposure, major inactivation effect of papain was related to the conformational change of the α-helix, irreversibly inactivated	10 °C
Papain[429]	1 and 1.3 MV m^{-1}	NR	0.2 Hz	48–432 pulses, (flow rate 0.2, 0.4, 6.6 L min^{-1}, chamber volume 0.13 mL estimated from electrodes dimensions)	Residual activity, relative protein concentration, sulfhydryl group content, fluorescence spectrophotometer	Enzymatic activity reduction, RPC and SH content decrease with the number of pulses for 0.2 and 0.4 L min^{-1} means secondary changes in structure, no significant changes in the ANS fluorescence – same surface hydrophobicity, higher peaks of fluorescence intensity for PEF means tertiary changes in structure, no emission shifts in wavelength	20 °C (max 50 °C measured)
Pectinase[430]	0.3–2.1 MV m^{-1} (square monopolar pulses)	5–20 μs	1–10 kHz	80 pulses, 50–160 mL min^{-1} (chamber volume NR)	Enzyme kinetics, far UV CD, fluorescence spectroscopy, SDS–PAGE	Pectinase activity increased with field strength (maximum at 12 kV cm^{-1}) and flow rate (maximum 80 mL min^{-1}), the PEF did not modify the polypeptide chain composition according to SDS–PAGE, in the secondary structure of the PEF sample α-helix and β-sheets increased and random coil content decreased, an increasing number of Trp residues on the surface of the pectinase molecules shows changes in the tertiary structure, the PEF increased the thermal stability of pectinase	RT
Horseradish peroxidase (POD), polyphenol oxidase (PPO)[431]	0.5–2.5 MV m^{-1}	POD: 1.4 and PPO: 0.6 μs	10 Hz	POD: 290–1740 μs, PPO: 124–744 μs	Enzyme activity assay, CD	Enzymatic activity (decreased); secondary structure (decrease of α-helix content)	≤40 °C
Pepsin[162]	1.78–3.56 MV m^{-1}	Bipolar square pulses: 2 μs positive, 18 μs gap, 2 μs negative	800 Hz	Total treatment time 126–630 μs, *i.e.*, N = 63–315 pulses	Enzymatic activity, UV absorption, CD, solubility analysis	Enzymatic activity deactivation, secondary structure loss, aggregation	<52 °C, pepsin claimed to be stable <60 °C,
Horseradish peroxidase, β-galactosidase, lactate dehydrogenase (LDH), glucoamylase, enolase, invertase[432]	0.4–2.3 MV m^{-1}	2 μs	50 Hz	30 or 60 s	Enzyme activity assay, SDS–PAGE	Enzymatic activity (increased with lower and decreased with higher EF strength); the degree of the influence by PEF treatment seemed to be greatly different depending on the type of enzyme; refolding enhancement of the thermal denatured peroxidase	NR
The second PDZ domain of the human E3 ubiquitin ligase LNX2 (*LNX2*)^{PDZ2} (ref. 22)	∼50–100 MV m^{-1}	50–500 ns	– (effects observed within a single pulse)	—	X-ray crystallography	The symmetry of the protein crystal was reduced; perturbations of nearly every type of physical interaction throughout the protein structure—induction of side-chain rotamer flips, continuous displacement of backbone atoms, side chains and bound waters, propagated rotamer shifts suggesting collective motions through the structure, breaking and re-forming of hydrogen bonds, global motions of entire secondary structure elements, and complex coordinated changes in large regions	RT
Plasmin (fibrinolysis)[248]	0, 1.5–4.5 MV m^{-1}	2 μs	0.1 Hz	10–50 pulses	Enzymatic activity assay	Enzymatic activity (decreased)	10–15 °C

Table 2 (*continued*)

Protein [reference]	EF strength	Pulse width/ duration	Frequency	Exposure	Techniques used	Effects observed	Temp.
Polyphenol oxidase (PPO)[433]	1.8 MV m^{-1}/ 0.9 MV m^{-1}	—	AC voltage, capacitively coupled: 10 Hz to 760 kHz	0–6 min	Enzyme activity assay	Frequency-dependent inhibition or stimulation of PPO enzyme activity	NR, remained constant
Protamex (bacillolysin and subtilisin)[251]	1.4 and 1.82 MV m^{-1}	20 μs	10 Hz	0–900 pulses	Enzymatic activity assay	Inactivation of the enzyme	18 to 55 °C
Protease (from *Pseudomonas fluorescens*)[434]	0.62 MV m^{-1}	700 μs	0.1 Hz	0, 10 and 20 pulses	Enzymatic activity assay	Inhibition of the enzymatic activity	15 to 20 °C
S-Adenosylhomocysteine (AdoHcy), 5′-methylthiadenosine (MTA)[250]	325–583 V m^{-1} (calculated from 1.5–3.1 W g^{-1}, assuming water as the material)	—	10.4 GHz continuous irradiation	0–90 min	Enzymatic activity assays, CD spectroscopy	Irreversible time-and temperature -dependent inactivation of both enzymes	70 to 90 °C (below the denaturation temperature of the given enzymes)
Soy protein isolate[180]	0.5–3 MV m^{-1}	Pulse pair: 40 μs, 40 μs 200 gap, μs opposite polarity	1 kHz	51 (calculated from flow, volumes, total treatment time)	Turbidimetry, DLS, SDS–PAGE, size exclusion chromatography, carbonyl content (DNPH), sulfhydryl content (DTNB), surface hydrobhobicity (ANS), CD, Trp/Tyr fluorescence	Secondary structure, tertiary structure, protein–protein interaction, aggregation	20 to 30 °C
Spike protein of SARS-CoV-2[290]	<5 kV m^{-1} (estimated based on 700 W and geometry of the waveguide)	—	2.45 GHz microwave	2, 5 and 10 min	UV-Spectroscopy	Significant denaturation can be induced by microwave irradiation	37 °C
Sup35NM (prion)[238]	1, 2 MV m^{-1}	50, 1000 μs	NR	10 pulses	AFM	Significant reductions in the length of prion fibrils, full disintegration of fibrils	RT (NR) + rise <4.6 °C
Transthyretin aggregates[226]	126 MV m^{-1}	1 ns	1.7 Hz	0, 200–1000 pulses	Native/SDS–PAGE, BCA method, fluorescence microscopy	Protein aggregates disassembly	18 °C
Tropomyosin[134]	0.5–2 MV m^{-1}	10 μs	50 Hz	Up to 4500 pulses (calculated from flow, volumes, total treatment time)	DLS, CD, PAGE, FTIR, Trp/Tyr fluorescence, carbonyl content (DNPH), surface hydrobhobicity (ANS)	Secondary structure, tertiary structure, interactions (depolymerization (from dimers), antibody binding)	NR/ice water bath
Tubulin[21]	2 MV m^{-1}	11 ns	1 Hz	0–800 pulses	Intrinsic (Trp, Tyr) fluorescence, dynamic light scattering, zeta potential, atomic force microscopy, 2D-PAGE and immunoblotting	Protein conformation, hydrodynamic radius, effective charge, capability of self-assembly	4 °C and slightly above
Tubulin, MTs[80]	100 to 400 kV m^{-1}	25 to 300 μs	1	Effects are observed within $N = 1$ pulse	Electric birefringence method	Tubulin and MT orientation, affected by MT-associated proteins	10 °C
Ubiquitin (Ub)[163]	18 and 90 mW cm^{-2} ($E = 260$, 582 V m^{-1})	0.8 μs	95 GHz radiation, 10 kHz pulse firing rate	0–12 min total exposure, *i.e.* 5.76 s net exposure	NMR	Change of rate of hydrogen–deuterium exchange of the protein amides (accelerated in the protein interior and in hydrophobic surfaces while decelerated in the surface loop and short 3_{10} helix regions)	25 °C
Whey protein isolate[355]	1.5 and 3 MV m^{-1}	25 μs	1.04 kHz	7.35 ms ($N = 294$ pulses)	SDS–PAGE, far-UV CD spectroscopy, measurement of free amino groups (*o*-pthalaldehyde (OPA) method)	EF promoted glycosylation of protein → decreased content of secondary structure and free amino groups, increase of glycosylation and emulsion stability	30 ± 0.5 °C

Table 3 Effects of EF on proteins observed in MD simulations. R_g = radius of gyration, SS = secondary structure, E = static electric field, EM = oscillating electromagnetic field

System of study [reference]	Type, shape of field	Field strength	Force field and water type (where available)	Condition of simulation	Simulation length	Observable
Act d 2 kiwi fruit allergen[435]	*E*, oscillating (2450 MHz)	50 MV m^{-1}	CHARMM27, TIP3P	NPT (300, 325, 350, 375 K, Berendson, Parrinello–Rahman)	2 ns	SS, RMSD, RMSF, SASA
Alanine polypeptide[185]	*E*, static	50–1000 MV m^{-1}	OPLS/AA, no water	NA	400 ns	SS, entropy, enthalpy
Alcalase[244]	*E*, static	1 MV m^{-1}	CHARMM36	NA	200 ns	RMSD, H-bond, SASA, R_g
Amyloid-β peptide[151]	*E*, static	20 MV m^{-1}	Amber ff99SB-ILDN, TIP3P	NPT (310 K, V-rescale, Parrinello–Rahman)	200 ns	SS
Amyloid-β peptide[147]	*E*, static	200–500 MV m^{-1}	Amber ff99SB-ILDN, TIP3P	NPT (300 K, V-rescale, Parrinello–Rahman)	100 ns	Dipole moment
Amyloid-β peptide[174]	*E*, oscillating (1 GHz)	10, 100, 200 MV m^{-1}	NVT (300 K)	CHARMM36m	300 ns	RMSD, RMSF, H-bond, SS, free energy
Amyloid-β peptide[133]	*E*, static, oscillating (0.1–1 GHz)	175, 200 MV m^{-1}	ff14SB, TIP3P	NVT(300 K, Monte Carlo)	100 ns	Interpeptide distance, R_g, dispersion entropy, dipole moment, potential of mean force
Amyloid-β (1BA4) peptide[214]	*E*, static	100, 250, 500, 1000 MV m^{-1}	CHARMM, TIP3P	NPT	10 ns	RMSD, dipole moment, SS, R_g
Amyloid-β peptide[175]	*E*, static, oscillating (0.1, 1 GHZ)	100, 200 MV m^{-1},	ff14SB, TIP3P	NVT (300 K, Langevin thermostat, Berendsen barostat)	500 to 1200 ns	RMSD, H-bonds, dipole moment, SS
apoC-II peptide[436]	*E*, EM, static, oscillating (1, 2.5 and 5 GHz)	0.7 to 700 MV m^{-1}	GROMOS96-43a1, SPC	NPT (300 K, Berendson)	200 ns	R_g, N–C termini distance, dipole moment, radial distribution functions (rdf), H-bond(s)
apoC-II peptide[153]	*E*, EM, static	7 kV m^{-1} to 700 MV m^{-1}	GROMOS96-43a1, SPC	NPT (300 K, Berendson)	4.8 μs	RMSD, dipole moment, free energy map, R_g, amino acids conformations
Ara h 6 peanut protein[155]	*E*, static, oscillating (2450 MHz)	50 MV m^{-1}	CHARMM27, TIP3P	NPT (Berendsen, 300, 380, 425 K)	1 ns	RMSD, R_g, dipole moment, SASA, SS
Aquaglyceroporin-7[437]	*E*, static, oscillating (10 GHz)	0.2 MV m^{-1}	CHARMM36, SPC/E	NPT (300 K, Nosé–Hoover, Parrinello–Rahman)	71 ns	RMSD, RMSF, R_g, free energy, H-bonds, water permeation
Human aquaporin 4[188]	*E*, static, oscillating (2.45, 20, 50, 100, 200, 500 GHz)	65 MV m^{-1} to 25 GV m^{-1}	CHARMM27, TIP3P	NPT (298 K, Nosé–Hoover, Langevin dynamics)	9 μs	Open and closed states of selectivity filter, dipole, potential-of-mean-force profile
Bovine insulin (2A3G)[157]	*E*, static	150–600 MV m^{-1}	Amber ff03, TIP3P	NPT (Berendsen, Parrinello–Rahman)	1 μs	Dipole moment, SS, H-bonds
BSA, trypsin[158]	*E*, static	0.03–10 000 MV m^{-1}	Amber all-atom, TIP3P	NA	NA	RMSD
BSA[240]	*E*, static	1.2 MV m^{-1}	OPLS-AA, TIP3P	NPT	30 ns	SASA, SS
Carnosine[191]	EM, oscillating (2.45 GHz)	10^{-6}–10^{2} V m^{-1}	OPLS-AA	NVT (velocity rescaling)	20 ns	Electrostatic potential surface, dipole moment, molecular collision number, kinetic energy of collision
β-Casein (BCN)[160]	*E*, sinusoidal	4–4000 MV m^{-1}	CHARMM36, TIP3P	NPT (300 K, Berendsen, Parrinello–Rahman)	10 ns	RMSD, RMSF, R_g, dipole moment, SS, distance matrix for residue pairs, SASA
Cav2.1 channel[183]	*E*, oscillating (40.12, 42.5, 42.65, 42.83, 46.63, 48.5 THz)	600 MV m^{-1}	CHARMM36, POPC, TIP3P	NPT (315 K, Nosé–Hoover, Parrinello–Rahman)	3 ns	Free energy profile, H-bonds, vibrational spectra
Chignolin (1UAO)[438]	*E*, static	100, 250, 500 and 1000 MV m^{-1}	CHARMM27 and TIP3P	NPT (300 K, Berendsen thermostat)	10 ns	RMSD, dipole moment, SS, R_g
Chignolin[439]	*E*, static, oscillating (9–3600 ps period, *i.e.* 111 GHz–278 MHz)	1000 MV m^{-1}	CHARMM27, TIP3P	NPT (300 K, Berendsen)	10 ns	RMSD, SS, dipole moment
Chignolin[181]	*E*, static, oscillating (2.45 GHz)	200 MV m^{-1}	Amber ff99SB, TIP4P/2005	NPT (300 K, Berendsen, Parrinello–Rahman)	5 μs	RMSD, SASA, free energy, H-bond(s), Ramachandran plot analysis
Connexin 26 hemi-channel (2ZW3)[152]	*E*, static, oscillating (2.4 and 50 GHz)	100, 175, 250, 325, 400 MV m^{-1}	CHARMM 36, TIP3	NPT (310 K, Nosé Hoover, Parrinello–Rahman)	50 ns	RMSD, dipole moment, H-bonds, tertiary structure
Cytochrome *c*[154]	*E*, static	500–2000 MV m^{-1}	CHARMM, TIP3P	NVT (310 K, Berendesen)	40 ns	

Table 3 (*continued*)

System of study [reference]	Type, shape of field	Field strength	Force field and water type (where available)	Condition of simulation	Simulation length	Observable
						Protein–surface distance, protein orientation, radial distribution function, protein–surface interaction energy, RMSD
Dihydro-lipoamide dehydrogenase (1BBL)[149]	*E*, static	200–800 MV m^{-1}	CHARMM27, TIP3P	NPT (310 K)	30 ns	RMSD, dipole moment, SS, R_g, H-bonds
Diphenyl-alanine peptide[144]	*E*, static	13 GV m^{-1}, 19.5 GV m^{-1}	CHARMM 36-AA, TIP3P, REMD	NPT (Berendsen, Parrinello–Rahman)	98 to 126 ns	Potential energy, RMSD, dipole moment
Dronpa[348]	*E*, static	0.4–1.3 GV m^{-1}	CHARMM27, water model not mentioned?	Langevin dynamics, 300 K	85 ps	Dipole moment
Ferritin[141]	*E*, static	1–4 MV m^{-1}	CHARMM36	NA	350 ns	RMSD, SASA
Fibronectin-hydroxyapatite[146]	*E*, static	250–1000 MV m^{-1}	Amber ff99SB ILDN, TIP3P	NPT (300 K, Berendsen, Parrinello–Rahman)	100 ns	Protein–ligand contacts, interaction energy, dipole moment, solvent radial distribution function
Hemoglobin[440]	*E*, linear/circularly polarized (5.9 GHz)	10, 7.1 V m^{-1} (looks like a typo, maybe authors meant GV m^{-1})	CHARMM36, TIP3P	NPT (310 K)	51 ns	RMSD, SS
HEWL[213]	*E*/*M*, oscillating (50–500 GHz)	1–5 GV m^{-1} (RMS)	CHARMM27, TIP3P	NVT (300 K, Nosé Hoover)	1 ns	RMSD, dipole moment
HEWL mutants[441]	*E*/*M*, static, oscillating (2.45 GHz)	100 to 1500 MV m^{-1} (RMS for osc, and amplitude for static)	GROMOS96 and SPC	NPT (Anderson–Hoover, 300 K)	2.5–25 ns	RMSD, dipole moment
HEWL mutant (2LZT)[401]	*E*/*M*, oscillating (2.45–100 GHz)	500 MV m^{-1} (RMS)	GROMOS96, SPC	NPT (300 K)	5 ns	H-bond
HEWL[186]	*E*, static, oscillating (2.45, 10, and 100 GHz)	50, 100, 200 MV m^{-1}	Amber ff99SB, TIP4P/2005	NPT (V-rescale, Parrinello–Rahman)	100 ns	Water density distribution, dipole moment
Human aquaporin 4[187]	*E*, static, oscillating (2.45, 100 GHz)	65 MV m^{-1}	CHARMM27, TIP3P	NPT (298 K, Nosé–Hoover, Langevin dynamics)	50 ns	Dipole moment
Human aquaporin 4 (3GD8) in lipid bilayer[442]	*E*, oscillating circularly polarized (100 GHz)	500 MV m^{-1}	CHARMM27, TIP3P	NPT (298 K)	60 ns	Pore radius, mean square displacement (MSD) of water
Human aquaporin 4[263]	*E*, static	200–500 MV m^{-1}	CHARMM27, TIP3P	NPT (298 K, Nosé–Hoover chains, Langevin dynamics piston)	2–11 ns	Ion conductivity, pore radius profile
Insulin chain-B (1ZNI)[443]	*E*, static, oscillating (2.45 GHz)	10–1000 MV m^{-1}	CHARMM27, TIP3P	NPT (300 K, 400 K, Nosé–Hoover, Langevin dynamics)	1.7–10 ns	RMSD, dipole moment, SS
Insulin chain-B (1ZNI)[444]	*E*, oscillating (1.225, 4.9 GHz)	10 to 500 MV m^{-1} (amplitude)	CHARMM27, TIP3P	NPT (300 K, Nosé–Hoover)	10 ns	RMSD, dipole moment, SS, R_g
Integrins[445]	*E*, static, oscillating (PEF)	0.0015, 0.015, 0.15 MV m^{-1} for static; 0.3, 1, 3 MV m^{-1} for pulse (pulse width 10, 100, 1000 μs)	Monte Carlo simulations	NA	20 s	Integrin clustering
Kinesin–tubulin[225]	*E*, static	30–100 MV m^{-1}	CHARMM36, TIP3P	NVT (300 K, Nosé–Hoover)	30 ns	RMSD, intermolecular contacts, dipole moment, translational/rotational work, SS
Laccase[446]	*E*, static	0.01–1000 MV m^{-1}	OPLS/AA, SPC	NPT (300 K)	50 ns	RMSD, H-bonds, dipole moment, SS, R_g, binding affinity
β-Lactoglobulin[447]	*E*, oscillating (2.45 GHz)	0.5 GV m^{-1}	Amber 99SB—ILDN	NPT (300, 333, 348, 363 K)	2 ns	SS, RMSD, RMSF, R_g, dipole moment, SASA

Table 3 (*continued*)

System of study [reference]	Type, shape of field	Field strength	Force field and water type (where available)	Condition of simulation	Simulation length	Observable
β-Lactoglobulin[148]	*E*, static	3000 MV m^{-1}	Amberff14SB, TIP3P	NVT (300, 400, 450 K, Berendsen, Langevin dynamics)	240 ns	RMSD, RMSF, SASA, dipole moment
L-type calcium channel[448]	*E*, static, oscillating (1, 2.5 GHz)	30 MV m^{-1}	GROMOS 96-43a1, SPC	NPT (310 K, Nosé–Hoover, Berendsen)	10 ns	RMSD, RMSF, H-bonds
Lysozyme, myoglobin[156]	*E*, static	75, 180, 424 MV m^{-1}	Amber ff99SB, TIP3P	NVT (Langevin dynamics, 298 K)	40 ns	Dipole moment, SASA
Model peptides[400]	*E*, static	1–5 GV m^{-1}	DFT/PCM, water, ethanol			Free energy, conformational stability, SS, H-bond(s)
Myofibrillar proteins[145]	*E*, static	0.8–2.8 MV m^{-1}	Gromacs 53a6, SPC	NPT (277 K, Berendsen thermostat and barostat)	30 ns	H-bonds, R_g
Myoglobin[190]	EM, oscillating (1 GHz)	0.001 to 500 MV m^{-1}	Perturbed matrix method	NPT (300 K)	10–20 ns	RMSD, free energy
Myoglobin[159]	*E*, static, pulse	100–1000 MV m^{-1}	GROMOS43a1, SPC	NVT (Berendsen)	100 ns	Dipole moment, SS
Myoglobin[449]	*E*, Gaussian pulse (time length = 8 ns), bipolar pulse (time length = 2 ns)	100–1000 MV m^{-1}	GROMOS96-43a1, SPC	NVT (300 K, Berendsen)	20 ns	Dipole moment, SS, H-bonds
Myoglobin[221]	*E*, static	100 V m^{-1} to 1000 MV m^{-1}	GROMOS96-43a1, SPC	NVT (300 K)	100 ns	Dipole moment, SS
Myoglobin[220]	*E*, oscillating (0.1–100 GHz)	2–200 MV m^{-1}	ffG43a1, SPC	NVT (200 K, Berendsen thermostat)	50 ns	Dipole moment
Voltage-gated ion channels: NavMs, NavPaS, HCN1[266]	*E*, static, pulse	97–108 MV m^{-1}	CHARMM36, TIP3P	NVT (300 K, Nosé–Hoover)	200 ns	SS, pore size, salt-bridge, ion conduction
Ovalbumin[140]	*E*, static, oscillating (2.5 GHz)	500 MV m^{-1}	CHARMM33, TIP3P	NPT (300, 320, 340, 360 K, Nosé–Hoover)	5 ns	SS, H-bond(s), saltbridge interactions, R_g, dipole moment, SASA
Peptides[450]	*E*, static	1.2–5 GV m^{-1}	DFT/PCM, vacuum			Free energy, geometry of the metal complex, dipole moment
α-Helix peptides[68]	*E*, pulsed, oscillating (1–2 GHz)	500 MV m^{-1}	CHARMM27, TIP3	NPT (310 K)	10 ns	RMSD, RMSF, dipole moment, SS
β-Sheet peptides[184]	*E*, static	4, 6, 10 GV m^{-1}	CHARMM27, TIP3P	NVE (300 K)	4 ns	Potential of mean force (PMF)
Pancreatic trypsin inhibitor (BPTI)[347]	*E*, static, square wave [pulse], oscillating	100 MV m^{-1}, 2 GV m^{-1} and 2.17 GV m^{-1}	CHARMM	NVE (100 K)	150 ps	RMSD, dipole moment
Pea protein isolate[126]	*E*, static	1 MV m^{-1}	OPLS-AA, TIP3P	NPT (300 K, V-rescale, Parrinello–Rahman)	25 ns	RMSD, RMSF, SASA, SS
Pectin methylesterase[142]	*E*, static	0.007–1000 MV m^{-1}	CHARMM27, TIP3P	NPT (323 K, Berendsen, Parrinello–Rahman)	5 ns	RMSF, RMSD, R_g, SASA, B-factor, water dynamics, hydration of enzyme, intra/inter-molecular H-bonds, dipole moment, Ramachandran plots
Amyloid-β peptide (2BEG)[234]	*E*, static	250, 500 MV m^{-1}	CHARMM27, TIP3P	NPT (300 K, Berendsen, Langevin dynamics)	50 ns	RMSD, SS, R_g, H-bonds
Polygalacturonase[451]	*E*, static	0.75–1.25 GV m^{-1}	CHARMM36, TIP3P	NPT	10 ns	SS, RMSD, RMSF, H-bonds, hydrophobic SASA, dipole moment, free binding energy
Soybean hydrophobic protein[452]	*E*, static	2, 4, 3000 MV m^{-1}	CHARMM27, TIP3P	NPT (300 K, Berendsen)	1 ns	RMSD, dipole moment, SS, R_g, SASA
SARS-CoV-2 spike protein[125]	*E*, static	0.1–10 MV m^{-1}	CHARMM36, TIP3P	NPT (300 K, Nosé Hoover, Parrinello–Rahman)	700 ns	RMSD, RMSF, SS
SARS-CoV-2 spike protein[139]	*E*, static	0.01–10 MV m^{-1}	CHARMM36, TIP3P	NPT (300 K, Nosé Hoover, Parrinello–Rahman)	700 ns	RMSD, RMSF, SS, free energy, electrostatic potential
Addlinespace serotonin 1A receptor (5-HT1AR)[135]	*E*, static	10–30 MV m^{-1}	Amber ff14SB, TIP3P	NPT (310 K, Nosé Hoover, Parrinello–Rahman)	600 ns	RMSD, R_g, contact number between protein and ligand, dipole moment.

Table 3 (*continued*)

System of study [reference]	Type, shape of field	Field strength	Force field and water type (where available)	Condition of simulation	Simulation length	Observable
Serotonin 1A receptor (5-HT1AR)[137]	*E*, static	20 MV m^{-1}	Amber ff14SB, TIP3P	NPT (310 K, velocity-rescaling, Parrinello–Rahman)	500 ns	RMSD, h-bond, residue contact count, dipole moment, SS
SOD1[216]	*E*, monopolar, bipolar nsPEF (pulse duration 2 ns)	100–700 MV m^{-1}	GROMOS96, SPC	NVT (300 K, V-rescale)	200 ns	Dipole moment, SS, RMSD, SASA, R_g
Soybean beta-conglycinin, soybean glycinin[180]	*E*, static	100, 200, 300 MV m^{-1}	Gromos 53a6, TIP3P	NPT (300 K)	30 ns	RMSD, H-bonds, SS
Amyloid-β fibrils[136]	*E*, static, oscillating (0.2 GHz)	200–400 MV m^{-1}	Amber ff99SB-ILDN, TIP3P	NPT (310 K, V-rescale, Parrinello–Rahman)	500 ns	SS, dipole moment, dielectric constant, H-bonds, PCA
Thioredoxin[182]	*E*, static	20–120 MV m^{-1}	SPC	NPT (300–350 K)	100 ns	pK_a, free energy, PCA, SASA, H-bonds, dipole moment
Tropomyosin[134]	*E*, static	0.5, 1.0, 2.0 MV m^{-1}	CHARMM36, SPC/E	NPT (298.15 K)	50 ns	SS, H-bonds, SASA
Tubulin[218]	*E*, static, oscillating (1 GHz)	30 MV m^{-1}	GROMOS96-43a1, SPC	NPT (300 K, V-rescale, Parrinello–Rahman)	500 ps	Elastic constant, Young's modulus
Tubulin[150]	*E*, static	5–75 MV m^{-1}	CHARMM36, TIP3P	NPT (310 K, Langevin dynamics, Nosé–Hoover–Langevin)	10 ns	RMSD, RMSF, dipole moment
Tubulin, kinesin[233]	*E*, oscillating (1–10 GHz)	30 MV m^{-1}	GROMOS96-43a1, SPC	NPT (310 K, Nosé–Hoover, Parrinello–Rahman)	10 ns	Flexibility of MTs, kinesin's affinity to tubulin
Tubulin–kinesin complex[217]	*E*, static	100 MV m^{-1}	CHARMM36, TIP3P	NVT (Nosé–Hoover thermostat)	30 ns	Dipole moment, RMSF, contact surface
Tubulin[78]	*E*, static	10 to 300 MV m^{-1}	Amber03 force field, TIP3P	NVT (300 K)	30 ns	Dipole moment, SS, shape and orientation (rotation) of protein
Tubulin ring[46]	*E*, static	50, 100 MV m^{-1}	Amberff14SB, TIP3P	NVT (Langevin thermostat, 0.5 ps coupling)	50 ns	Dipole moment, binding energy
αβ-Tubulin and kinesin[232]	*E*, oscillating (1 to 10 GHz)	30 MV m^{-1}	GROMOS96-43a1, SPC	NPT (310 K, Parrinello–Rahman)	500 ps	Kinesin's affinity to tubulin dimer
αβ-Tubulin dimer pairs[219]	*E*, oscillating (1–10 GHz)	30 MV m^{-1}	GROMOS96-43a1, SPC	NPT (310 K, V-rescale, Parrinello–Rahman)	300 ps	Elastic constant
αβ-Tubulin[453]	*E*, oscillating (900 MHz, 2450 MHz)	10 MV m^{-1}	GROMOS96-43a1, SPC	NPT (310 K, Nosé Hoover, Parrinello–Rahman)	10 ns	RMSD, elastic constant, Young's modulus
Trp-cage, Ctf, ubiquitin, lysozyme[79]	*E*, static	0 to 3 GV m^{-1}	OPLS-AA/L, vacuum	No-PBC (300 K, Berendsen)	10 ns	RMSD, degree of orientation, total internal energy
Ubiquitin[123]	*E*, time dependent	100 to 3000 MV m^{-1}	OPLS-AA, vacuum	NVT (300 K, Berendsen thermostat)	5 to 14 ns	Degree of orientation, RMSD
Ubiquitin[47]	*E*, static	3 GV m^{-1}–11 GV m^{-1}	OPLS/AA, vacuum	NVT (300 K, Nose thermostat)	50 ps	Unfolding, RMSD
Ubiquitin[138]	*E*, static	10–200 MV m^{-1}	Amber ff99sb-ILDN, SPC/E	NPT (310 K, Berendsen, Parrinello–Rahman)	1 μs	RMSD, RMSF, H-bonds, dipole moment, R_g
Ubiquitin[82]	*E*, static	0.1–5 GV m^{-1}	CHARMM36, TIP3P	NPT (300 K, Langevin dynamics, Nosé–Hoover)	5 ns	Dipole moment, SASA, RMSD, R_g, protein rotational diffusion, water diffusion
Ubiquitin[130]	*E*, static	0.05–3.0 GV m^{-1}	OPLS-AA, TIP4P	No-PBC (300 K, Berendsen)	10 ns	Dipole orientation, dipole moment, RMSF, RMSD, diffraction pattern
Voltage sensing domain (VSD) of the NaV1.5 sodium cardiac channel[454]	*E*, static	100–200 MV m^{-1}	CHARMM36, POPC	NPT (310 K, Nosé–Hoover, Parrinello–Rahman)	50 ns	RMSD, clustering structures, density profile of clusters based on RMSD and FNC (fraction of native contacts), free energy
Voltage-gated potassium (Kv) channel[455]	*E*, static	40–200 MV m^{-1}	CHARMM22, TIP3P	NPT (300 K, Langevin dynamics, Langevin piston)	20 ns	SS, RMSD, water density, pore-radius profile

Table 3 (*continued*)

System of study [reference]	Type, shape of field	Field strength	Force field and water type (where available)	Condition of simulation	Simulation length	Observable
Voltage-gated potassium (Kv4) channel[456]	*E*, static	250 MV m^{-1}	CHARMM36, TIP3P	NPT (310 K, Nosé–Hoover, Parrinello–Rahman)	4 ns	Pore radius, cross-sectional area, dipole moment
Voltage-gated potassium (Kv1.2) channel[457]	*E*, oscillating (36.75 37.06, 37.68, and 38.2 THz)	400 MV m^{-1}	CHARMM36m, CHARMM TIP3P	NPT (310 K, V-rescale, Parrinello–Rahman)	400 ns	Dihedral angle, ion permeation, RMSD, RMSF, potassium ion occupancy
Voltage-gated Ca^{2+} channel[143]	*E*, static	100, 200 MV m^{-1}	CHARMM36, TIP3P	NPT (310 K, Nosé–Hoover, Parrinello–Rahman)	50 ns	RMSD, fraction of native contacts (FNC), free energy

Atomistic simulations extend these experimental findings, albeit in a different range of EF strengths and timescales. Density functional theory/PCM (polarizable continuum model) calculations on model α-helices revealed a threshold near $\approx$2.6 GV m^{-1} for complete helix disruption when the EF is aligned with the helix dipole; importantly, removing the field allowed the misfolded peptide to refold to near-native geometry, even in polar solvents.[400] Constant-field MD of lysozyme in the 0.5 GV m^{-1} range under static and oscillating conditions showed accelerated hydrogen-bond breakage/reformation cycles, largely reversible except for some persistent losses in solvent-exposed charged regions at specific driving frequencies.[401] For ubiquitin, moderate fields ($\lesssim$0.5 GV m^{-1}) induced reversible dipole reorientation and minor secondary-structure changes, while higher fields (1–2 GV m^{-1}) could still be reversible if switched off prior to overstretching.[140]

Analogies can be drawn – cautiously – from protein refolding after mechanical unfolding,[229] reassembly of supramolecular protein complexes, and reversible disruption of peptide–peptide interfaces. Across these contexts, reversibility hinges on perturbations that do not cross irreversible kinetic barriers such as extensive hydrophobic-core exposure or covalent bond scission. For EF perturbations, key determinants include the field vector relative to the intrinsic protein dipole, temporal waveform, and structural context (*e.g.*, solvent-exposed flexible tails *versus* buried secondary-structure cores). Designing EF protocols that exploit such "safe windows" could enable reversible, on-demand modulation of protein structure and function.

Across field modalities, the characteristic recovery time and dominant sources of irreversibility span many orders of magnitude. In EF-X, perturbations delivered on nanosecond timescales can drive reversible, collective motions in crystals without apparent structural degradation.[22] In sub-THz/THz irradiation, the primary solvent relaxation occurs on ps–ns timescales, suggesting that reversible modulation is plausible provided that the field does not trigger large-scale unfolding or chemical modification.[24,163] By contrast, in electrode-based PEF experiments, irreversibility often originates from indirect pathways (Joule heating, pH gradients, ROS, and bubble interfaces), which act on ms–min timescales and can accumulate under repeated exposures. This is particularly relevant for emerging protein/peptide-based piezoelectric platforms,[402] where longevity may be limited by cumulative electrochemical and hydration changes; mitigating strategies include minimizing duty cycle (an E^2-weighted "dose"), using bipolar pulses, and isolating electrodes from the protein-containing volume.[266]

5 Conclusion

External EFs offer a powerful, reagent-free handle to perturb proteins and to modulate their interactions and function. Across the studies reviewed here, EFs couple directly to charged and dipolar groups, biasing rigid-body motion, reshaping intra- and inter-molecular electrostatics, and – when sufficiently strong or resonant with intrinsic motions – modifying secondary/tertiary/quaternary

structure. In parallel, high-field protocols often introduce indirect electrophysical and electrochemical stresses – Joule heating, electrohydrodynamic flows, shock/cavitation, electrolysis-driven pH gradients, reactive oxygen/nitrogen species (ROS/RNS), and bubble interfaces – that can dominate the observed outcome if not controlled.

A central message is that "EF effects on proteins" should be interpreted as a competition between direct EF–protein coupling and solvent-/interface-mediated pathways. The balance is set by the field strength, waveform and frequency, exposure time (or duty cycle), and geometry (electrode-based *vs.* contactless), together with protein stability and solution conditions (conductivity, ionic strength, buffering capacity, redox environment). When indirect pathways are mitigated, reversible control becomes feasible: ultrafast nanosecond perturbations in EF-X can drive coordinated motions along functional modes,[22] while pulsed MV m^{-1} regimes and THz exposures can modulate binding, catalysis and supramolecular assembly on experimentally accessible timescales.[24,25,225] When indirect stresses accumulate (heating, electrochemical byproducts, interface adsorption), irreversible unfolding and aggregation are more likely.

Preliminary design rules for EF-based protein control:

• Match the field vector to the target degree of freedom. Orientation and torque couple to the permanent dipole moment and charge distribution, while local polarization and bond-scale rearrangements couple to induced dipoles and heterogeneous internal electrostatics. Electro-optical experiments and modelling commonly place protein dipole moments in the $\sim 10^2$–10^3 D range, so fields of order 1–10 MV m^{-1} already give $\mu E \sim k_B T$ and can bias orientation, whereas remodeling tertiary interfaces, oligomer contacts, or buried secondary structure typically requires substantially larger effective fields and/or longer forcing, and is strongly direction-dependent.[22,81,113,116,225]

• Treat dose as a coupled strength–time problem. For many indirect pathways (Joule/dielectric heating, electrolysis, electrode corrosion, electrothermal/electrohydrodynamic flows), the accumulated "damage" or energy deposition scales approximately with an E^2-type integral over the duty cycle (*e.g.* $\propto \int E^2(t)\mathrm{d}t$ or $\propto \sigma E^2$ for Ohmic heating), so short pulses can access large peak fields while limiting the bulk temperature rise and electrochemical accumulation.[294,299,403] For direct EF-driven conformational/functional changes, however, the field–time trade-off can be much steeper: if the EF lowers an effective activation barrier, the response rate can follow an Arrhenius-like dependence $k(E) \approx k_0 \exp\left[-\frac{\Delta G^{\ddagger}(E)}{k_B T}\right]$, with $\Delta G^{\ddagger}(E) \simeq \Delta G_0^{\ddagger} - \Delta\mu^{\ddagger} E$ (or related forms), implying an exponential sensitivity to E.[22,225,352–354] For pulsed protocols, explicitly report both the single-pulse width τ_p and the cumulative on-time $\tau_{on} = N\tau_p$ (and also the total elapsed exposure time), because large-N pulse trains can have $\tau_{on} \ll$ elapsed time yet still produce a substantial thermal/chemical dose.

• Tune spectral content (frequency and waveform) to the target timescale, and to suppress unwanted interfacial physics. Protein dynamics spans picoseconds to days, so efficient forcing requires matching the stimulus bandwidth to the relaxation time of the targeted coordinate; narrowband drives can preferentially address a chosen dynamic window, whereas fast-rise pulses are inherently broadband and can excite multiple dispersive processes in water and biomolecules.[77,220,404] Frequency also selects which macroscopic couplings dominate near interfaces: at low frequencies (typically $\lesssim$10 kHz) electrical-double-layer charging and induced-charge electroosmosis are strong, while at higher frequencies the double layer cannot follow and electroosmotic contributions diminish.[304–306] In the GHz–THz range, coupling can shift toward fast polarization dynamics and collective modes; outcomes then depend critically on absorption and duty cycle (thermal *vs.* nonthermal regimes).[24,177]

• Control the matrix chemistry and interfaces. Buffer conductivity and thermal properties set Joule heating and electrothermal flows; buffer capacity sets pH excursions; electrode composition and dissolved oxygen/metal ions/peroxides set susceptibility to electrolysis, corrosion, and ROS/RNS chemistry. Use matched chemical controls (conductivity, buffering, scavengers), minimize direct electrode contact when possible (coatings, salt bridges), and manage polarity/pulse structure (*e.g.* bipolar or burst protocols) to separate direct EF effects from chemistry-driven artifacts.[317,319–324]

• Account for solvent-mediated thermodynamics and nonlinear dielectric response. Strong static and oscillating fields can reorganize water structure/dynamics (dielectric saturation, anisotropy, altered hydrogen-bond statistics), changing entropic contributions and effective local fields that feed back on protein stability and kinetics.[356–359,404] These solvent responses may also limit durability in repeated-use bioelectronic and piezoelectric protein/peptide platforms.[402]

• Validate "direct" EF mechanisms with orthogonal controls and quantitative modelling. Because indirect pathways can mimic "nonthermal" effects, combine structural/functional readouts with monitoring of temperature, pH, and electrochemical/ROS markers, and report geometry, conductivity, waveform details, and local-field estimates (or EM/thermal simulations) to enable reproducibility and cross-modality comparison.[47,297–299,403]

Looking forward, closing the gap between simulations and experiments will require multiscale modelling (including explicit interfaces and realistic conductivity), improved force fields for polarization and charge transfer, and experimental platforms that deliver well-calibrated fields while simultaneously reporting structural and functional observables. Such advances should enable EF protocols that are not generic denaturants but rather tunable physical stimuli for selective, reversible and sustainable control of protein function.

Author contributions

M. C.: conceptualization; funding acquisition; project administration; resources; supervision; data curation; visualization; writing – original draft; writing – review & editing. S. K. P.: visualization; writing – review & editing. T. Z.: visualization; writing – original draft. M. P.: visualization; writing – original draft. D. G. B. C.: visualization; writing – original draft. J. P.: visualization; writing – original draft. D. H.: visualization. P. M.: writing – review & editing.

M. L.: writing – review & editing. F. A.: visualization; writing – original draft; writing – review & editing. N. J. E.: writing – original draft. C. C.: writing – original draft. E. G. M.: writing – review & editing. Contributor roles follow the ANSI/NISO CRediT taxonomy.

Conflicts of interest

There are no conflicts to declare.

List of abbreviations

Aβ	Amyloid-beta
AC	Alternating current
AQP	Aquaporin
AdoHcy	*S*-Adenosyl-L-homocysteine
AFM	Atomic force microscopy
ANS	8-anilino-1-naphthalenesulfonic acid
anti-DNP	Antidinitrophenyl
AP	Alkaline phosphatase
ATR-FTIR	Attenuated total reflectance Fourier-transform IR
BCA	Bicinchoninic-acid protein assay
BSA	Bovine serum albumin
CD	Circular dichroism
CLSM	Confocal laser scanning microscopy
CW	Continuous wave
DC	Direct current
DFT	Density functional theory
DLS	Dynamic light scattering
DNPH	2,4-Dinitrophenyl-hydrazine (carbonyl assay)
DSC	Differential scanning calorimetry
DTNB	5,5′-Dithiobis-(2-nitrobenzoic acid)
EF	Electric field
EF-X	EF X-ray crystallography
EGFP	Enhanced green fluorescent protein
EM	Electromagnetic
EMC	Expand–maximize–compress
EWOD	Electrowetting-on-dielectric
FNC	Fraction of native contacts
FTIR	Fourier-transform infrared
GFP	Green fluorescent protein
GFPuv5	Ultraviolet-excitable GFP variant (uv5)
GPCR	G-protein-coupled receptor
H-bond	Hydrogen bond
HEWL	Hen egg-white lysozyme
HPLC	High-performance liquid chromatography
HRTEM	High-resolution transmission EM
HRP	Horseradish peroxidase
HSA	Human serum albumin
HPG	High-power generator
HV	High voltage
ITO	Indium tin oxide
LDH	Lactate dehydrogenase
LLPS	Liquid–liquid phase separation
MD	Molecular dynamics
Mb	Myoglobin
MT	Microtubule
MTA	5′-Methylthioadenosine
NEMD	Non-equilibrium molecular dynamics
NMR	Nuclear magnetic resonance
nsPEF	Nanosecond pulsed electric field
OPA	*o*-Phthalaldehyde
OVA	Ovalbumin
PCA	Principal component analysis
PDB	Protein data bank
PDMS	Poly(dimethylsiloxane)
PEF	Pulsed electric field
POD	Peroxidase
PPI	Protein–protein interaction
PPO	Polyphenol oxidase
PL	Photoluminescence
PMF	Potential of mean force
R_g	Radius of gyration
RMSD	Root-mean-square deviation
RMSF	Root-mean-square fluctuation
ROA	Raman optical activity
ROS	Reactive oxygen species
RNS	Reactive nitrogen species
RPC	Relative protein concentration
RXS	Reactive species (generic)
SASA	Solvent-accessible surface area
SAXS	Small-angle X-ray scattering
SEC	Size-exclusion chromatography
SEM	Scanning electron microscopy
SDS–PAGE	Sodium dodecyl-sulfate polyacrylamide-gel electrophoresis
SiR	Silicon–rhodamine (fluorophore)
SPI	Single-particle imaging
SPR	Surface plasmon resonance
TEM	Transmission electron microscopy
ThT	Thioflavin T
Trp	Tryptophan
Tyr	Tyrosine
Ub	Ubiquitin
UV-vis	Ultraviolet-visible spectroscopy
VCD	Vibrational circular dichroism
VG	Voltage generator
VGIC	Voltage-gated ion channel
VSD	Voltage-sensing domain
XFEL	X-Ray free-electron laser

Data availability

No primary research results, software or code have been included and no new data were generated or analysed as part of this review.

Acknowledgements

This research was funded by Czech Science Foundation grant number 20-06873X (MC, SKP, TZ, MP, DGBC, JP), 25-16700S

(DH), Czech Academy of Sciences PPLZ program, project n. L100672501 (MP) and (CC) by the Swedish Research Council *via* projects 2018-00740, 2023-04346 and (CC, EGM) *via* the Röntgen-Ångström Cluster (2019-03935). CC also acknowledges the Helmholtz Association through the Center for Free-Electron Laser Science at DESY. Tasnia Tarana and Neuron Collective are acknowledged for graphical design. Ondřej Kučera is acknowledged for valuable comments on the manuscript. ChatGPT tools were used as assistants for writing and rephrasing based on the inputs and prompts by the authors.

Notes and references

1 G. E. Neurohr and A. Amon, *Trends Cell Biol.*, 2020, **30**, 213–225.
2 R. Milo and R. Phillips, *Cell biology by the numbers*, Garland Science, 2015.
3 B. Alberts, A. Johnson, J. Lewis, M. Raff, K. Roberts and P. Walter, *Mol. Biol. Cell*, Garland Science, 4th edn, 2002.
4 R. Nussinov, Y. Liu, W. Zhang and H. Jang, *RSC Chem. Biol.*, 2023, **4**, 850–864.
5 L. Orellana, *Front. Mol. Biosci.*, 2019, **6**, 117.
6 H. Ai, M. Pan and L. Liu, *ACS Cent. Sci.*, 2024, **10**, 1442–1459.
7 H. Nada, Y. Choi, S. Kim, K. S. Jeong, N. A. Meanwell and K. Lee, *Signal Transduction Targeted Ther.*, 2024, **9**, 341.
8 D. Vasudevan, *Textbook of Biochemistry*, Jaypee Brothers Medical Publishers (P) Ltd., 6th edn, 2011, pp. 27–39.
9 C. Soto and S. Pritzkow, *Nat. Neurosci.*, 2018, **21**, 1332–1340.
10 C. Scheckel and A. Aguzzi, *Nat. Rev. Genet.*, 2018, **19**, 405–418.
11 F. Chiti and C. M. Dobson, *Annu. Rev. Biochem.*, 2017, **86**, 27–68.
12 S. Verbrugge, Z. Lansky and E. J. G. Peterman, *Proc. Natl. Acad. Sci. U. S. A.*, 2009, **106**, 17741–17746.
13 W. A. M. Loenen, D. T. F. Dryden, E. A. Raleigh, G. G. Wilson and N. E. Murray, *Nucleic Acids Res.*, 2014, **42**, 3–19.
14 O. Brandman and R. S. Hegde, *Nat. Struct. Mol. Biol.*, 2016, **23**, 7–15.
15 R. Croce and H. van Amerongen, *Photosynth. Res.*, 2013, **116**, 153–166.
16 S. G. Boxer and T. Head-Gordon, *Chem. Rev.*, 2025, **125**, 6871–6873.
17 M. A. Rothermund, S. J. Koehler and V. Vaissier Welborn, *Chem. Rev.*, 2024, **124**, 13331–13369.
18 C. Yang, Y. Guo, H. Zhang and X. Guo, *Chem. Rev.*, 2025, **125**, 223–293.
19 Z. Long, J. Meng, L. R. Weddle, P. E. Videla, J. P. Menzel, D. G. A. Cabral, J. Liu, T. Qiu, J. M. Palasz, D. Bhattacharyya, C. P. Kubiak, V. S. Batista and T. Lian, *Chem. Rev.*, 2025, **125**, 1604–1628.
20 S. Ishizawa, K. Fujimura, K. Oisaki, S. Sato and J. Ohata, *ChemCatChem*, 2025, **17**, e202402125.
21 D. E. Chafai, V. Sulimenko, D. Havelka, L. Kubínová, P. Dráber and M. Cifra, *Adv. Mater.*, 2019, **31**, 1903636.
22 D. R. Hekstra, K. I. White, M. A. Socolich, R. W. Henning, V. Šrajer and R. Ranganathan, *Nature*, 2016, **540**, 400–405.
23 R. A. Petrella, K. H. Schoenbach and S. Xiao, *IEEE Trans. Plasma Sci.*, 2016, **44**, 708–714.
24 J.-i Sugiyama, Y. Tokunaga, M. Hishida, M. Tanaka, K. Takeuchi, D. Satoh and M. Imashimizu, *Nat. Commun.*, 2023, **14**, 2825.
25 C. M. Hough, D. N. Purschke, C. Bell, A. P. Kalra, P. J. Oliva, C. Huang, J. A. Tuszynski, B. J. Warkentin and F. A. Hegmann, *Biomed. Opt. Express*, 2021, **12**, 5812–5828.
26 C. Marar, Y. Jiang, Y. Li, L. Lan, N. Zheng, G. Chen, C. Yang and J.-X. Cheng, *Sci. Adv.*, 2024, **10**, eado5560.
27 A. Wada and H. Nakamura, *Nature*, 1981, **293**, 757–758.
28 M. N. Alves, S. E. Neto, A. S. Alves, B. M. Fonseca, A. Carrêlo, I. Pacheco, C. M. Paquete, C. M. Soares and R. O. Louro, *Front. Microbiol.*, 2015, **6**, 665.
29 L. Li, Z. Jia, Y. Peng, S. Godar, I. Getov, S. Teng, J. Alper and E. Alexov, *Sci. Rep.*, 2017, **7**, 8237.
30 T. G. Castro, F.-D. Munteanu and A. Cavaco-Paulo, *Biomolecules*, 2019, **9**, 116.
31 C. Kweyu, L. Feng, M. Stein and P. Benner, *Comput. Visualization Sci.*, 2020, **23**, 15.
32 P. Ren, J. Chun, D. G. Thomas, M. J. Schnieders, M. Marucho, J. Zhang and N. A. Baker, *Q. Rev. Biophys.*, 2012, **45**, 427–491.
33 M.-Y. Tsai, W. Zheng, D. Balamurugan, N. P. Schafer, B. L. Kim, M. S. Cheung and P. G. Wolynes, *Protein Sci.*, 2016, **25**, 255–269.
34 R. H. W. Funk and F. Scholkmann, *Prog. Biophys. Mol. Biol.*, 2023, **177**, 185–201.
35 M. T. Neves-Petersen and S. B. Petersen, *Biotechnology Annual Review*, Elsevier, 2003, vol. 9, pp. 315–395.
36 A. Chakravorty, Z. Jia, L. Li, S. Zhao and E. Alexov, *J. Chem. Theory Comput.*, 2018, **14**, 1020–1032.
37 Z. Zhang, S. Witham and E. Alexov, *Phys. Biol.*, 2011, **8**, 035001.
38 A. Macchiarulo, G. Costantino, R. Sbaglia, S. Aiello, M. Meniconi and R. Pellicciari, *Proteins: Struct., Funct., Bioinf.*, 2003, **50**, 609–619.
39 A. Warshel, P. K. Sharma, M. Kato, Y. Xiang, H. Liu and M. H. M. Olsson, *Chem. Rev.*, 2006, **106**, 3210–3235.
40 S. D. Fried, S. Bagchi and S. G. Boxer, *Science*, 2014, **346**, 1510–1514.
41 S. D. Fried and S. G. Boxer, *Annu. Rev. Biochem.*, 2017, **86**, 387–415.
42 C. Zheng, Z. Ji, I. I. Mathews and S. G. Boxer, *Nat. Chem.*, 2023, **15**, 1715–1721.
43 F. Bezanilla, *Physiol. Rev.*, 2000, **80**, 555–592.
44 A. L. Hodgkin and A. F. Huxley, *J. Physiol.*, 1952, **116**, 449–472.
45 H. C. Lai and L. Y. Jan, *Nat. Rev. Neurosci.*, 2006, **7**, 548–562.
46 J. Průša, A. T. Ayoub, D. E. Chafai, D. Havelka and M. Cifra, *Comput. Struct. Biotechnol. J.*, 2021, **19**, 1488–1496.
47 A. Sinelnikova, T. Mandl, C. Östlin, O. Grånäs, M. N. Brodmerkel, E. G. Marklund and C. Caleman, *Chem. Sci.*, 2021, **12**, 2030–2038.
48 M. A. Malik, M. A. Sheikh and N. A. Mir, *Food Biosci.*, 2024, **61**, 104636.
49 J. Marín-Sánchez, A. Berzosa, I. Álvarez, C. Sánchez-Gimeno and J. Raso, *Bioelectricity*, 2024, **6**, 154–166.

50 C. Zhang, X. Lyu, R. N. Arshad, R. M. Aadil, Y. Tong, W. Zhao and R. Yang, *Food Chem.*, 2023, **403**, 134367.
51 Y.-F. Liu, I. Oey, P. Bremer, A. Carne and P. Silcock, *Compr. Rev. Food Sci. Food Saf.*, 2019, **18**, 986–1002.
52 A. Taha, F. Casanova, P. Šimonis, V. Stankevič, M. A. E. Gomaa and A. Stirkė, *Foods*, 2022, **11**, 1556.
53 X. Jiao, W. Chen and D. Fan, *Curr. Opin. Food Sci.*, 2022, **48**, 100936.
54 K. Takaki, K. Takahashi, A. Guionet and T. Ohshima, *Molecules*, 2021, **26**, 6288.
55 S. Zhang, L. Sun, H. Ju, Z. Bao, X.-A. Zeng and S. Lin, *Food Res. Int.*, 2021, **139**, 109914.
56 S. K. Vanga, J. Wang, S. Jayaram and V. Raghavan, *Processes*, 2021, **9**, 722.
57 R. M. Rodrigues, Z. Avelar, L. Machado, R. N. Pereira and A. A. Vicente, *Food Res. Int.*, 2020, **137**, 109709.
58 D. Niu, X.-A. Zeng, E.-F. Ren, F.-Y. Xu, J. Li, M.-S. Wang and R. Wang, *Food Res. Int.*, 2020, **137**, 109715.
59 L. H. Fasolin, R. N. Pereira, A. C. Pinheiro, J. T. Martins, C. C. P. Andrade, O. L. Ramos and A. A. Vicente, *Food Res. Int.*, 2019, **125**, 108586.
60 R. N. Pereira, R. M. Rodrigues, Ó. L. Ramos, A. C. Pinheiro, J. T. Martins, J. A. Teixeira and A. A. Vicente, *J. Agric. Food Chem.*, 2018, **66**, 11227–11233.
61 Z. Han, M.-J. Cai, J.-H. Cheng and D.-W. Sun, *Trends Food Sci. Technol.*, 2018, **75**, 1–9.
62 S. G. Giteru, I. Oey and M. A. Ali, *Trends Food Sci. Technol.*, 2018, **72**, 91–113.
63 L. Barsotti, E. Dumay, T. H. Mu, M. D. Fernandez Diaz and J. C. Cheftel, *Trends Food Sci. Technol.*, 2001, **12**, 136–144.
64 S. J. Beebe, *Bioelectrochemistry*, 2015, **103**, 52–59.
65 P. M. Graybill and R. V. Davalos, *Cancers*, 2020, **12**, 1132.
66 J. N. Israelachvili, *Intermolecular and Surface Forces*, Elsevier, 3rd edn, 2011.
67 R. S. Fisher, J. Liao, S. Y. Ahn, N. Modi, A. K. Kidane and A. C. Obermeyer, *Annu. Rev. Chem. Biomol. Eng.*, 2025, **16**, 119–145.
68 Q. Zhang, D. Shao, P. Xu and Z. Jiang, *Polymers*, 2022, **14**, 123.
69 D. Miklavcic, *Handbook of electroporation*, Springer, Cham, 2019.
70 Y. Shen, H. Wang and S. Fan, *Adv. Opt. Photonics*, 2025, **17**, 295.
71 H. Rubinsztein-Dunlop, A. Forbes, M. V. Berry, M. R. Dennis, D. L. Andrews, M. Mansuripur, C. Denz, C. Alpmann, P. Banzer, T. Bauer, E. Karimi, L. Marrucci, M. Padgett, M. Ritsch-Marte, N. M. Litchinitser, N. P. Bigelow, C. Rosales-Guzmán, A. Belmonte, J. P. Torres, T. W. Neely, M. Baker, R. Gordon, A. B. Stilgoe, J. Romero, A. G. White, R. Fickler, A. E. Willner, G. Xie, B. McMorran and A. M. Weiner, *J. Opt.*, 2016, **19**, 013001.
72 S. B. Glybovski, S. A. Tretyakov, P. A. Belov, Y. S. Kivshar and C. R. Simovski, *Phys. Rep.*, 2016, **634**, 1–72.
73 L. Vincenti, P. Pellegrino, M. Cascione, V. De Matteis, I. Farella, F. Quaranta and R. Rinaldi, *Mater. Des.*, 2024, **243**, 113036.
74 S. Toyama, T. Seki, Y. Kohno, Y. O. Murakami, Y. Ikuhara and N. Shibata, *Nat. Rev. Electr. Eng.*, 2025, **2**, 27–41.
75 E. Oswald, K. Palanisamy and C. Kranz, *Curr. Opin. Electrochem.*, 2022, **34**, 100965.
76 H.-X. Zhou and X. Pang, *Chem. Rev.*, 2018, **118**, 1691–1741.
77 D. Nettels, N. Galvanetto, M. T. Ivanović, M. Nüesch, T. Yang and B. Schuler, *Nat. Rev. Phys.*, 2024, **6**, 587–605.
78 P. Marracino, D. Havelka, J. Průša, M. Liberti, J. Tuszynski, A. T. Ayoub, F. Apollonio and M. Cifra, *Sci. Rep.*, 2019, **9**, 10477.
79 E. G. Marklund, T. Ekeberg, M. Moog, J. L. P. Benesch and C. Caleman, *J. Phys. Chem. Lett.*, 2017, **8**, 4540–4544.
80 G. Mithieux, F. Chauvin, B. Roux and B. Rousset, *Biophys. Chem.*, 1985, **22**, 307–316.
81 D. Porschke, C. Créminon, X. Cousin, C. Bon, J. Sussman and I. Silman, *Biophys. J.*, 1996, **70**, 1603–1608.
82 A. Chakraborty and R. Venkatramani, *ChemPhysChem*, 2023, **24**, e202200646.
83 J. P. Landers, *Handbook of capillary electrophoresis*, CRC Press, 1996.
84 H. Rehm and H. Rehm, *Protein biochemistry and proteomics*, Elsevier, Academic Press, Amsterdam, Boston, 4th edn, 2006.
85 M. Uppalapati, Y.-M. Huang, V. Aravamuthan, T. N. Jackson and W. O. Hancock, *Integr. Biol.*, 2011, **3**, 57–64.
86 M. Uppalapati, Y.-M. Huang, T. N. Jackson and W. O. Hancock, *Small*, 2008, **4**, 1371–1381.
87 K. J. Böhm, N. E. Mavromatos, A. Michette, R. Stracke and E. Unger, *Electromagn. Biol. Med.*, 2005, **24**, 319–330.
88 K. Kim, A. Sikora, K. S. Nakayama, M. Umetsu, W. Hwang and W. Teizer, *J. Appl. Phys.*, 2015, **117**, 144701.
89 M. G. L. Van den Heuvel, M. P. De Graaff, S. G. Lemay and C. Dekker, *Proc. Natl. Acad. Sci. U. S. A.*, 2007, **104**, 7770–7775.
90 M. G. L. van den Heuvel, C. T. Butcher, S. G. Lemay, S. Diez and C. Dekker, *Nano Lett.*, 2005, **5**, 235–241.
91 N. Isozaki, H. Shintaku, H. Kotera, T. L. Hawkins, J. L. Ross and R. Yokokawa, *Sci. Rob.*, 2017, **2**, eaan4882.
92 R. Stracke, K. Böhm, L. Wollweber, J. Tuszynski and E. Unger, *Biochem. Biophys. Res. Commun.*, 2002, **293**, 602–609.
93 S. Kobayashi, *Biochim. Biophys. Acta, Spec. Sect. Biophys. Subj.*, 1964, **88**, 541–552.
94 D. Riveline, A. Ott, F. Jülicher, D. A. Winkelmann, O. Cardoso, J.-J. Lacapère, S. Magnúsdóttir, J.-L. Viovy, L. Gorre-Talini and J. Prost, *Eur. Biophys. J.*, 1998, **27**, 403–408.
95 M. E. Arsenault, H. Zhao, P. K. Purohit, Y. E. Goldman and H. H. Bau, *Biophys. J.*, 2007, **93**, L42–L44.
96 C. Wigge, H. Hinssen, G. Reiss and S. Herth, *Appl. Phys. Lett.*, 2010, **96**, 243703.
97 A. M. Roseman, S. Chen, H. White, K. Braig and H. R. Saibil, *Cell*, 1996, **87**, 241–251.
98 H. Noji, R. Yasuda, M. Yoshida and K. Kinosita, *Nature*, 1997, **386**, 299–302.
99 W. Wriggers and K. Schulten, *Proteins: Struct., Funct., Bioinf.*, 1997, **29**, 1–14.
100 H. Omote, N. Sambonmatsu, K. Saito, Y. Sambongi, A. Iwamoto-Kihara, T. Yanagida, Y. Wada and M. Futai, *Proc. Natl. Acad. Sci. U. S. A.*, 1999, **96**, 7780–7784.

101 M. D. Daily, G. N. Phillips and Q. Cui, *J. Mol. Biol.*, 2010, **400**, 618–631.
102 J. R. Braxton, H. Shao, E. Tse, J. E. Gestwicki and D. R. Southworth, *Nat. Struct. Mol. Biol.*, 2024, **31**, 1848–1858.
103 A. Oleinikova, P. Sasisanker and H. Weingärtner, *J. Phys. Chem. B*, 2004, **108**, 8467–8474.
104 V. Raicu and Y. Feldman, *Dielectric relaxation in biological systems: Physical principles, methods, and applications*, Oxford University Press, USA, 2015.
105 *Molecular Electro-Optics*, ed. S. Krause, Springer US, Boston, MA, 1981.
106 D. Porschke, *Annu. Rev. Phys. Chem.*, 1985, **36**, 159–178.
107 S. P. Stoylov and M. V. Stoimenova, *Molecular and colloidal electro-optics*, CRC Press, 2016, vol. 134.
108 L. Keszthelyi, *Biochim. Biophys. Acta, Biomembr.*, 1980, **598**, 429–436.
109 Y. Kimura, A. Ikegami, K. Ohno, S. Saigo and Y. Takeuchi, *Photochem. Photobiol.*, 1981, **33**, 435–439.
110 K. Barabás, A. Dér, Z. Dancsházy, P. Ormos, L. Keszthelyi and M. Marden, *Biophys. J.*, 1983, **43**, 5–11.
111 Y. Kimura, M. Fujiwara and A. Ikegami, *Biophys. J.*, 1984, **45**, 615–625.
112 S. P. Stoylov, G. Todorov and A. Zhivkov, *Bioelectrochem. Bioenerg.*, 1984, **12**, 49–55.
113 J. Antosiewicz and D. Porschke, *Biochemistry*, 1989, **28**, 10072–10078.
114 A. Dér, R. Tóth-Boconádi, L. Keszthelyi, H. Kramer and W. Stoeckenius, *FEBS Lett.*, 1995, **377**, 419–420.
115 D. Porschke, *Biophys. J.*, 1996, **71**, 3381–3391.
116 T. Schönknecht and D. Pörschke, *Biophys. Chem.*, 1996, **58**, 21–28.
117 Y. Sugiyama, T. Inoue, M. Ikematsu, M. Iseki and T. S. T. Sekiguchi, *Jpn. J. Appl. Phys.*, 1997, **36**, 5674.
118 R. Neutze, R. Wouts, D. van der Spoel, E. Weckert and J. Hajdu, *Nature*, 2000, **406**, 752–757.
119 N.-T. D. Loh and V. Elser, *Phys. Rev. E:Stat., Nonlinear, Soft Matter Phys.*, 2009, **80**, 026705.
120 C. Östlin, N. Timneanu, C. Caleman and A. V. Martin, *Struct. Dyn.*, 2019, **6**, 044103.
121 T. Mandl, C. Östlin, I. E. Dawod, M. N. Brodmerkel, E. G. Marklund, A. V. Martin, N. Timneanu and C. Caleman, *J. Phys. Chem. Lett.*, 2020, **11**, 6077–6083.
122 A. Wollter, E. De Santis, T. Ekeberg, E. G. Marklund and C. Caleman, *J. Chem. Phys.*, 2024, **160**, 114108.
123 A. Sinelnikova, T. Mandl, H. Agelii, O. Grånäs, E. G. Marklund, C. Caleman and E. De Santis, *Biophys. J.*, 2021, **120**, 3709–3717.
124 M. Amin, J.-M. Hartmann, A. K. Samanta and J. Küpper, *J. Am. Chem. Soc.*, 2025, **147**, 7445–7451.
125 C. R. Arbeitman, P. Rojas, P. Ojeda-May and M. E. Garcia, *Nat. Commun.*, 2021, **12**, 5407.
126 Z.-L. Chen, Y. Li, J.-H. Wang, R. Wang, Y.-X. Teng, J.-W. Lin, X.-A. Zeng, M.-W. Woo, L. Wang and Z. Han, *Int. J. Biol. Macromol.*, 2023, **244**, 125082.
127 A. Guionet, T. Fujiwara, H. Sato, K. Takahashi, K. Takaki, M. Matsui, T. Tanino and T. Ohshima, *J. Electrost.*, 2021, **112**, 103597.
128 A. Kadek, K. Lorenzen and C. Uetrecht, *Drug Discovery Today: Technol.*, 2021, **39**, 89–99.
129 T. Kierspel, A. Kadek, P. Barran, B. Bellina, A. Bijedic, M. N. Brodmerkel, J. Commandeur, C. Caleman, T. Damjanović and I. Dawod, *et al.*, *Anal. Bioanal. Chem.*, 2023, **415**, 4209–4220.
130 H. Agelii, E. L. S. Jakobsson, E. D. Santis, G. Elfrink, T. Mandl, E. G. Marklund and C. Caleman, *Phys. Chem. Chem. Phys.*, 2025, **27**, 10939–10948.
131 E. D. Santis, T. Mandl, J. C. K. Kung, K. Huynh, S. Daly, L. A. D'Alessandro, L. MacAleese, C. Uetrecht, E. G. Marklund and C. Caleman, *Phys. Chem. Chem. Phys.*, 2025, **27**, 14767–14776.
132 B. Alberts, *Molecular biology of the cell*, Garland Science, 2017.
133 S. Kalita, D. Danovich and S. Shaik, *J. Am. Chem. Soc.*, 2025, **147**, 2626–2641.
134 X. Hu, H. Wang, Y. Hu, P. Wen, X. Wu and Z. Tu, *Food Chem.*, 2025, **463**, 141376.
135 L. Guan, B. Qi, J. Tan, Y. Chen, Y. Sun, Q. Zhang and Y. Zou, *J. Chem. Inf. Model.*, 2025, **65**, 2066–2079.
136 M. Makhkamov, A. Baev, E. Kurganov and J. Razzokov, *Sci. Rep.*, 2024, **14**, 22246.
137 L. Guan, J. Tan, B. Qi, Y. Chen, M. Cao, Q. Zhang and Y. Zou, *Biophys. Chem.*, 2024, **312**, 107283.
138 Y. Shuto, E. Walinda, D. Morimoto and K. Sugase, *J. Phys. Chem. B*, 2023, **127**, 7417–7430.
139 A. Lipskij, C. Arbeitman, P. Rojas, P. Ojeda-May and M. E. Garcia, *Viruses*, 2023, **15**, 2405.
140 W. A. Müller, J. R. Sarkis, L. D. F. Marczak and A. R. Muniz, *Innovative Food Sci. Emerging Technol.*, 2022, **75**, 102911.
141 S. Zhang, Y. Li, Z. Bao, N. Sun and S. Lin, *Int. J. Biol. Macromol.*, 2021, **182**, 849–857.
142 C. P. Samaranayake and S. K. Sastry, *Phys. Chem. Chem. Phys.*, 2021, **23**, 14422–14432.
143 A. R. Ruiz-Fernández, L. Campos, F. Villanelo, S. E. Gutiérrez-Maldonado and T. Perez-Acle, *Membranes*, 2021, **11**, 473.
144 B. Narayan, C. Herbert, B. J. Rodriguez, B. R. Brooks and N.-V. Buchete, *J. Phys. Chem. B*, 2021, **125**, 5233–5242.
145 M. Dong, H. Tian, Y. Xu, M. Han and X. Xu, *Food Chem.*, 2021, **342**, 128306.
146 S. Basu, B. Gorai, B. Basu and P. K. Maiti, *J. Phys. Chem. B*, 2021, **125**, 3–16.
147 S. Muscat, F. Stojceski and A. Danani, *J. Mol. Graphics Modell.*, 2020, **96**, 107535.
148 I. Baruah and G. Borgohain, *Biophys. Chem.*, 2020, 106479.
149 Z. Jiang, L. You, W. Dou, T. Sun and P. Xu, *Polymers*, 2019, **11**, 282.
150 J. J. Timmons, J. Preto, J. A. Tuszynski and E. T. Wong, *PLoS One*, 2018, **13**, e0202141.
151 Y. Lu, X.-F. Shi, F. R. Salsbury and P. Derreumaux, *J. Chem. Phys.*, 2017, **146**, 145101.
152 H. Alizadeh, J. Davoodi and H. Rafii-Tabar, *J. Mol. Graphics Modell.*, 2017, **73**, 108–114.
153 N. Todorova, A. Bentvelzen, N. J. English and I. Yarovsky, *J. Chem. Phys.*, 2016, **144**, 085101.
154 Y. Xie, Y. Pan, R. Zhang, Y. Liang and Z. Li, *Appl. Surf. Sci.*, 2015, **326**, 55–65.

155 S. K. Vanga, A. Singh and V. Raghavan, *Innovative Food Sci. Emerging Technol.*, 2015, **30**, 79–88.
156 T. E. Benavidez, D. Torrente, M. Marucho and C. D. Garcia, *Langmuir*, 2015, **31**, 2455–2462.
157 X. Wang, Y. Li, X. He, S. Chen and J. Z. H. Zhang, *J. Phys. Chem. A*, 2014, **118**, 8942–8952.
158 M. Damm, C. Nusshold, D. Cantillo, G. N. Rechberger, K. Gruber, W. Sattler and C. O. Kappe, *J. Proteomics*, 2012, **75**, 5533–5543.
159 P. Marracino, F. Apollonio, M. Liberti, G. d'Inzeo and A. Amadei, *J. Phys. Chem. B*, 2013, **117**, 2273–2279.
160 Y. Wu, S. Qin, Y. Zang, M. Zhou, S. Chen and S. Huang, *Innovative Food Sci. Emerging Technol.*, 2023, **89**, 103484.
161 J.-N. Wei, X.-A. Zeng, T. Tang, Z. Jiang and Y.-Y. Liu, *Innovative Food Sci. Emerging Technol.*, 2018, **45**, 249–254.
162 R. Yang, S.-Q. Li and Q. H. Zhang, *J. Agric. Food Chem.*, 2004, **52**, 7400–7406.
163 Y. Tokunaga, M. Tanaka, H. Iida, M. Kinoshita, Y. Tojima, K. Takeuchi and M. Imashimizu, *Biophys. J.*, 2021, **120**, 2386–2393.
164 A. Homenko, B. Kapilevich, R. Kornstein and M. Firer, *Bioelectromagnetics*, 2009, **30**, 167–175.
165 I. Bekard and D. E. Dunstan, *Soft Matter*, 2014, **10**, 431–437.
166 K. Kang, *Front. Phys.*, 2023, **11**, 1282099.
167 W. Jin, Z. Wang, D. Peng, W. Shen, Z. Zhu, S. Cheng, B. Li and Q. Huang, *Food Hydrocolloids*, 2020, **101**, 105547.
168 K. Tsuji and B. Hess, *Ferroelectrics*, 1988, **86**, 147–157.
169 K. Tsuji, S. C. Miiller and B. Hess, *Eur. Biophys. J.*, 1988, **15**, 329–337.
170 K. Tsuji and B. Hess, *Eur. Biophys. J.*, 1986, **13**, 273–280.
171 K. Tsuji and E. Neumann, *Biophys. Chem.*, 1983, **17**, 153–163.
172 K. Tsuji and E. Neumann, *Int. J. Biol. Macromol.*, 1981, **3**, 231–242.
173 D. De, N. Pawar and A. N. Gupta, *Phys. Chem. Chem. Phys.*, 2021, **23**, 4195–4204.
174 P. A. Vargas-Rosales, A. D'Addio, Y. Zhang and A. Caflisch, *ACS Phys. Chem. Au*, 2023, **3**, 456–466.
175 S. Kalita, H. Bergman, K. D. Dubey and S. Shaik, *J. Am. Chem. Soc.*, 2023, **145**, 3543–3553.
176 R. M. Rodrigues, L. H. Fasolin, Z. Avelar, S. B. Petersen, A. A. Vicente and R. N. Pereira, *Food Hydrocolloids*, 2020, **101**, 105505.
177 W. Peng, Z. Zhu, J. Lou, K. Chen, Y. Wu and C. Chang, *eLight*, 2023, **3**, 18.
178 R. M. Rodrigues, Z. Avelar, A. A. Vicente, S. B. Petersen and R. N. Pereira, *Food Chem.*, 2020, **304**, 125442.
179 R. Wang, Q.-H. Wen, X.-A. Zeng, J.-W. Lin, J. Li and F.-Y. Xu, *Food Chem.*, 2022, **377**, 131945.
180 R. Wang, P.-F. Guo, J.-P. Yang, Y.-Y. Huang, L.-H. Wang, J. Li, S.-Y. Lin, Q.-L. Sheng, X.-A. Zeng and Y.-X. Teng, *Food Hydrocolloids*, 2025, **160**, 110761.
181 H. Wu, M. R. Ghaani, Z. Futera and N. J. English, *J. Phys. Chem. B*, 2022, **126**, 376–386.
182 V. D'Annibale, D. Fracassi, P. Marracino, G. D'Inzeo and M. D'Abramo, *Molecules*, 2022, **27**, 6454.
183 Y. Sun, Y. Li, Y. Yang, S. Wang and Y. Gong, *Spectrochim. Acta, Part A*, 2025, 126039.
184 P.-K. Yang, *Biopolymers*, 2014, **101**, 861–870.
185 A. Baumketner, *J. Phys. Chem. B*, 2014, **118**, 14578–14589.
186 H. Wu, M. R. Ghaani, P. K. Nandi and N. J. English, *J. Phys. Chem. B*, 2022, **126**, 858–868.
187 R. Reale, N. J. English, J.-A. Garate, P. Marracino, M. Liberti and F. Apollonio, *J. Chem. Phys.*, 2013, **139**, 205101.
188 N. J. English and J.-A. Garate, *J. Chem. Phys.*, 2016, **145**, 085102.
189 J. A. Garate, A. Bernardin, Y. Escalona, C. Yanez, N. J. English and T. Perez-Acle, *J. Phys. Chem. B*, 2019, **123**, 2599–2608.
190 F. Apollonio, M. Liberti, A. Amadei, M. Aschi, M. Pellegrino, M. D'Alessandro, M. D'Abramo, A. Di Nola and G. d'Inzeo, *IEEE Trans. Microwave Theory Tech.*, 2008, **56**, 2511–2519.
191 D. Gou, K. Huang, Y. Liu, H. Shi and Z. Wu, *J. Phys. Chem. B*, 2022, **126**, 7686–7700.
192 D. Ray, M. Madani, J. K. G. Dhont, F. Platten and K. Kang, *J. Phys. Chem. Lett.*, 2024, **15**, 8108–8113.
193 D. Hou and H.-C. Chang, *Appl. Phys. Lett.*, 2008, **92**, 223902.
194 H. Koizumi, S. Uda, K. Fujiwara, M. Tachibana, K. Kojima and J. Nozawa, *Cryst. Growth Des.*, 2014, **14**, 5662–5667.
195 H. Koizumi, K. Fujiwara and S. Uda, *Cryst. Growth Des.*, 2009, **9**, 2420–2424.
196 H. Koizumi, S. Uda, K. Fujiwara, J. Okada and J. Nozawa, *Crystals*, 2017, **7**, 170.
197 F. Li and R. Lakerveld, *Cryst. Growth Des.*, 2017, **17**, 3062–3070.
198 C. N. Nanev and A. Penkova, *Colloids Surf., A*, 2002, **209**, 139–145.
199 L. Fiona Alexander and N. Radacsi, *CrystEngComm*, 2019, **21**, 5014–5031.
200 M. Taleb, C. Didierjean, C. Jelsch, J. P. Mangeot, B. Capelle and A. Aubry, *J. Cryst. Grow.*, 1999, **200**, 575–582.
201 M. Taleb, C. Didierjean, C. Jelsch, J. Mangeot and A. Aubry, *J. Cryst. Grow.*, 2001, **232**, 250–255.
202 Y. Tomita, H. Koizumi, S. Uda, K. Fujiwara and J. Nozawa, *J. Appl. Crystallogr.*, 2012, **45**, 207–212.
203 M. I. Al-haq, E. Lebrasseur, H. Tsuchiya and T. Torii, *Crystallogr. Rev.*, 2007, **13**, 29–64.
204 G. Rummel, A. Hardmeyer, C. Widmer, M. L. Chiu, P. Nollert, K. P. Locher, I. Pedruzzi, E. M. Landau and J. P. Rosenbusch, *J. Struct. Biol.*, 1998, **121**, 82–91.
205 E. Nieto-Mendoza, B. A. Frontana-Uribe, G. Sazaki and A. Moreno, *J. Cryst. Grow.*, 2005, **275**, e1437–e1446.
206 A. Moreno and G. Sazaki, *J. Cryst. Grow.*, 2004, **264**, 438–444.
207 E. Rubin, C. Owen and V. Stojanoff, *Crystals*, 2017, **7**, 206.
208 H. Koizumi, S. Uda, K. Fujiwara, M. Tachibana, K. Kojima and J. Nozawa, *J. Appl. Crystallogr.*, 2013, **46**, 25–29.
209 T. Wakamatsu, *Trans. Mater. Res. Soc. Jpn.*, 2016, **41**, 13–15.
210 H. Koizumi, Y. Tomita, S. Uda, K. Fujiwara and J. Nozawa, *J. Cryst. Grow.*, 2012, **352**, 155–157.
211 C. Pareja-Rivera, M. Cuéllar-Cruz, N. Esturau-Escofet, N. Demitri, M. Polentarutti, V. Stojanoff and A. Moreno, *Cryst. Growth Des.*, 2017, **17**, 135–145.

212 M. I. Al-Haq, E. Lebrasseur, W.-K. Choi, H. Tsuchiya, T. Torii, H. Yamazaki and E. Shinohara, *J. Appl. Crystallogr.*, 2007, **40**, 199–201.
213 N. J. English and D. A. Mooney, *J. Chem. Phys.*, 2007, **126**, 091105.
214 F. Toschi, F. Lugli, F. Biscarini and F. Zerbetto, *J. Phys. Chem. B*, 2009, **113**, 369–376.
215 N. J. English and C. J. Waldron, *Phys. Chem. Chem. Phys.*, 2015, **17**, 12407–12440.
216 E. della Valle, P. Marracino, O. Pakhomova, M. Liberti and F. Apollonio, *PLoS One*, 2019, **14**, e0221685.
217 J. Průša and M. Cifra, *Sci. Rep.*, 2019, **9**, 19721.
218 H. R. Saeidi, A. Lohrasebi and K. Mahnam, *J. Mol. Model.*, 2014, **20**, 2395.
219 S. S. Setayandeh and A. Lohrasebi, *J. Mol. Model.*, 2015, **21**, 85.
220 P. Marracino, A. Paffi and G. d'Inzeo, *Phys. Chem. Chem. Phys.*, 2022, **24**, 11654–11661.
221 A. Amadei and P. Marracino, *RSC Adv.*, 2015, **5**, 96551–96561.
222 J. D. Slocum and L. J. Webb, *Annu. Rev. Phys. Chem.*, 2018, **69**, 253–271.
223 E. S. Park, S. S. Andrews, R. B. Hu and S. G. Boxer, *J. Phys. Chem. B*, 1999, **103**, 9813–9817.
224 E. S. Park, M. R. Thomas and S. G. Boxer, *J. Am. Chem. Soc.*, 2000, **122**, 12297–12303.
225 J. Průša and M. Cifra, *Comput. Struct. Biotechnol. J.*, 2023, **21**, 1349–1361.
226 G. Urabe, T. Sato, G. Nakamura, Y. Kobashigawa, H. Morioka and S. Katsuki, *Sci. Rep.*, 2020, **10**, 12003.
227 N. K. Pandey, S. Mitra, M. Chakraborty, S. Ghosh, S. Sen, S. Dasgupta and S. DasGupta, *J. Phys. D: Appl. Phys.*, 2014, **47**, 305401.
228 Y.-F. Liu, I. Oey, P. Bremer, A. Carne and P. Silcock, *Food Res. Int.*, 2017, **91**, 161–170.
229 M. Mora, A. Stannard and S. Garcia-Manyes, *Chem. Soc. Rev.*, 2020, **49**, 6816–6832.
230 J. Alegre-Cebollada, *Biophys. Rev.*, 2021, **13**, 435–454.
231 N. A. Chebotareva, S. G. Roman and B. I. Kurganov, *Biophys. Rev.*, 2016, **8**, 397–407.
232 H. R. Saeidi, S. S. Setayandeh and A. Lohrasebi, *Chin. Phys. B*, 2015, **24**, 080701.
233 S. S. Setayandeh and A. Lohrasebi, *J. Nanosci. Nanotechnol.*, 2018, **18**, 7902–7906.
234 F. Lugli, F. Toschi, F. Biscarini and F. Zerbetto, *J. Chem. Theory Comput.*, 2010, **6**, 3516–3526.
235 S. Sen, M. Chakraborty, S. Goley, S. Dasgupta and S. DasGupta, *Biophys. Chem.*, 2017, **226**, 23–33.
236 S. Yamazaki, M. Harata, T. Idehara, K. Konagaya, G. Yokoyama, H. Hoshina and Y. Ogawa, *Sci. Rep.*, 2018, **8**, 9990.
237 K. Kang and F. Platten, *Sci. Rep.*, 2022, **12**, 3061.
238 J. Jurgelevičiūtė, N. Bičkovas, A. Sakalauskas, V. Novickij, V. Smirnovas and E. Lastauskienė, *Appl. Sci.*, 2021, **11**, 2684.
239 O. P. Cherkasova, V. I. Fedorov, E. F. Nemova and A. S. Pogodin, *Opt. Spectrosc.*, 2009, **107**, 534–537.
240 X. Xu, S. Xiao, L. Wang, D. Niu, W. Gao, X.-A. Zeng, M. Woo, Z. Han and R. Wang, *Int. J. Biol. Macromol.*, 2024, **257**, 128509.
241 A. Taha, F. Casanova, P. Šimonis, J. Jonikaitė-Švėgždienė, M. Jurkūnas, M. A. E. Gomaa and A. Stirké, *Innovative Food Sci. Emerging Technol.*, 2022, **82**, 103190.
242 K. Zhong, X. Hu, G. Zhao, F. Chen and X. Liao, *Food Chem.*, 2005, **92**, 473–479.
243 T. Yu and X. Fu, *Bioelectrochemistry*, 2015, **101**, 42–45.
244 Y. Li, S. Zhang, Z. Bao, N. Sun and S. Lin, *Innovative Food Sci. Emerging Technol.*, 2022, **76**, 102918.
245 M.-L. Tian, T. Fang, M.-Y. Du and F.-S. Zhang, *Protein J.*, 2016, **35**, 154–162.
246 C. P. Samaranayake and S. K. Sastry, *LWT–Food Sci. Technol.*, 2018, **90**, 448–454.
247 H. W. Yeom, Q. H. Zhang and C. P. Dunne, *Food Chem.*, 1999, **67**, 53–59.
248 H. Vega-Mercado, J. R. Powers, G. V. Barbosa-Cánovas and B. G. Swanson, *J. Food Sci.*, 1995, **60**, 1143–1146.
249 S. Y. Ho, G. S. Mittal and J. D. Cross, *J. Food Eng.*, 1997, **31**, 69–84.
250 M. Porcelli, G. Cacciapuoti, S. Fusco, R. Massa, G. d'Ambrosio, C. Bertoldo, M. De Rosa and V. Zappia, *FEBS Lett.*, 1997, **402**, 102–106.
251 C. Arroyo, T. M. Kennedy, J. G. Lyng and M. O'Sullivan, *Food Bioprod. Process.*, 2017, **105**, 95–103.
252 R.-S. Agoua, L. Bazinet, E. Vorobiev, N. Grimi and S. Mikhaylin, *ACS Sustainable Chem. Eng.*, 2020, **8**, 14775–14785.
253 *Clinical Aspects of Electroporation*, ed. S. T. Kee, J. Gehl and E. W. Lee, Springer New York, New York, NY, 2011.
254 N. J. English and D. G. Carroll, *J. Chem. Inf. Comput. Sci.*, 2001, **41**, 1150–1161.
255 N. J. English, *Mol. Phys.*, 2005, **103**, 1945–1960.
256 N. J. English, *Mol. Phys.*, 2008, **106**, 1887–1898.
257 H. Cao, N. J. English and J. M. D. MacElroy, *J. Chem. Phys.*, 2013, **138**, 094507.
258 K. Ishibashi, S. Hara and S. Kondo, *Clin. Exp. Nephrol.*, 2009, **13**, 107–117.
259 A. S. Verkman, P.-W. Phuan, N. Asavapanumas and L. Tradtrantip, *Brain Pathol.*, 2013, **23**, 684–695.
260 A. Verkman, *Annu. Rev. Med.*, 2012, **63**, 303–316.
261 P. Marracino, M. Bernardi, M. Liberti, F. Del Signore, E. Trapani, J.-A. Gárate, C. J. Burnham, F. Apollonio and N. J. English, *ACS Omega*, 2018, **3**, 15361–15369.
262 M. L. Fernández, M. Risk, R. Reigada and P. T. Vernier, *Biochem. Biophys. Res. Commun.*, 2012, **423**, 325–330.
263 M. Bernardi, P. Marracino, M. Liberti, J. Garate, C. Burnham, F. Apollonio and N. English, *Phys. Chem. Chem. Phys.*, 2019, 1–8.
264 M. Bernardi, P. Marracino, M. R. Ghaani, M. Liberti, F. Del Signore, C. J. Burnham, J.-A. Gárate, F. Apollonio and N. J. English, *J. Chem. Phys.*, 2018, **149**, 245102.
265 M. Bernardi, M. R. Ghaani and N. J. English, *Mol. Phys.*, 2019, **117**, 3783–3790.
266 L. Rems, M. A. Kasimova, I. Testa and L. Delemotte, *Biophys. J.*, 2020, **119**, 190–205.
267 T. Y. Tsong and C.-H. Chang, *Chin. J. Phys.*, 2005, **43**, 273–284.

268 P. Marracino, M. Liberti, E. Trapani, C. Burnham, M. Avena, J.-A. Garate, F. Apollonio and N. English, *Int. J. Mol. Sci.*, 2016, **17**, 1133.
269 K. Tsuji and E. Neumann, *FEBS Lett.*, 1981, **128**, 265–268.
270 K. Tsuji and B. Hess, *Eur. Biophys. J.*, 1990, **18**, 63–69.
271 B. E. Knox and T. Tsong, *J. Biol. Chem.*, 1984, **259**, 4757–4763.
272 T. Y. Tsong, *Biochim. Biophys. Acta, Rev. Biomembr.*, 1992, **1113**, 53–70.
273 E. H. Serpersu and T. Y. Tsong, *J. Biol. Chem.*, 1984, **259**, 7155–7162.
274 D. S. Liu, R. D. Astumian and T. Y. Tsong, *J. Biol. Chem.*, 1990, **265**, 7260–7267.
275 H. V. Westerhoff, T. Y. Tsong, P. B. Chock, Y.-D. Chen and R. D. Astumian, *Proc. Natl. Acad. Sci. U. S. A.*, 1986, **83**, 4734–4738.
276 T. Y. Tsong, D.-S. Liu, F. Chauvin and R. D. Astumian, *Biosci. Rep.*, 1989, **9**, 13–26.
277 T. Y. Tsong, *Annu. Rev. Biophys. Biophys. Chem.*, 1990, **19**, 83–106.
278 V. S. Markin and T. Y. Tsong, *Biophys. J.*, 1991, **59**, 1308–1316.
279 V. Markin, D. Liu, M. Rosenberg and T. Tsong, *Biophys. J.*, 1992, **61**, 1045–1049.
280 T. Xie, P. Marszalek, Y. Chen and T. Y. Tsong, *Biophys. J.*, 1994, **67**, 1247–1251.
281 T. Xie, Y.-D. Chen, P. Marszalek and T. Y. Tsong, *Biophys. J.*, 1997, **72**, 2496–2502.
282 T. Y. Tsong and C.-H. Chang, *AAPPS Bull.*, 2003, **13**, 12–18.
283 T. Nakabayashi, M. Kinjo and N. Ohta, *Chem. Phys. Lett.*, 2008, **457**, 408–412.
284 I. Barak, M. Golosovsky and D. Davidov, *Piers Online*, 2009, **5**, 561–566.
285 J. W. Park and Y. M. Rhee, *J. Am. Chem. Soc.*, 2016, **138**, 13619–13629.
286 P. P. Pompa, A. Bramanti, G. Maruccio, R. Cingolani, F. De Rienzo, S. Corni, R. Di Felice and R. Rinaldi, *J. Chem. Phys.*, 2005, **122**, 181102.
287 T. Nakabayashi, M. Wahadoszamen and N. Ohta, *J. Am. Chem. Soc.*, 2005, **127**, 7041–7052.
288 P. P. Pompa, A. Bramanti, G. Maruccio, L. L. del Mercato, R. Chiuri, R. Cingolani and R. Rinaldi, SPIE Proceedings, 2005, p. 171.
289 D. Havelka, D. E. Chafai, O. Krivosudský, A. Klebanovych, F. Vostárek, L. Kubínová, P. Dráber and M. Cifra, *Adv. Mater. Technol.*, 2020, **5**, 1900669.
290 P. Afaghi, M. A. Lapolla and K. Ghandi, *Sci. Rep.*, 2021, **11**, 23373.
291 A. Intze, M. E. Temperini, G. Gregori, F. Verde, M. Ortolani and V. Giliberti, *IEEE Trans. Terahertz Sci. Technol.*, 2024, **14**, 652–660.
292 D. Havelka, I. Zhernov, M. Teplan, Z. Lánský, D. E. Chafai and M. Cifra, *Sci. Rep.*, 2022, **12**, 2462.
293 M. A. Schroer, S. Schewa, A. Y. Gruzinov, C. Rönnau, J. M. Lahey-Rudolph, C. E. Blanchet, T. Zickmantel, Y.-H. Song, D. I. Svergun and M. Roessle, *Sci. Rep.*, 2021, **11**, 22311.
294 J. C. Bischof and X. He, *Ann. N. Y. Acad. Sci.*, 2006, **1066**, 12–33.
295 F. Zhao, S. M. Matt, J. Bu, O. G. Rehrauer, D. Ben-Amotz and S. A. McLuckey, *J. Am. Soc. Mass Spectrom.*, 2017, **28**, 2001–2010.
296 J. Wu, Z. Zhou, Y. Huang, X. Deng, S. Zheng, S. He, G. Huang, B. Hu, M. Shi, W. Liao and N. Huang, *MedComm*, 2024, **5**, e746.
297 Z. Haider, J. Modolo, M. Liberti, F. Apollonio and M. Zhadobov, *IEEE J. Microwaves*, 2023, **3**, 170–180.
298 Y. Y. Chen and A. W. Wood, *Bioelectromagnetics*, 2009, **30**, 583–590.
299 A. Salari, M. Navi, T. Lijnse and C. Dalton, *Micromachines*, 2019, **10**, 762.
300 A. González, A. Ramos, H. Morgan, N. G. Green and A. Castellanos, *J. Fluid Mech.*, 2006, **564**, 415–433.
301 A. Khayari, M. Medrano, E. Verlage, M. C. Velázquez-Ahumada, M. J. Freire and A. Ramos, *J. Appl. Phys.*, 2011, **110**, 064912.
302 R. Orlacchio, M. Zhadobov, S. I. Alekseev, D. Nikolayev, R. Sauleau, Y. Le Page and Y. Le Dréan, *Bioelectromagnetics*, 2019, **40**, 553–568.
303 R. Piazza, *Soft Matter*, 2008, **4**, 1740.
304 A. Ramos, H. Morgan, N. G. Green and A. Castellanos, *J. Phys. D: Appl. Phys.*, 1998, **31**, 2338.
305 N. G. Green, A. Ramos, A. González, H. Morgan and A. Castellanos, *Phys. Rev. E:Stat. Phys., Plasmas, Fluids, Relat. Interdiscip. Top.*, 2000, **61**, 4011–4018.
306 T. M. Squires and M. Z. Bazant, *J. Fluid Mech.*, 2004, **509**, 217–252.
307 B. J. Kirby and E. F. Hasselbrink, *Electrophoresis*, 2004, **25**, 187–202.
308 C.-C. Chang and R.-J. Yang, *Microfluid. Nanofluid.*, 2007, **3**, 501–525.
309 C. Moino, F. Artusio and R. Pisano, *Int. J. Pharm.*, 2024, **650**, 123679.
310 C. C. Roth, R. A. Barnes Jr., B. L. Ibey, H. T. Beier, L. Christopher Mimun, S. M. Maswadi, M. Shadaram and R. D. Glickman, *Sci. Rep.*, 2015, **5**, 15063.
311 B. Harish, R. E. Gillilan, J. Zou, J. Wang, D. P. Raleigh and C. A. Royer, *Biophys. J.*, 2021, **120**, 2592–2598.
312 A. Y. Starikovskiy and M. N. Shneider, *Phys. Fluids*, 2024, **36**, 042011.
313 K. S. Suslick, *Science*, 1990, **247**, 1439–1445.
314 P. Riesz, K. Takashi and C. M. Krishna, *Free Radical Res. Commun.*, 1990, **10**, 27–35.
315 T. W. Randolph, E. Schiltz, D. Sederstrom, D. Steinmann, O. Mozziconacci, C. Schöneich, E. Freund, M. S. Ricci, J. F. Carpenter and C. S. Lengsfeld, *J. Pharm. Sci.*, 2015, **104**, 602–611.
316 E. Y. Lau, M. L. Berkowitz and E. Schwegler, *Biophys. J.*, 2016, **110**, 147–156.
317 R. Šmerc, D. Miklavčič and S. Mahnič-Kalamiza, *Electrochim. Acta*, 2024, 145363.
318 K. Talley and E. Alexov, *Proteins: Struct., Funct., Bioinf.*, 2010, **78**, 2699–2706.
319 L. Konermann, E. A. Silva and O. F. Sogbein, *Anal. Chem.*, 2001, **73**, 4836–4844.

320 P. Turjanski, N. Olaiz, P. Abou-Adal, C. Suárez, M. Risk and G. Marshall, *Electrochim. Acta*, 2009, **54**, 6199–6206.
321 P. G. Erlandsson and N. D. Robinson, *Electrophoresis*, 2011, **32**, 784–790.
322 T. Kakiuchi, *J. Solid State Electrochem.*, 2011, **15**, 1661–1671.
323 K. Wang, W. Mao, X. Song, M. Chen, W. Feng, B. Peng and Y. Chen, *Chem. Soc. Rev.*, 2023, **52**, 6957–7035.
324 K. Červinková, P. Vahalová, M. Poplová, T. Zakar, D. Havelka, M. Paidar, V. Kolivoška and M. Cifra, *Sci. Rep.*, 2024, **14**, 22649.
325 E. R. Stadtman, *Annu. Rev. Biochem.*, 1993, **62**, 797–821.
326 M. J. Davies, *Biochem. J.*, 2016, **473**, 805–825.
327 P. Vahalová, D. Havelka, E. Vaněčková, T. Zakar, V. Kolivoška and M. Cifra, *Sens. Actuators, B*, 2023, **385**, 133676.
328 E. D'Imprima, D. Floris, M. Joppe, R. Sánchez, M. Grininger and W. Kühlbrandt, *eLife*, 2019, **8**, e42747.
329 K. Mitra, I. Ubarretxena-Belandia, T. Taguchi, G. Warren and D. M. Engelman, *Proc. Natl. Acad. Sci. U. S. A.*, 2004, **101**, 4083–4088.
330 D. Stuerga and P. Gaillard, *J. Microwave Power Electromagn. Energy*, 1996, **31**, 101–113.
331 D. Stuerga and P. Gaillard, *J. Microwave Power Electromagn. Energy*, 1996, **31**, 87–100.
332 I. Y. Belyaev, V. S. Shcheglov, E. D. Alipov and V. D. Ushakov, *IEEE Trans. Microwave Theory Tech.*, 2000, **48**, 2172–2179.
333 K. R. Foster, *IEEE Trans. Plasma Sci.*, 2000, **28**, 15–23.
334 R. K. Adair, *Bioelectromagnetics*, 2003, **24**, 39–48.
335 M. Cifra, J. Z. Fields and A. Farhadi, *Prog. Biophys. Mol. Biol.*, 2011, **105**, 223–246.
336 O. Kučera and M. Cifra, *J. Biol. Phys.*, 2016, **42**, 1–8.
337 M. Cifra, F. Apollonio, M. Liberti, T. García-Sánchez and L. M. Mir, *Int. J. Biometeorol.*, 2021, **65**, 59–67.
338 F. Apollonio, M. Liberti, A. Paffi, C. Merla, P. Marracino, A. Denzi, C. Marino and G. d'Inzeo, *IEEE Trans. Microwave Theory Tech.*, 2013, **61**, 2031–2045.
339 N. T. Hunt, *Chem. Soc. Rev.*, 2009, **38**, 1837–1848.
340 M. Maiuri, M. Garavelli and G. Cerullo, *J. Am. Chem. Soc.*, 2020, **142**, 3–15.
341 E. D. B. Foley, M. S. Kushwah, G. Young and P. Kukura, *Nat. Methods*, 2021, **18**, 1–6.
342 G. Young and P. Kukura, *Annu. Rev. Phys. Chem.*, 2019, **70**, 301–322.
343 K. Schoenbach, J. Kolb, S. Xiao, S. Katsuki, Y. Minamitani and R. Joshi, *Plasma Sources Sci. Technol.*, 2008, **17**, 024010.
344 H. M. Jones and E. E. Kunhardt, *J. Appl. Phys.*, 1995, **77**, 795–805.
345 S. Y. Joshi and S. A. Deshmukh, *Mol. Simul.*, 2021, **47**, 786–803.
346 S. Kmiecik, D. Gront, M. Kolinski, L. Wieteska, A. E. Dawid and A. Kolinski, *Chem. Rev.*, 2016, **116**, 7898–7936.
347 D. Xu, J. C. Phillips and K. Schulten, *J. Phys. Chem.*, 1996, **100**, 12108–12121.
348 B. Rakos, *Int. J. Circ. Theory Appl.*, 2015, **43**, 60–72.
349 Z. Jing, C. Liu, S. Y. Cheng, R. Qi, B. D. Walker, J.-P. Piquemal and P. Ren, *Annu. Rev. Biophys.*, 2019, **48**, 371–394.
350 J. Liu, T. Zhu, X. Wang, X. He and J. Z. H. Zhang, *J. Chem. Theory Comput.*, 2015, **11**, 5897–5905.
351 D. J. Cole and N. D. M. Hine, *J. Phys.: Condens. Matter*, 2016, **28**, 393001.
352 E. Neumann, *Top. Bioelectrochem. Bioenerg.*, 1981, **4**, 113–160.
353 M. J. Schnitzer, K. Visscher and S. M. Block, *Nat. Cell Biol.*, 2000, **2**, 718–723.
354 T.-L. Kuo, S. Garcia-Manyes, J. Li, I. Barel, H. Lu, B. J. Berne, M. Urbakh, J. Klafter and J. M. Fernández, *Proc. Natl. Acad. Sci. U. S. A.*, 2010, **107**, 11336–11340.
355 W.-W. Sun, S.-J. Yu, X.-A. Zeng, X.-Q. Yang and X. Jia, *Food Res. Int.*, 2011, **44**, 1052–1058.
356 M. Shafiei, M. von Domaros, D. Bratko and A. Luzar, *J. Chem. Phys.*, 2019, **150**, 074505.
357 Z. Futera and N. J. English, *J. Chem. Phys.*, 2017, **147**, 031102.
358 G. Cassone, *J. Phys. Chem. Lett.*, 2020, **11**, 8983–8988.
359 V. Conti Nibali, S. Maiti, F. Saija, M. Heyden and G. Cassone, *J. Chem. Phys.*, 2023, **158**, 184501.
360 H. Vega-Mercado, O. Martín-Belloso, B.-L. Qin, F. J. Chang, M. Marcela Góngora-Nieto, G. V. Barbosa-Cánovas and B. G. Swanson, *Trends Food Sci. Technol.*, 1997, **8**, 151–157.
361 G. V. Barbosa-Cánovas and Q. H. Zhang, *Pulsed electric fields in food processing: fundamental aspects and applications*, CRC Press, 2001.
362 A. Van Loey, B. Verachtert and M. Hendrickx, *Trends Food Sci. Technol.*, 2001, **12**, 94–102.
363 R. Soliva-Fortuny, A. Balasa, D. Knorr and O. Martín-Belloso, *Trends Food Sci. Technol.*, 2009, **20**, 544–556.
364 W. Zhao and R. Yang, in *Handbook of Electroporation*, ed. D. Miklavčič, Springer International Publishing, Cham, 2017, pp. 2239–2251.
365 R. M. Rodrigues, A. J. Martins, O. L. Ramos, F. X. Malcata, J. A. Teixeira, A. A. Vicente and R. N. Pereira, *Food Hydrocolloids*, 2015, **43**, 329–339.
366 J.-Y. Qian, L.-J. Ma, L.-J. Wang and W. Jiang, *LWT–Food Sci. Technol.*, 2016, **74**, 331–337.
367 L. Wu, W. Zhao, R. Yang, W. Yan and Q. Sun, *J. Sci. Food Agric.*, 2016, **96**, 3334–3341.
368 B. Y. Xiang, M. O. Ngadi, L. A. Ochoa-Martinez and M. V. Simpson, *Food Bioprocess Technol.*, 2011, **4**, 1341–1348.
369 B. Y. Xiang, M. O. Ngadi, B. K. Simpson and M. V. Simpson, *J. Food Process. Preserv.*, 2011, **35**, 563–570.
370 R. N. Pereira, J. A. Teixeira and A. A. Vicente, *J. Agric. Food Chem.*, 2011, **59**, 11589–11597.
371 R. M. Rodrigues, A. A. Vicente, S. B. Petersen and R. N. Pereira, *Innovative Food Sci. Emerging Technol.*, 2019, **52**, 1–7.
372 Y. Li, Z. Chen and H. Mo, *LWT–Food Sci. Technol.*, 2007, **40**, 1167–1175.
373 A. Singh, R. Lahlali, S. K. Vanga, C. Karunakaran, V. Orsat and V. Raghavan, *Int. J. Food Prop.*, 2016, **19**, 1217–1226.
374 S. K. Vanga, A. Singh, F. Kalkan, Y. Gariepy, V. Orsat and V. Raghavan, *Int. J. Food Prop.*, 2016, **19**, 1259–1271.
375 R. N. Pereira, B. W. S. Souza, M. A. Cerqueira, J. A. Teixeira and A. A. Vicente, *Biomacromolecules*, 2010, **11**, 2912–2918.
376 Y.-Q. Li, *Phys. Procedia*, 2012, **33**, 132–137.

377 W. Zhao, R. Yang, Y. Tang and R. Lu, *Int. J. Food Eng.*, 2007, **3**, 12.
378 R. N. Pereira, R. M. Rodrigues, Ó. L. Ramos, F. Xavier Malcata, J. A. Teixeira and A. A. Vicente, *Food Bioprocess Technol.*, 2016, **9**, 576–587.
379 R. N. Pereira, R. M. Rodrigues, E. Altinok, Ó. L. Ramos, F. Xavier Malcata, P. Maresca, G. Ferrari, J. A. Teixeira and A. A. Vicente, *Food Res. Int.*, 2017, **99**, 435–443.
380 T. Grahl and H. Märkl, *Appl. Microbiol. Biotechnol.*, 1996, **45**, 148–157.
381 A. J. Castro, B. G. Swanson, G. V. Barbosa-Cánovas and Q. H. Zhang, *Pulsed Electric Fields in Food Processing*, CRC Press, 2001, pp. 65–82.
382 C. P. Samaranayake and S. K. Sastry, *J. Food Eng.*, 2016, **186**, 17–26.
383 C. P. Samaranayake and S. K. Sastry, *Food Chem.*, 2016, **199**, 265–272.
384 A. G. Pakhomov, S. Xiao, O. N. Pakhomova, I. Semenov, M. A. Kuipers and B. L. Ibey, *Bioelectrochemistry*, 2014, **100**, 88–95.
385 C. Blangero, M. P. Rols and J. Teissié, *Biochim. Biophys. Acta, Biomembr.*, 1989, **981**, 295–302.
386 C. Kanthou, S. Kranjc, G. Sersa, G. Tozer, A. Zupanic and M. Cemazar, *Mol. Cancer Ther.*, 2006, **5**, 3145–3152.
387 L. Carr, PhD thesis, Université de Limoges, 2016.
388 L. Carr, S. M. Bardet, R. C. Burke, D. Arnaud-Cormos, P. Leveque and R. P. O'Connor, *Sci. Rep.*, 2017, **7**, 41267.
389 C. J. W. Meulenberg, V. Todorovic and M. Cemazar, *PLoS One*, 2012, **7**, e52713.
390 D. E. Chafai, F. Vostárek, E. Dráberová, D. Havelka, D. Arnaud-Cormos, P. Leveque, J. Janáček, L. Kubínová, M. Cifra and P. Dráber, *Adv. Biosyst.*, 2020, **4**, 2000070.
391 T. Berghöfer, C. Eing, B. Flickinger, P. Hohenberger, L. H. Wegner, W. Frey and P. Nick, *Biochem. Biophys. Res. Commun.*, 2009, **387**, 590–595.
392 D. G. Harkin and E. D. Hay, *Cell Motil.*, 1996, **35**, 345–357.
393 G. P. Tolstykh, G. L. Thompson, H. T. Beier, Z. A. Steelman and B. L. Ibey, *Biochem. Biophys. Rep.*, 2017, **9**, 36–41.
394 M. Stacey, P. Fox, S. Buescher and J. Kolb, *Bioelectrochemistry*, 2011, **82**, 131–134.
395 G. L. Thompson, C. C. Roth, D. R. Dalzell, M. Kuipers and B. L. Ibey, *J. Biomed. Opt.*, 2014, **19**, 055005.
396 G. L. Thompson, C. Roth, G. Tolstykh, M. Kuipers and B. L. Ibey, *Terahertz and Ultrashort Electromagnetic Pulses for Biomedical Applications*, 2013, p. 85850T.
397 D. L. Perrier, A. Vahid, V. Kathavi, L. Stam, L. Rems, Y. Mulla, A. Muralidharan, G. H. Koenderink, M. T. Kreutzer and P. E. Boukany, *Sci. Rep.*, 2019, **9**, 8151.
398 M. Rief, M. Gautel, F. Oesterhelt, J. M. Fernandez and H. E. Gaub, *Science*, 1997, **276**, 1109–1112.
399 M. D. Fernandez-Diaz, L. Barsotti, E. Dumay and J. C. Cheftel, *J. Agric. Food Chem.*, 2000, **48**, 2332–2339.
400 S. Ilieva, D. Cheshmedzhieva and T. Dudev, *Phys. Chem. Chem. Phys.*, 2019, **21**, 16198–16206.
401 G. Y. Solomentsev, N. J. English and D. A. Mooney, *J. Chem. Phys.*, 2010, **133**, 235102.
402 C. A. Petroff, G. Cassone, J. Šponer and G. R. Hutchison, *Adv. Mater.*, 2021, **33**, 2007486.
403 D. E. Chafai, A. Mehle, A. Tilmatine, B. Maouche and D. Miklavčič, *Bioelectrochemistry*, 2015, **106**, 249–257.
404 W. J. Ellison, *J. Phys. Chem. Ref. Data*, 2007, **36**, 1–18.
405 D. Niu, Y. Feng, X.-A. Zeng and J.-H. Cheng, *Innovative Food Sci. Emerging Technol.*, 2024, **97**, 103826.
406 O. E. Perez and A. M. R. Pilosof, *Food Res. Int.*, 2004, **37**, 102–110.
407 H. Bohr and J. Bohr, *Phys. Rev. E:Stat. Phys., Plasmas, Fluids, Relat. Interdiscip. Top.*, 2000, **61**, 4310–4314.
408 T. Kawasaki, Y. Yamaguchi, T. Ueda, Y. Ishikawa, T. Yaji, T. Ohta, K. Tsukiyama, T. Idehara, M. Saiki and M. Tani, *Biomed. Opt. Express*, 2020, **11**, 5341–5351.
409 D. F. George, M. M. Bilek and D. R. McKenzie, *Bioelectromagnetics*, 2008, **29**, 324–330.
410 D. I. de Pomerai, B. Smith, A. Dawe, K. North, T. Smith, D. B. Archer, I. R. Duce, D. Jones and E. M. Candido, *FEBS Lett.*, 2003, **543**, 93–97.
411 N. Huda and A. K. Bhuyan, *J. Phys. Chem. B*, 2023, **127**, 4386–4395.
412 D. M. Landry, PhD thesis, Brigham Young University – Provo, 2013.
413 Y. Shi, M. J. Acerson, K. L. Shuford and B. F. Shaw, *ACS Chem. Neurosci.*, 2015, **6**, 1696–1707.
414 W. Zhao and R. Yang, *J. Phys. Chem. B*, 2010, **114**, 503–510.
415 W. Zhao, R. Yang, R. Lu, Y. Tang and W. Zhang, *J. Agric. Food Chem.*, 2007, **55**, 9850–9858.
416 W. Zhao and R. Yang, *Eur. Food Res. Technol.*, 2008, **228**, 47–54.
417 I. V. Lundholm, H. Rodilla, W. Y. Wahlgren, A. Duelli, G. Bourenkov, J. Vukusic, R. Friedman, J. Stake, T. Schneider and G. Katona, *Struct. Dyn.*, 2015, **2**, 054702.
418 P. M. Favi, Q. Zhang, H. O'Neill, E. Mamontov and S. O. Diallo, *J. Biol. Phys.*, 2014, **40**, 167–178.
419 G. Urabe, T. Katagiri and S. Katsuki, *Bioelectricity*, 2020, **2**, 33–39.
420 L. Wu, W. Zhao, R. Yang and W. Yan, *Food Chem.*, 2015, **175**, 115–120.
421 L. Wu, W. Zhao, R. Yang and X. Chen, *J. Food Eng.*, 2014, **139**, 13–18.
422 W. Zhao and R. Yang, *J. Phys. Chem. B*, 2008, **112**, 14018–14025.
423 G. Hammarin, P. Norder, R. Harimoorthy, G. Chen, P. Berntsen, P. O. Widlund, C. Stoij, H. Rodilla, J. Swenson, G. Brändén and R. Neutze, *Sci. Rep.*, 2024, **14**, 18286.
424 P. M. Vassilev, R. T. Dronzine, M. P. Vassileva and G. A. Georgiev, *Biosci. Rep.*, 1982, **2**, 1025–1029.
425 I. Minoura and E. Muto, *Biophys. J.*, 2006, **90**, 3739–3748.
426 W. Zhao and R. Yang, *Food Bioprocess Technol.*, 2012, **5**, 1706–1714.
427 J. Zhang, T. Tang, Z. Jiang, Y. Liu and A. Jiang, *Food Chem.*, 2019, **293**, 455–462.
428 Y. Li, S. Zhang, P. Jiang, L. Zhong, S. Lin and N. Sun, *LWT–Food Sci. Technol.*, 2021, **141**, 110891.
429 M. D. L. Meza-Jiménez, P.-R. Pokhrel, R. R. Robles De La Torre, G. V. Barbosa-Canovas and H. Hernández-Sánchez, *LWT–Food Sci. Technol.*, 2019, **109**, 336–341.

430 F. Zhang, M. Tian, M. Du and T. Fang, *J. Food Eng.*, 2017, **205**, 56–63.
431 K. Zhong, J. Wu, Z. Wang, F. Chen, X. Liao, X. Hu and Z. Zhang, *Food Chem.*, 2007, **100**, 115–123.
432 T. Ohshima, T. Tamura and M. Sato, *J. Electrost.*, 2007, **65**, 156–161.
433 J. Castorena-García, F. Martínez-Montes, M. Robles-López, J. Welti-Chanes, H. Hernandez-Sanchez and R. Robles-de-la Torre, *Rev. Mex. Ing. Quim.*, 2013, **12**, 391–400.
434 H. Vega-Mercado, J. R. Powers, G. V. Barbosa-Cánovas and B. G. Swanson, *Pulsed Electric Fields in Food Processing*, CRC Press, 2001, pp. 121–134.
435 J. Wang, S. K. Vanga and V. Raghavan, *Food Funct.*, 2020, **11**, 1373–1384.
436 N. Todorova, A. Bentvelzen and I. Yarovsky, *J. Chem. Phys.*, 2020, **152**, 035104.
437 Z. Rahimi and A. Lohrasebi, *Eur. Phys. J. E:Soft Matter Biol. Phys.*, 2023, **46**, 3.
438 L. Astrakas, C. Gousias and M. Tzaphlidou, *J. Appl. Phys.*, 2011, **109**, 094702.
439 L. G. Astrakas, C. Gousias and M. Tzaphlidou, *J. Appl. Phys.*, 2012, **111**, 074702.
440 N. Hamedi, M. Saviz, A. Banaei, S. Shabani, M. Qafary, A. A. Moosavi-Movahedi and R. Faraji-Dana, *J. Mol. Liq.*, 2020, **312**, 113283.
441 N. J. English, G. Y. Solomentsev and P. O'Brien, *J. Chem. Phys.*, 2009, **131**, 035106.
442 C. J. Burnham and N. J. English, *J. Phys. Chem. Lett.*, 2017, **8**, 4646–4651.
443 A. Budi, F. S. Legge, H. Treutlein and I. Yarovsky, *J. Phys. Chem. B*, 2005, **109**, 22641–22648.
444 A. Budi, F. S. Legge, H. Treutlein and I. Yarovsky, *J. Phys. Chem. B*, 2007, **111**, 5748–5756.
445 E. K. Massaro, I. Goswami, S. S. Verbridge and M. R. von Spakovsky, *Bioelectrochemistry*, 2021, **137**, 107638.
446 T. Yoon, W. Park, Y. Kim and S. Na, *Appl. Surf. Sci.*, 2023, **608**, 155124.
447 R. Saxena, S. K. Vanga and V. Raghavan, *J. Food Biochem.*, 2019, **43**, e12898.
448 Z. Rahimi and A. Lohrasebi, *Adv. Sci., Eng. Med.*, 2018, **10**, 1077–1084.
449 P. Marracino, *J. Phys. Chem. Biophys.*, 2013, **03**, 1000117.
450 T. Dudev, S. Ilieva and L. Doudeva, *Phys. Chem. Chem. Phys.*, 2018, **20**, 24633–24640.
451 L. Wang, S. Qin, O. Wei, X. Liang, D. Fu, J. Yu, S. Huang and L. Xie, *Int. J. Biol. Macromol.*, 2025, **307**, 142398.
452 A. Singh, V. Orsat and V. Raghavan, *Biomolecules*, 2013, **3**, 168–179.
453 S. S. Setayandeh and A. Lohrasebi, *J. Theor. Comput. Chem.*, 2016, **15**, 1650010.
454 A. R. Ruiz-Fernández, L. Campos, F. Villanelo, J. A. Garate and T. Perez-Acle, *Int. J. Mol. Sci.*, 2023, **24**, 11397.
455 W. Treptow, B. Maigret, C. Chipot and M. Tarek, *Biophys. J.*, 2004, **87**, 2365–2379.
456 F. Guo, J. Xiang, Y. Zhuo and K. Pei, *Biomacromolecules*, 2025, **26**, 1002–1011.
457 X. Zhao, W. Ding, H. Wang, Y. Wang, Y. Liu, Y. Li and C. Liu, *ACS Omega*, 2024, **9**, 9702–9713.